ENTRAINMENT AND MIXING PROPERTIES OF MULTIPHASE PLUMES: EXPERIMENTAL STUDIES ON TURBULENCE AND SCALAR STRUCTURE OF A BUBBLE PLUME

A Dissertation

by

DONG-GUAN SEOL

Submitted to the Office of Graduate Studies of
Texas A&M University
in partial fulfillment of the requirements for the degree of

DOCTOR OF PHILOSOPHY

May 2008

Major Subject: Ocean Engineering

ENTRAINMENT AND MIXING PROPERTIES OF MULTIPHASE PLUMES: EXPERIMENTAL STUDIES ON TURBULENCE AND SCALAR STRUCTURE OF A BUBBLE PLUME

A Dissertation

by

DONG-GUAN SEOL

Submitted to the Office of Graduate Studies of
Texas A&M University
in partial fulfillment of the requirements for the degree of

DOCTOR OF PHILOSOPHY

Approved by:

Chair of Committee,	Scott A. Socolofsky
Committee Members,	Kuang-An Chang
	Hamn-Ching Chen
	Yassin Hassan
Head of Department,	David V. Rosowsky

May 2008

Major Subject: Ocean Engineering

ABSTRACT

Entrainment and Mixing Properties of Multiphase Plumes:
Experimental Studies on Turbulence and Scalar Structure
of a Bubble Plume. (May 2008)

Dong-Guan Seol, B.S., Pukyong National University, Korea;
M.S., Pukyong National University, Korea
Chair of Advisory Committee: Dr. Scott A. Socolofsky

This dissertation presents a series of laboratory experiments to study flow and mixing properties of multiphase plumes. The particle image velocimetry (PIV) and laser-induced fluorescence (LIF) techniques are developed to measure two-dimensional velocity and concentration fields of multiphase plumes. The developed measurement techniques are applied to bubble plumes in different ambient conditions.

The problems and errors in the two-phase PIV application to a bubble plume case are addressed through a comparative study between the optical separation method using fluorescent particles and a new phase separation method using vector post-processing. The study shows that the new algorithm predicts well the instantaneous and time-averaged velocity profiles and has errors comparable to those for image masking techniques.

The phase separation method developed in the previous section is applied to study the mean flow characteristics of a bubble plume in quiescent and unstratified condition. The entrainment coefficients representing the mixing properties of a bubble plume are calculated to lie between 0.08 near the plume source and 0.05 in the upper region, and to depend on the non-dimensional quantity $u_s/(B/z)^{1/3}$, where u_s is the bubble slip velocity, B is the initial buoyancy flux, and z is the height from the diffuser.

Further, the LIF technique is investigated to measure the scalar concentration field around a bubble plume in quiescent, unstratified condition. This new application to bubble plumes accounts for light scattering by bubbles using an attenuation coefficient that is proportional to the local void fraction. Measured scalar concentration fields show similar trend in concentration fluctuation to turbulent plume cases.

Finally, the velocity and concentration field measurements using the developed two-phase PIV and LIF methods are applied for a bubble plume in a density-stratified ambient. The turbulent flow characteristics induced by a bubble plume in a stratified ambient water are studied. The plume fluctuation frequency is measured as about 0.1 Hz and compares well to plume wandering frequency measured in unstratified plume cases.

To my family and friends

ACKNOWLEDGMENTS

This work was part of the project: “CAREER: The role of turbulence, coherent structures, and intermittency for controlling transport in multiphase plumes in the environment.” (Grant CTS-0348572) funded by the United States National Science Foundation (NSF).

I sincerely express my thankfulness to my advisor, Dr. Scott A. Socolofsky, for his invaluable guidance and motivation extended to me for my entire degree program. He showed me totally new paradigm as a teacher, leader, and manager while I was working with him. He sacrificed tremendous amount of his time to help me to break through all the obstacles in the course of my study. His passion for his class and researches deeply inspired me to finish my degree and consolidate my foundation to the next step as a professional researcher.

I also would like to extend my gratefulness to my committee members, Dr. Kuang-An Chang, Dr. Hamn-Ching Chen, and Dr. Yassin A. Hassan for their kind words of inspiration and encouragement which I often received during the course of this work. I would like to thank my research mate, Duncan Bryant, for providing me with help to set up and conduct the experiments for this work. I am also thankful to Mr. John Reed for his advice on my experiments and help.

Besides of my research, I am indebted to all my friends for their kind words of consolation and encouragement and for offering their help and advice to enliven my spirit sometimes.

Last but not least, I thank my beloved family and friends in Korea for giving me love, care, and all kinds of support whenever I need from afar.

TABLE OF CONTENTS

CHAPTER Page

LIST OF TABLES

LIST OF FIGURES

CHAPTER I

INTRODUCTION

1.1 Problem Statement

Multiphase plumes can be found in a variety of environmental applications, including bubble plumes occurring in pneumatic breakwaters (e.g. Bulson 1967, Wilkinson 1979, Fenneløp et al. 1991), the underwater spill of oil and gas (e.g. Fenneløp & Sjoen 1980, Milgram 1983, Topham 1975, Yapa et al. 1999, Socolofsky & Adams 2002, Socolofsky & Adams 2003), reservoir reaeration or destratification (e.g. McDougall 1978, Wüest et al. 1992, Zic et al. 1992, Asaeda & Imberger 1993, Lemckert & Imberger 1993, McGinnis et al. 2004, Soga & Rehmann 2004, Wain & Rehmann 2005, García & García 2006), and direct sequestration of liquid CO_2 into deep ocean for mitigating green house gas (e.g. Caulfield et al. 1997, Socolofsky et al. 2002). The plume properties have been investigated in the laboratory for stratification (e.g. McDougall 1978, Leitch & Baines 1989, Asaeda & Imberger 1993, Socolofsky 2001) or unstratified cases (e.g. Kobus 1968, Wilkinson 1979, Fenneløp & Sjoen 1980, Rensena & Roig 2001, Soga & Rehmann 2004, Wain & Rehmann 2005) and in field studies (e.g. Milgram 1983, McGinnis et al. 2004). Previous experimental studies on turbulence and mixing properties in a bubble plume have been made by measuring the bulk parameters, such as volume fluxes (Leitch & Baines 1989, Lemckert & Imberger 1993, Socolofsky & Adams 2003), mean velocity profiles (Kobus 1968, Bulson 1967, Wilkinson 1979, Fenneløp & Sjoen 1980, Milgram 1983, García & García 2006), and density and temper-

---

This dissertation follows the style and format of *Journal of Hydraulic Engineering.*

Table 1.1. Previous experimental studies on bubble plumes

Measured parameters	Measurement methods	Recommendation
Mean velocity profiles	Velocity of air-water mixture by in-situ probes	Need separate information for both phases
Liquid volume flux	Change rate of isopycnal height (density interface)	Small flow structure are ignored
Temperature/salinity/DO	Thermistor/temperature micro structure profiler/CTD profiler	Need direct / non-intrusive measurement of flow properties

ature profiles (Zic et al. 1992, McGinnis et al. 2004, Soga & Rehmann 2004, Wain & Rehmann 2005) as summarized in Table 1.1. But, there are few data to provide detailed full-field information on mixing and flow characteristics around a bubble plume. To understand the mixing mechanism in a bubble plume and interaction between the plume and ambient fluid, it is necessary to have detailed velocity- and concentration-field information around a bubble plume.

1.2 Objectives of Study

The main objective of this study is to conduct a detailed experimental study on a bubble plume using full-field, non-intrusive laser-based experimental techniques in a stagnant, unstratified and stratified ambient. To understand the mean flow characteristics of a bubble plume, the centerline velocity, plume width, and entrainment coefficients of a bubble plume will be measured and calculated on the basis on self-similarity assumption and entrainment theory. Instead of measuring bulk parameters as previous studies, experimental measurement techniques for detailed full-field passive scalar concentration field and velocity vector field will be developed for a bubble plume in a quiescent, unstratified and stratified condition.

1.3 Literature Review

The single-phase flow field can be measured using common image velocimetry methods, such as particle image velocimetry (PIV) and particle tracking velocimetry (PTV). The main concept of these velocimetry methods is to obtain velocity field information by measuring the displacement of passive tracer particles from recorded photographic images at different exposures with a certain time interval. In the case that the number of particle images per unit area is small, it is possible to track individual particles to measure their displacement in a pair of images. This is referred to as PTV. To track correct particles in a pair of images, the size of the search window needs to be specified in the second image of an image pair (Hassan et al. 1992). On the other hand, PIV can be applied to the case of high-particle-concentration images. To measure the displacement of particles, the small windows, which are called interrogation windows, are sampled from the recorded image pairs. Based on the statistical correlation between these interrogation windows, the average displacement of a group of particles is determined (Keane & Adrian 1992). The location of peak correlation value in a correlation field represents the mean displacement of particles in the interrogation window. These image velocimetry methods have been successfully applied to single-phase flow (Adrian 1991).

For application of image velocimetry to multiphase flow, it is very challenging to discriminate velocity information for the continuous fluid and the discrete phases in a measurement since there are multiple tracers in the flow (seeded tracer particles for the continuous phase and bubbles, drops, and particles themselves for the dispersed phase). For two-phase flow, an array of phase discrimination methods have been developed for different stages of the image velocimetry processing algorithm. Discrimination of one phase from the other can be made by generating two different images for each phase using optical separation at the image acquisition stage (Hilgers et al. 1995), applying image processing techniques to a single image containing both phases based on particle image size, brightness or shape (Khalitov & Longmire 2002), or using different properties of statistical cross-correlation peaks of two phase (Delnoij et al. 2000).

In the first method, phase discrimination is at the image recording stage, where two separate images for each phase can be recorded using optical separation methods. Two cameras are needed to capture the dispersed phase and the continuous phase from the same field of view. The first camera is usually equipped with an optical filter to block the light reflected from the dispersed phase and record only the fluoresced light from the seeded fluorescent particles for the fluid phase (Sridhar et al. 1991, Hilgers et al. 1995, Deen 2001). The second camera is used to capture the dispersed-phase image. For recording the dispersed-phase image, a light emitting diode (LED) panel can also be used as a shadowgraphy method (Liu & Adrain 1992, Tokuhiro et al. 1998, Lindken & Merzkirch 1999). PIV and PTV methods are applied to these separated seeded particle and bubble images, respectively. These optical separation methods work better than other phase separation methods (Deen 2001, Bröder & Sommerfeld 2002). However, bubbles also reflect the fluoresced light from the seeded particles so that the weak bubble images still remain in the separated fluid-phase image (Brücker 2000, Lindken & Merzkirch 1999). In addition, these methods require complicated experimental setup and expensive fluorescent particles (Khalitov & Longmire 2002).

The second method uses image processing techniques to extract two separate images for each phase from a single image containing both dispersed phase and fluid phase tracers. Only one camera is required for imaging dispersed phase and fluid phase together on a single field of view. The recorded image can be separated into two separate images using image processing techniques, such as median filtering (Jakobsen et al. 1996, Kiger & Pan 2000), edge detection (Song et al. 1999, Brücker 2000), digital masking (Gui & Merzkirch 1996, Gui et al. 1997), utilization of differences in image brightness between bubbles and tracer particles (Sakakibara et al. 1996), both size and brightness difference (Khalitov & Longmire 2002), or shape of spot in a raw image (Oakley et al. 1997) prior to applying PIV or PTV. These single-image phase separation methods using image processing work very well for solid dispersed phase particles with sufficient size, but the different light scattering properties of bubbles makes it difficult to apply these image processing techniques to a bubble plume. These methods also require complex image processing algorithms that take expensive CPU time.

For the third method, phase separation can be made in the PIV calculation stage using the cross-correlation function. The ensemble cross-correlation PIV based on the single-frame double-exposure image is used to detect two different peaks in the cross-correlation field (one for the dispersed phase and another for fluid phase) (Delnoij et al. 1999). Rottenkolber et al. (1999) discriminate the phases based on the height and width of the two peaks in the cross-correlation field. In order to get these methods to work, the bubble phase and fluid phase should remain in the same interrogation area between exposures and the two phases should have significant velocity difference. For the ensemble cross-correlation PIV, it is impossible to obtain instantaneous velocity information because several correlation fields should be averaged to detect two different peaks for both phases (Bröder & Sommerfeld 2002).

Table 1.2 summarizes previous studies of multiphase PIV based on which stage of the single-phase PIV algorithm their method is applied and details the identified problems with the previous methods. In the first part of this dissertation (Chapters II and III), a new approach for phase separation is presented to apply PIV measurement techniques to a bubble plume based on post-processing of mixed phase PIV vector

Table 1.2. Previous PIV studies on multiphase flows

Single-phase PIV	Multiphase PIV	Problems
Image Acquisition	Optical separation, shadowgraphy	Expensive, complicate setup
Image Processing	Digital masking, median filter, size/brightness difference	Different optical characteristics of bubbles
Velocity evaluation	Ensemble correlation, Correlation peak width difference	No instantaneous, two phases in same measurement area

maps. Although the optical separation methods are regarded more reliable than other phase separation methods (Deen 2001, Bröder & Sommerfeld 2002), it is desired to have a cheaper and easier method to avoid the complex and expensive setup for the optical separation methods. Since the phase separation is made in the vector post-processing, the proposed method does not require complicated experimental setup or additional change in PIV algorithm. The application limits of the proposed method are also explored by comparing to optically separated data.

In the second part of the dissertation (Chapter IV), quantitative measurements on concentration field of a bubble plume plume have been conducted in unstratified ambient condition. A detailed understanding of turbulent mixing behavior in bubble plume relies on a quantitative description of the spatial structure of the scalar field. The planar laser-induced fluorescence (PLIF) can be used in single-phase flow to quantify the scalar concentration field as well as to visualize the flow structure quantitatively. PLIF uses a fluorescent dye (e.g. Rhodamine 6G, Rhodamine B, etc.) as the scalar quantity. These types of fluorescent dye emit a certain range of wave-length light when it is exposed to laser light. The amount of emitted fluoresced light is linearly proportional to the concentration of dye at any local point when the dye concentration is kept low enough (Ferrier et al. 1993). This scalar measurement technique has been used in studying turbulent mixing around single-phase jets and plumes (e.g. Koochesfahani & Dimotakis 1985, Dahm & Dimotakis 1986, Ferrier et al. 1993, Chen & Jirka 1999, Tian & Roberts 2003, Webster et al. 2003). All these previous authors applied LIF methods to measure the temporal and spatial distribution of passive scalar tracer in single-phase flows.

In multiphase flow, it is difficult to measure the whole concentration field in a bubble plume since the bubbles reflect the laser light and create shadows behind bubbles. Only a few studies have applied fluorescence techniques to multiphase flows. Socolofsky (2001) measured the fluorescence profile in a tank around a bubble plume after stopping injecting bubbles with an *in-situ* point-measurement fluorometer to provide direct measurements of the average liquid fluxes. In Roy & Duke (2004), the fluorescence was used to directly represent the oxygen concentration around a single bubble. They measured concentration profiles around a single bubble and provided the oxygen transfer rates through a bubble surface using a fluorescent tracer that reacts with oxygen. This can be extended to the case of a group of bubbles as in a bubble plume. However, it is still necessary to take into account the change of flow properties by a group of bubbles and the light scattering characteristics by the bubbles in measuring concentration field in a bubble plume.

The third part of the dissertation (Chapter V) presents experiment results on a bubble plume in density-stratified condition. To apply the laboratory experimental results to real situations, density stratification should be taken into account. The strength of density stratification is a very important parameter along with buoyancy flux in classification of the characteristic behavior of a bubble plume (Asaeda & Imberger 1993). Socolofsky & Adams (2005) showed that the plume behavioral properties are also dependent on the slip velocity of the dispersed phase. Depending on the type of plume behavior, the eddy structure also has different properties, where small eddies play an important role in entraining the surrounding water (Asaeda & Imberger 1993). This observation on eddies demonstrates that the plume is made up of a series of rising and falling coherent eddy structures. It can be presumed that both the dispersed phase and the continuous phase have their own coherent structures, and the entrainment and detrainment in a plume take place by the interaction of these coherent structures. The measured full-field velocity information for both phases is to be required to find out the correlation between the dispersed phase and the entrained ambient fluid phase. In addition, measurement on scalar concentration field can provide better insight on the mixing mechanism around a bubble plume in a stratified ambient.

1.4 Dissertation Organization

The dissertation is organized as follows:

- In Chapter II, the standard particle image velocimetry (PIV) technique is extended to study a bubble plume. By comparing to widely-used two-phase PIV methods, such as optical separation and image post-processing techniques, the applicability of the proposed phase-separation method using vector post-processing is tested.
- In Chapter III, the developed vector post-processing method is applied to a bubble plume in unstratified ambient to study mean properties and entrainment characteristics of a bubble plume.
- In Chapter IV, The laser-induced fluorescence (LIF) technique is investigated to measure the scalar concentration field around a bubble plume in quiescent,

unstratified condition. Measured scalar concentration fields are used to quantify the mixing mechanism around a bubble plume.

- In Chapter V, the velocity and concentration field measurements using the developed two-phase PIV and LIF methods are applied for a bubble plume in density-stratified ambient. The turbulent flow characteristics induced by a bubble plume in a stratified ambient water are studied.

Chapter II has been published in *Experiments in Fluids* (Seol & Socolofsky 2008). Chapter III has already been published in *Journal of Engineering Mechanics* (Seol et al. 2007). LIF measurements in a bubble plume of Chapter IV have been submitted to *Experiments in Fluids* for review. Parts from Chapter V are the subject of a publication in preparation.

CHAPTER II

VECTOR POST-PROCESSING ALGORITHM FOR PHASE DISCRIMINATION OF TWO-PHASE PIV[1]

2.1 Introduction

Single-phase particle image velocimetry (PIV) has been adapted through recent studies to measure the in-plane velocity field of multiphase flows. These applications of PIV to multiphase flows are frequently referred to as two-phase PIV and are reviewed comprehensively in Brücker (2000) and Deen et al. (2002*a*). Discrimination of one phase from another can be made in several ways, such as by generating two different images for each phase using optical separation (e.g. Hilgers et al. 1995), applying image processing techniques to a single image containing both phases to remove one phase based on particle size, brightness, or shape (e.g. Khalitov & Longmire 2002), or using the different properties of the statistical cross-correlation peaks in the PIV calculation to extract results for one of the phases in a mixed-phase image (e.g. Delnoij et al. 1999).

In the two-phase PIV application to a bubble plume, however, the light scattering properties of the bubbles make some of these techniques difficult (Bröder & Sommerfeld 2002). Moreover, these methods can be very expensive, time consuming, or require specialized PIV software. This paper presents a simple approach for phase separation in bubble plumes using PIV vector post-processing techniques introduced

---

[1] Reprinted with permission from "Vector post-processing algorithm for phase discrimination of two-phase PIV" by Seol & Socolofsky (2008). *Experiments in Fluids*, DOI 10.1007/s00348-008-0473-9, Copyright[2008] by Springer.

by Seol et al. (2007). The method requires a discernible slip velocity between the continuous and bubble phases and uses particle tracking velocimetry (PTV) analysis for real-time validation of the post-processing algorithm. Though more rigorous methods exist, the development of this simple, inexpensive approach to phase separation in bubble plumes is useful in order to apply PIV methods economically to large scales, where multiple, simultaneous fields of view are required. The resulting data also shed light on bubble plume physics, including the interactions between the two phases, and provide needed information for validation of computational fluid dynamic models. Environmental applications of bubble plumes occur in many situations, such as for reservoir aeration and destratification, breakwaters and ice prevention in harbors, direct sequestration of liquid carbon dioxide in the oceans, and tracking of oil and natural gas released in accidental oil-well blowouts (Socolofsky & Adams 2005).

Many previous experimental studies on bubble plumes have focused on the plume bulk properties, such as volume fluxes, mean velocity profiles, and density and temperature profiles of the ambient reservoir fluid. Leitch & Baines (1989) and Socolofsky & Adams (2003) studied the plume structure in the laboratory by measuring bulk liquid volume fluxes for a bubble plume in stratified ambient conditions. Since the average vertical velocities of density interfaces were measured to study the liquid volume flux in the bubble plume, small structures of the flow were ignored. Similar techniques have been applied at the field scale by Lemckert & Imberger (1993) and by McGinnis et al. (2004). In unstratified conditions, mean velocity profiles in bubble plumes have also been measured using intrusive propeller velocimeters to study flow properties and entrainment (Kobus 1968, Milgram 1983, Wilkinson 1979). These studies found the mixed-fluid velocity profile to follow the Gaussian distribution and provided the framework for the development of integral plume models (Cederwall & Ditmars 1970, Milgram 1983). Though these studies can infer the entrainment properties from measurements of the net volume flux, the details of the turbulent structure are lost. Recently, non-intrusive PIV measurements using optical separation were applied to large-scale laboratory bubble plumes in a confined tank by Simiano et al. (2006).

Data for the bubble and fluid velocity were obtained in separate experiments and were analyzed statistically to give a rich database of information on bubble plume wandering and turbulence characteristics. Other recent studies have investigated the interaction between the bubbles and entrained fluid for two-dimensional bubble plumes, focusing on the development of plume wandering in response to eddies in the continuous phase and comparing meander characteristics between laboratory and numerical experiments (Bech 2005, Díaz et al. 2006, Zhou et al. 2006). In these studies, simultaneous velocity information for both phases was also lacking. However, to understand the mixing mechanisms in a bubble plume (entrainment) and the large-scale interaction between the plume and ambient fluid (wandering), it is desirable to have detailed, instantaneous full-field velocity information simultaneously and separately for each phase over a large scale in the bubble plume. The objective of the present study is to evaluate a simple phase discrimination method for PIV data in a bubble plume in order to study the instantaneous and time-averaged properties of flow in the plume. The simplified approach for phase separation is based on a post-processing algorithm introduced by Seol et al. (2007) that is applied to mixed-phase PIV vector maps. The validity and application limits of the post-processing algorithm are studied in this paper by comparing to synoptic data obtained by optical separation and by digital masking techniques.

In the following section, Section 2.2, we discuss the previous studies of two-phase PIV methods and the particular difficulties encountered in the bubble plume case. In Section 2.3, we present details of the experiments, the data processing, and the post-processing phase discrimination algorithm. In Section 2.5, we analyze data to demonstrate the applicability of the post-processing method, followed by measurements of plume wandering, time-averaged velocity profiles, and probability distributions of instantaneous eddy size for the continuous phase data in Section 2.6.

2.2 Review of Two-Phase PIV Methods

Phase separation schemes for two-phase PIV have been developed using a diverse range of techniques. For a regular PIV application to single-phase flow, the seeded tracer particles in the flow are illuminated by a pulsed laser light sheet with a precise timing interval. First, images of the tracer particles are recorded using a CCD camera or video camera. Second, the recorded images are analyzed with statistical cross-correlation applied to sub-image interrogation windows to obtain the velocity vector of the flow at each interrogation window. Third, vectors are post-processed to remove errant results. For two-phase flow, different phase discrimination methods have been developed that are applied at each stage of this standard PIV algorithm. At the image acquisition stage, two different images can be obtained using optical separation. The flow is seeded with fluorescent tracer particles, and two cameras are needed for each field of view to capture separate images of the tracers for the dispersed and continuous phases. The first camera is equipped with an optical filter to block the light reflected from the dispersed phase and records only the fluoresced light from the tracer particles for the fluid phase (Deen et al. 2002*a*, Hilgers et al. 1995, Sridhar & Katz 1995). The second camera is used to capture the dispersed-phase image either using a filter to remove the fluorescent particles or by adjusting the laser power so that the fluorescent particles are much darker than the dispersed phase (Lindken & Merzkirch 1999, Liu & Adrain 1992). For recording the dispersed-phase image, a light emitting diode (LED) panel can also be used in a shadowgraphy method (Tokuhiro et al. 1998). Regular PIV and PTV methods are applied separately to these seeded particle and bubble images. In general, these optical separation methods work better than other phase separation methods (Bröder & Sommerfeld 2002, Deen 2001). However, because bubbles reflect the fluoresced light from the seeded particles, weak bubble signatures still remain in the separated fluid-phase image (Brücker 2000, Lindken & Merzkirch 1999). In addition, these methods require complicated and expensive setups, especially when multiple fields of view are required to capture the flow field (Khalitov & Longmire 2002). If optical separation is not used, a single image is obtained during acquisition that contains tracers for both phases together. The advantage is that only one camera is required for each field of view. The recorded image can be separated into two images, one for each phase, using image processing techniques, such as median filtering (Jakobsen et al. 1996, Kiger & Pan 2000), edge detection (Brücker 2000, Song et al. 1999), digital masking (Gui et al. 1997, Gui & Merzkirch 1996), utilization of differences in image brightness between bubbles and tracer particles (Sakakibara et al. 1996), both size and brightness differences (Khalitov & Longmire 2002), or shape of a spot in a raw image (Oakley et al. 1997). Once the image separation is achieved, the regular PIV or PTV algorithm is applied to each phase separately. These image processing techniques work well for solid dispersed-phase particles having sufficient size compared to the fluid-phase tracer particles, but the different light scattering properties of bubbles make it difficult to apply some image processing techniques to a bubble plume. Fig. 2.1 illustrates examples of the application of three common image processing techniques to a sub-region of the bubble plume in the mixed-phase PIV images from our experiments. Four bubbles are observed in the selected sub-region and are numbered in each frame. Two of the image processing techniques, the Khalitov & Longmire (2002) and median filtering

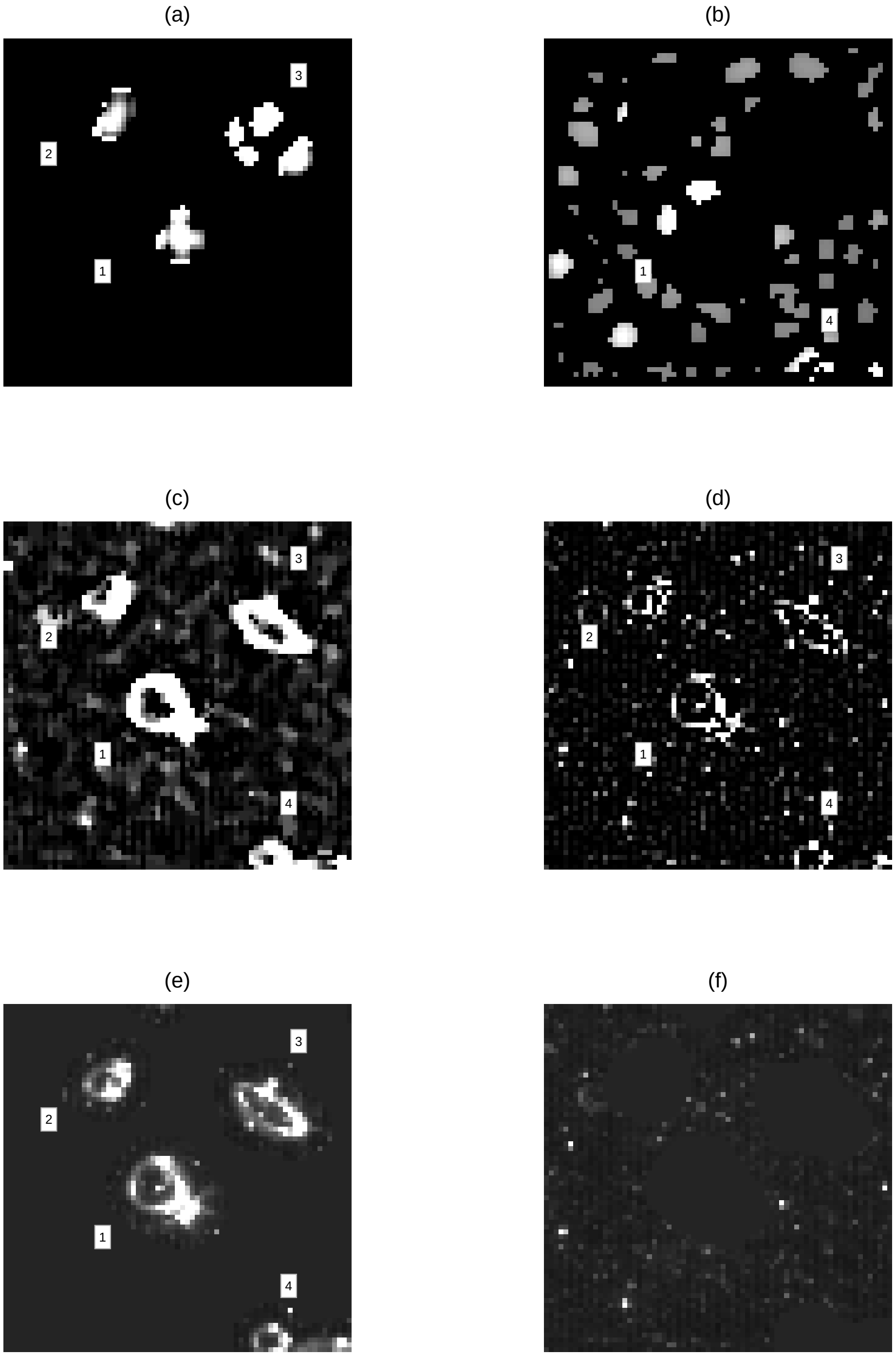

Fig. 2.1. Application of image-processing techniques to a sub-region of a mixed-phase image in a bubble plume: (a) bubble phase and (b) fluid phase by Khalitov & Longmire (2002), (c) bubble phase and (d) fluid phase by median filtering (Kiger & Pan 2000), and (e) bubble phase and (f) fluid phase by image masking.

methods (Kiger & Pan 2000), do not produce complete phase separation. The Khalitov & Longmire (2002) method removes the continuous-phase tracers from the bubble image (a), but signatures of bubbles 1 and 4 remain in the continuous-phase images (b). This is due to the fact that the bubbles appear as halos with dark centers and complex light and dark regions on their boundaries. The median filter method neither removes tracer particles from the bubble image nor removes bubbles from the continuous-phase image. We note that both these methods perform well for solid dispersed phase particles. The final method illustrated in the figure is based on digital masking techniques (Gui & Merzkirch 1996) and is described in more detail in Section 2.4. The method accurately filters all four bubbles from the continuous-phase image. Because of a buffer region around each bubble needed to extract a complete bubble, a few continuous phase tracer particles are extracted with the bubble-phase image. As a result, the continuous-phase data can be analyzed without interference from the bubbles; whereas, the bubble-phase images may require additional processing to remove the remaining fluid-phase tracer particles before PTV analysis. If phase separation is not achieved before PIV processing, the differing statistical correlation properties of the tracer particles for the dispersed and continuous phases may be used to obtain separate velocity information for each phase during the PIV computation. Rottenkolber et al. (1999) discriminate the phases based on the height and width of the peaks in the cross-correlation field for a fuel spray. However, it is necessary to specify proper cut-off cross-correlation peak heights and widths to discriminate the dispersed and continuous phases (Khalitov & Longmire 2002). Delnoij et al. (1999) apply the ensemble correlation PIV to doubly-exposed single-frame images to detect two different peaks in the correlation field, one for each phase in the flow. Since several instantaneous correlation fields must be ensemble-averaged to obtain better detection probability for the bubble-phase correlation peak, it is not easy to obtain instantaneous velocity information for a bubble plume (Bröder & Sommerfeld 2002). In addition, the bubble phase and fluid phase must remain in the same interrogation area between exposures, and this does not always happen. When none of the above techniques are employed, phase separation must be made after all the velocity vectors are computed together. The method evaluated in this paper uses vector post-processing to achieve this task. Although the optical separation methods are regarded as more reliable than other phase separation methods (Bröder & Sommerfeld 2002, Deen 2001), it is desirable here to have a cheaper and simpler method that reduces the setup complexity and expense compared to the optical separation method. In addition, since the phase separation is made in the vector post-processing stage, the proposed method does not require any change from the classical PIV algorithm or sophisticated image processing. The vector post-processing algorithm does, however, rely on a significant velocity difference between the two phases and requires a relatively dilute plume (low void fraction). The purpose of this study is to evaluate the accuracy and range of applicability of this vector post-processing algorithm, to validate it against synoptic data obtained using optical separation and digital masking methods, and to apply these data to study coherent structures and the entrainment properties of bubble plumes.

2.3 Laboratory Methods

Fig. 2.2 shows a schematic diagram of the setup for our PIV/PTV experiments, conducted in the Ocean Engineering Wave Tank Laboratory at Texas A&M University. The setup is similar to that described in Seol et al. (2007), but expanded here to allow for optical separation in a single, small-scale field of view. A Plexiglas tank with dimension of 38×38×80 cm was used in the experiments. A double-pulsed Nd:YAG laser (Spectra-Physics Quanta-Ray PIV-400, 400 mJ/pulse at a wavelength of 532 nm) was used to generate a two-dimensional planar light sheet using a combination of spherical lenses. Two Basler cameras (10 bit image depth with 1004×1004 pixel resolution) were used to record the raw images. Both cameras were equipped with Nikkor 50 mm focal length lenses. The fields of view of each camera were 15×15 cm. A pulse generator (Berkeley Nucleonics Corporation, Model 500A) was employed to externally trigger the laser. The pulse generator and the two cameras were synchronized using LabVIEW and a National Instruments PCI-6713 analog signal output board (12 bit by 8 channels). Since the laser operation frequency was 8 Hz, the image acquisition frequency of double-frames was 4 Hz. The air was injected from a standard aquarium airstone diffuser having a diameter of 1.4 cm and which was fixed to the bottom of the tank. A needle valve and gas mass flow meter (Alborg GFM 171) enabled precise control of the air flow rate from the air source. Bubble sizes for each air flow rate were estimated by interrogation of the camera images. The slip velocity of bubbles, defined as the terminal rise velocity of a single bubble in static, ambient fluid, was estimated from correlation equations in Clift et al. (1978). Experimental conditions are listed in Table 2.1. As a passive tracer particle to represent the fluid phase, fluorescent particles obtained from the Laboratory for Experimental Fluid Dynamics at Johns Hopkins University were seeded before acquiring the PIV images. The fluorescent particles contained Rhodamine 6G and dichlorofluorescein with a size distribution of 20 to 100 μm. The specific gravity of the particles ranged from 0.92 to 1.1.

The fluorescent particles absorb the green laser light and have a peak emission wavelength in the orange range near 585 nm. For the dispersed phase, the bubbles themselves were used as tracer particles. To collect both mixed-phase and optically-filtered data, two CCD cameras were employed to synoptically image the bubble

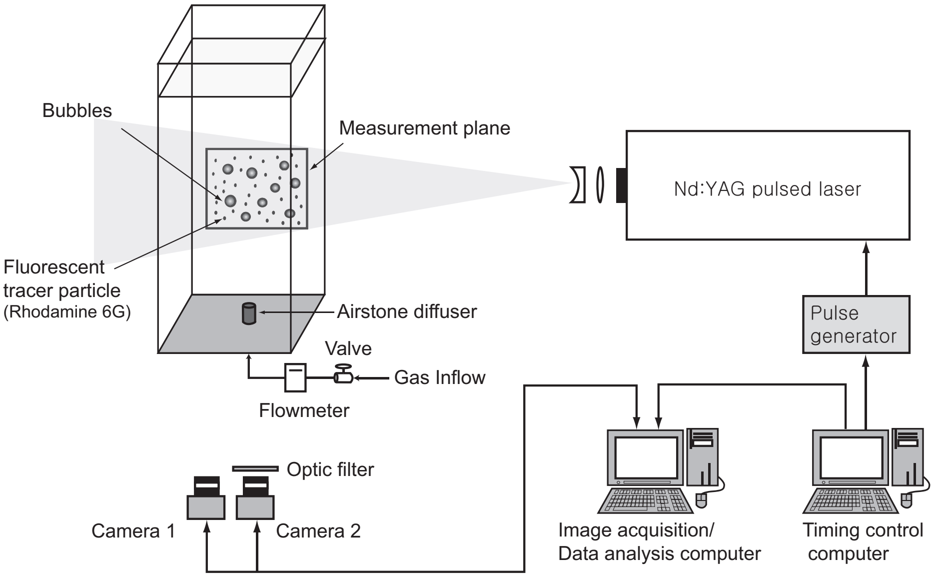

Fig. 2.2. Experimental setup.

Table 2.1. Air sources used in the experiments and their properties.

Dispersed phase	Injection method	Mean diameter [μm]	Slip velocity [m/s]	Flowrate [l/min]
Air	airstone diffuser	1510	0.167	0.5
Air	airstone diffuser	1710	0.183	1.0
Air	airstone diffuser	2020	0.204	1.5

plume over the same field of view. One camera was equipped with an orange optic filter (Kodak Wratten gelatin filter No. 22) to effectively block the original laser light and transmit the fluorescent light from the continuous phase tracer particles. The second camera had no optical filter and was used to capture mixed-phase images containing the dispersed and continuous phases. Though it is desirable to use optical image splitting methods to provide the same image to both cameras, these optics were not available, and the cameras imaged the same field of view from slightly different angles. The overlapping fields of view of the two cameras were geometrically corrected for image distortion using images of a single calibration grid plate based on the image dewarping algorithm (Willert 1997). Image correction was made before the PIV processing so that vector maps from the two cameras could be calculated on identical grids. As indicated from previous research (Bröder & Sommerfeld 2002), careful adjustment of the laser power and camera aperture are needed to capture images of the desired tracer particles in the first camera and mixed phase images in the second camera. For our experiments, the optically-filtered camera had an f-stop of 2.0 and the mixed-phase camera was set to an f-stop of 4.0. Based on a previous study by the authors (Seol et al. 2007), the bubbles released from the airstone diffuser rise with a total velocity of approximately 40 cm/s, which is the summation of the mean fluid velocity and the slip velocity. Thus, the time interval between image pairs was chosen as 4 ms in order to have an average bubble displacement of around 10 pixels. 600 double frames were recorded for a total data duration of 150 seconds. The recorded images were processed with the regular PIV algorithm using the DaVis program, Version 6.0 (LaVision GmbH 2002).

2.4 Data Processing

Three different phase separation methods were compared to study the application range of the vector post-processing method. These were optical separation, yielding PIV data for the fluid phase only, digital masking applied to the mixed-phase images, yielding PIV data for the fluid phase and PTV data for the bubble phase, and vector post-processing, yielding vector fields for the fluid and bubble phase separated from PIV analysis of the mixed-phase images. Because the vector post-processing method is intended to be a stand-alone method, the optically-separated and image-masked data cannot be used to calibrate the parameters of the vector post-processing algorithm. As a result, a fourth data set was obtained by segmenting the mixed-phase image at a threshold light intensity to remove the tracer particles and then applying PTV to the obtained bubble signatures.

2.4.1 Optically Separated Data

Raw images of the continuous phase tracer particles obtained from the optically-filtered camera were processed using the regular PIV algorithm to obtain the fluid-phase velocity fields (called optic filtered data in the remainder of this paper). The PIV algorithm calculates the average displacement of a group of tracer particles in divided small interrogation areas from successively recorded double-frame images using cross-correlation. Although fluorescent light emitted by the tracer particles reflects off the bubbles, bubble signatures were not significant in the optically filtered images due to careful adjustment of the laser power and camera lens aperture (Bröder & Sommerfeld 2002). We employed an adaptive multi-pass PIV process using interrogation windows of 32×32 pixels at the first pass and 16×16 pixels in the second pass with 50% overlap at each pass. Each interrogation area contained about three to five tracer particles at 16×16 pixel grid resolution, and the data yield rate was 95%. Spurious vectors were removed using the vector median filter. Typically, 2 to 5% of the vectors are removed from this median filtering process. Hence, the optically separated data provide an important validation database for comparison to the remaining two phase separation methods.

2.4.2 Digitally Masked Data

To obtain a second set of validation data (called in the remaining paper the image masked data), image masking techniques were applied to the mixed-phase images to separate the phases before PIV processing. The image masking algorithm was programmed using the Matlab® Image Processing Toolbox. The goal of the image mask is to identify the bubble signatures so that they can be separated from the image. The first step was to apply a two-dimensional median filter with a 3×3 pixel footprint to remove noise. The image was then segmented at a low threshold level (5% of the peak intensity) to convert it to a binary image containing both bubbles and fluorescent tracer particles. The bubbles were identified using the binary area-open algorithm with a threshold of 30 connected pixels to define a bubble signature. The bubbles obtained in this way appeared as halos because of the dark centers present for the bubbles in the raw images. These halos were filled-in using the area-close algorithm. Because of the 5% threshold used to create the binary image, the true edge of the bubble is outside the region obtained so far in the binary image. To correct this problem, the image dilation algorithm was applied to the binary bubble structures to create the final image mask. The original image was then multiplied by the image mask appropriately to separate the bubble and fluorescent particles into two images. In the tracer particle image, the missing bubble regions were filled with background noise instead of pure black so that the PIV algorithm is not biased by the missing bubble regions. Fig. 2.1(e) and (f) show the results of applying this technique to a sub-region of the mixed-phase image. The regular PIV algorithm with multi-pass parameters identical to the optically filtered data was applied to the tracer particles; PTV was applied to the bubble data and projected on an 8×8 grid to match the coverage of the PIV data. The vector median filter was also applied, as for the optically separated data, to remove bad vectors with similar data rates. Hence, the image masked data provide a high-quality validation data set that does not require image correction in order to compare to phase separated data based on the vector post-processing algorithm.

2.4.3 Vector Post-Processed Data

The PIV process with multi-pass parameters identical to the optically filtered data was also applied to the mixed-phase images to obtain mixed-phase velocity fields. Because the bubbles and fluorescent tracer particles produce different peaks in the cross-correlation function, true velocities for each are obtained in the PIV images there is no bias introduced by having both phases together. However, there is no control over whether a bubble- or fluid-phase velocity vector is obtained at a given point, so that vector post-processing, described below, is required to separate the mixed-phase velocity field into separate fields for bubbles and entrained fluid. Bad vectors were removed using the same median filter parameters as for the image masked data. The difference between this data set and the others, however, is that both bubble and continuous phase velocity vectors are contained in the vector map. The median filter used takes secondary peaks in the PIV cross-correlation field into consideration, and a few vectors identified as bubbles may be replaced by the local fluid phase velocity. This does not occur for the majority of bubble vectors because of the chose field of view, in which each bubble is represented by many vectors in the vector map. Hence, there is a low likelihood that a bubble vector would be selected for replacement by the median filter. In addition to PIV processing, the mixed-phase images were processed with the PTV algorithm to obtain velocities of individual bubbles. Before running the PTV process, the two-dimensional median filter was applied to a raw image to remove noise and reduce the intensity of the fluorescent tracer particles. Because the remaining bubble signatures are normally brighter than the tracer particles, a grayscale intensity threshold (150 to 200 out of 1024 image intensity levels in this study) was used to remove the remaining continuous phase tracers. For the PTV process, it is necessary to specify the allowable vector range, which sets limits on the search range for possible locations of particle intensity peaks (LaVision GmbH 2002). This allowable vector range was set as 5 to 12 pixels for the given time interval by visually inspecting pixel displacement of bubbles in a pair of raw images. These PTV velocity data for the bubbles were then used to calibrate the parameters of the vector post-processing algorithm applied to the mixed-phase PIV data. The fluid-phase velocity vector field was obtained from the mixed-phase PIV result by removing the unwanted dispersed-phase vectors from the mixed-phase PIV data using a velocity threshold and vector median filter, following the algorithm introduced by Seol et al. (2007). In the first pass, dispersed-phase vectors are identified by selecting all vectors above a threshold velocity U_{max} specified for the continuous phase. It was observed in the PTV data that bubble velocities near the edge of the plume were more variable than those in the center. In Seol et al. (2007) a constant value of U_{max} was used. In the present study, a variable velocity threshold was obtained by calculating radial averages and standard deviations from the 600 PTV vector maps as depicted in Fig. 2.3. We then define the velocity threshold as

$$U_{max}(r) = \bar{U}(r) + k\sigma(r) \tag{2.1}$$

where $\bar{U}(r)$ and $\sigma(r)$ denote the average velocity and the standard deviation of the velocity along the radial direction, and k is a parameter that is adjusted to achieve the correct phase separation. After applying the variable velocity threshold, some bubble vectors remain in the fluid-phase result, especially on the edges of the plume where the continuous phase velocity is low and the slip velocity of the bubbles may be below the velocity threshold. The remaining bubble vectors are filtered out using the regional vector median filter (LaVision GmbH 2002). The vector median filter determines the range of allowable vectors according to the rule

$$U_{med} - fU_{rms} \leq U \leq U_{med} + fU_{rms} \tag{2.2}$$

where U denotes the allowed vector components and U_{med} and U_{rms} denote the median and standard deviation of all neighboring vector components, respectively. The parameter f for the median filter is specified to adjust the allowable vector range. DaVis 6.0 applies the median filter using several passes. In the first pass, Eq. (2.2) is used to identify potential bad vectors. In the second pass, all vectors that have fewer than n neighboring good vectors are also identified as potential bad vectors. The third pass through the data replaces some of the identified bad vectors by new vectors given by the second or third highest peaks in the PIV cross-correlation function, dependent on whether these peaks better fit the local trends in the velocity. The final pass rechecks the number of neighboring good vectors. To calibrate the final values of U_{max}, f, and n, comparison is made between the PTV data obtained from the mixed-fluid images and the bubble-vectors removed by the vector post-processing algorithm. When the best match is obtained between the two data sets, those calibrated values of the separation algorithm parameters are determined. In this paper, the optimal match is obtained when the root mean square difference between the PIV and PTV bubble-phase velocity data averaged over one representative image is minimized. The

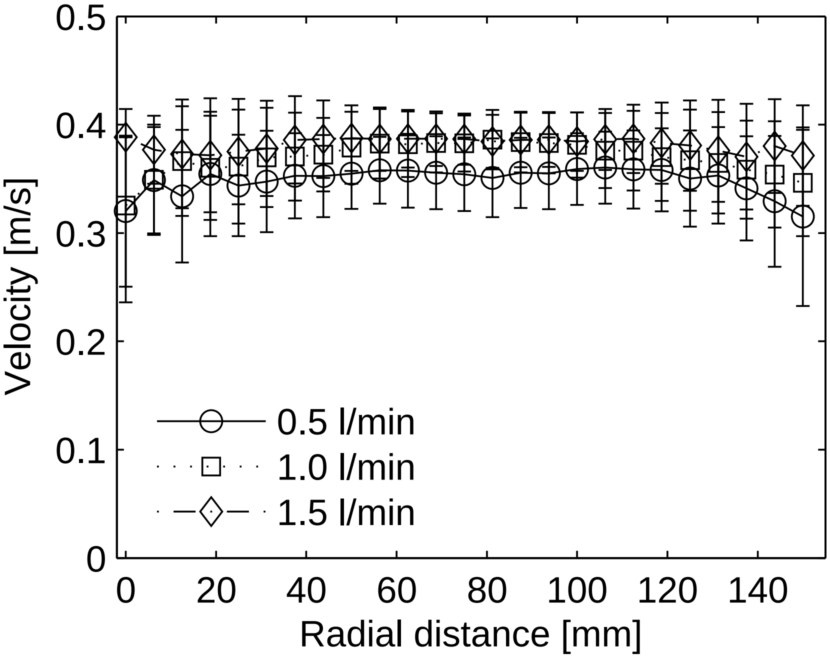

Fig. 2.3. Time-averaged bubble phase velocity from PTV used to specify the radial velocity threshold. Error bars represent plus and minus one standard deviation of the measured velocities.

full data processing algorithm is summarized in the flow chart as shown in Fig. 2.4. In this paper, we evaluate the phase discrimination method to determine its reliability. A potential application of this method beyond the scope of this paper would be to use the identified bubble velocity vectors to reevaluate the cross-correlation field to search for secondary peaks that could fill in the continuous phase data in a method similar to Delnoij et al. (1999).

2.4.4 Reliability and Validation of Data

The reliability of the PIV data depends on many factors, including the number of tracer particles, the interrogation window size, the image resolution, the presence of particle displacements normal to the light sheet, the velocity gradients, and the

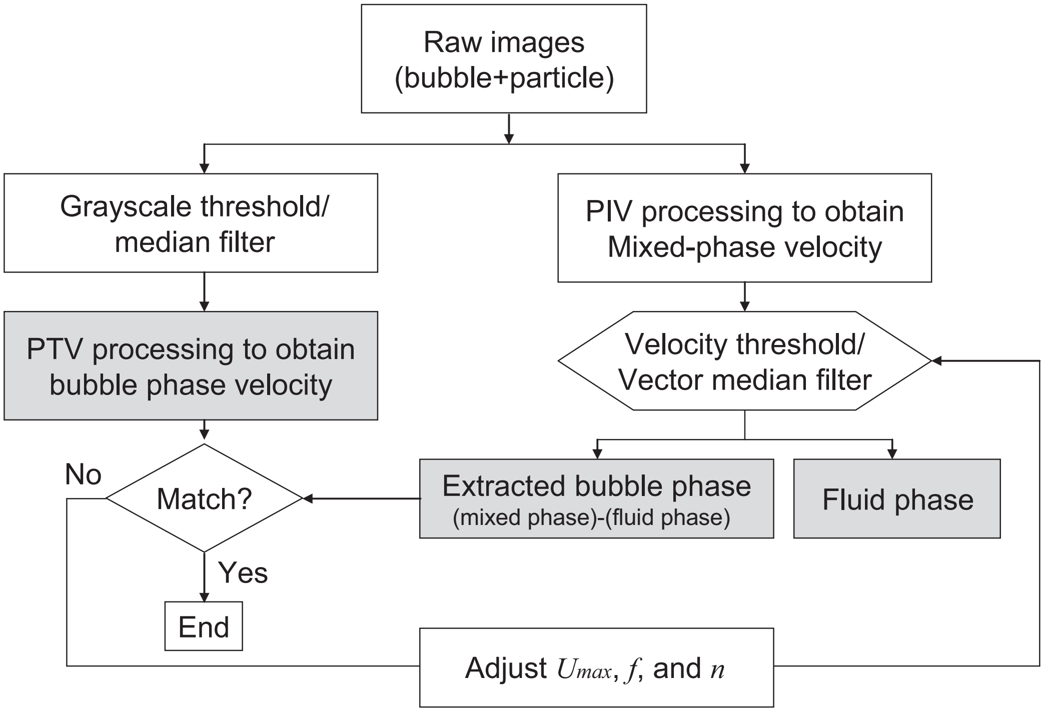

Fig. 2.4. Flowchart for vector post-processing algorithm applied for phase discrimination of the mixed-phase PIV vector maps.

image quality, among others (Raffael et al. 1998). One challenge in this study was to achieve uniform lighting characteristics in both the optically-filtered data and the mixed phase data. In fact, the mixed phase data had higher lighting quality on the side of the plume opposite the laser; whereas, the optically-filtered data were darker on the far side of the plume due to laser attenuation through the bubbles. Nonetheless, all images had adequate lighting and seeding density for the interrogation window sizes selected for this study. If larger interrogation windows were used, the mixed-phase PIV data would have more bubble vectors, and therefore, fewer continuous phase velocity vectors could be obtained. To validate the mixed-phase vector post-processing algorithm, velocity errors between the various phase separation methods are calculated as a function of the plume radial direction. For the comparison, the optically-filtered data and the digitally-masked data were considered as reference data. The averaged velocity errors E_i for one velocity component are defined similarly to Hu et al. (1998) as

$$E_i = \frac{\sum_{j=1}^{N} \sqrt{\left(V_{ij} - \hat{V_{ij}}\right)^2}}{\frac{1}{M}\sum_{i=1}^{N}\sum_{j=1}^{M}\sqrt{V_{ij}^2}} \tag{2.3}$$

where V is the reference velocity, $\hat{V}$ is the corresponding velocity obtained from the vector post-processing algorithm, and i and j are indices that cycle through the radial and vertical directions, respectively. N and M are the number of vectors in the radial and vertical directions. Hence, the error statistics are computed along vertical averages for individual images.

2.5 Results and Discussion

Results for the evaluation of the vector post-processing algorithm for phase discrimination are presented in this section for the analysis of an unconfined bubble plume. The phase discrimination method is validated by comparison to synoptic optically-filtered and image-masked data for both the instantaneous and time-averaged velocity fields.

2.5.1 Phase Discriminated Data

For the calibration of the parameters of the vector post-processing algorithm, comparison is made between the post-processed data and the PTV data obtained from the mixed-fluid images. Fig. 2.5 shows a typical comparison between the two data sets for one cross-section through the plume for a gas flow rate of 0.5 l/min. The data from the optical and image-mask methods are also shown for reference. For the plots in the figures, only every third data point is plotted to improve visual clarity, and the calibrated values of the phase-separation method parameters were k = -1, n = 3, and f had a value of 0.35 in the first pass of the median filter and 1.5 in the third pass. These optimal values were the same for all three gas flow rates investigated here.

For the most part, the optically-filtered and post-processed data agree, which, as anticipated, indicates that the presence of the bubbles in the mixed-phase images does not bias the velocity estimates. A few erroneous vectors in the range of 0.2 to 0.3 m/s appear in both the bubble and continuous phase results for the post-processed data in Fig. 2.5. These vectors represent both continuous phase vectors incorrectly attributed to the bubble phase (sub-plot (a)) and bubble velocity vectors that could not be identified by the vector post-processing algorithm and remain in the continuous phase data (sub-plot (b)). This is due to the unsteady nature of the

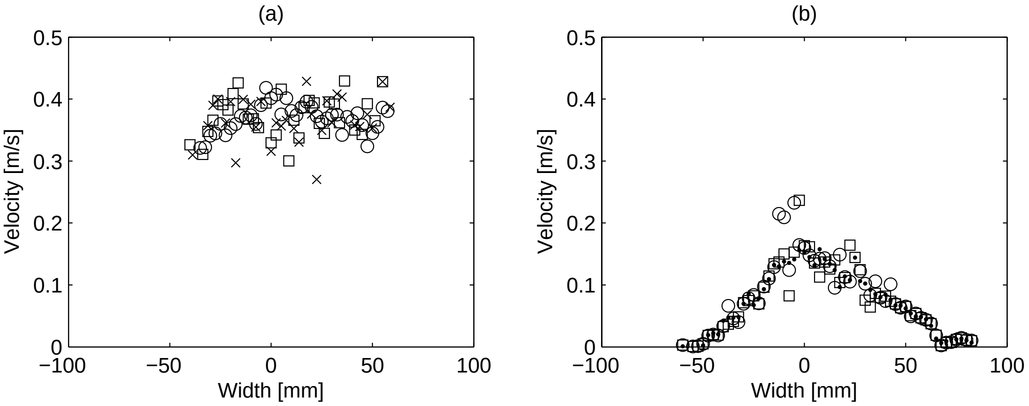

Fig. 2.5. Instantaneous velocity profiles for (a) bubble phase and (b) fluid phase for an air flow rate of 0.5 l/min: crosses are PTV data, open squares are image-masked data, filled dots are optic-filtered PIV data, and open circles are vector post-processed PIV data.

flow field. When a relatively low continuous phase velocity occurs, bubble vectors may not be large enough to be caught by the velocity threshold or median filtering. Likewise, when the continuous phase velocity is relatively high locally, the vectors may be incorrectly attributed to the bubble phase. In both cases, these vectors represent a rare and difficult to identify flow state. The consequence of these few velocity errors is studied in the error analysis presented below. It is important to note that by comparison between the fluid- and bubble-phase data, the post-processing algorithm does identify the majority of bubble-phase vectors correctly.

Fig. 2.6 shows an example of the phase separation algorithm applied to a complete vector map. Sub-plot(a) shows the recorded mixed phase image. This image is processed by regular PIV and filtered using the post-processing algorithm. The separated fluid phase velocity is shown in sub-plot(b) and the bubble velocity vectors are shown in sub-plot(c); sub-plot(d) shows the dispersed phase velocity vectors obtained from the PTV analysis. Similar results were presented in (Seol et al. 2007) using non-fluorescent tracer particles and a constant velocity threshold U_{max}. As seen

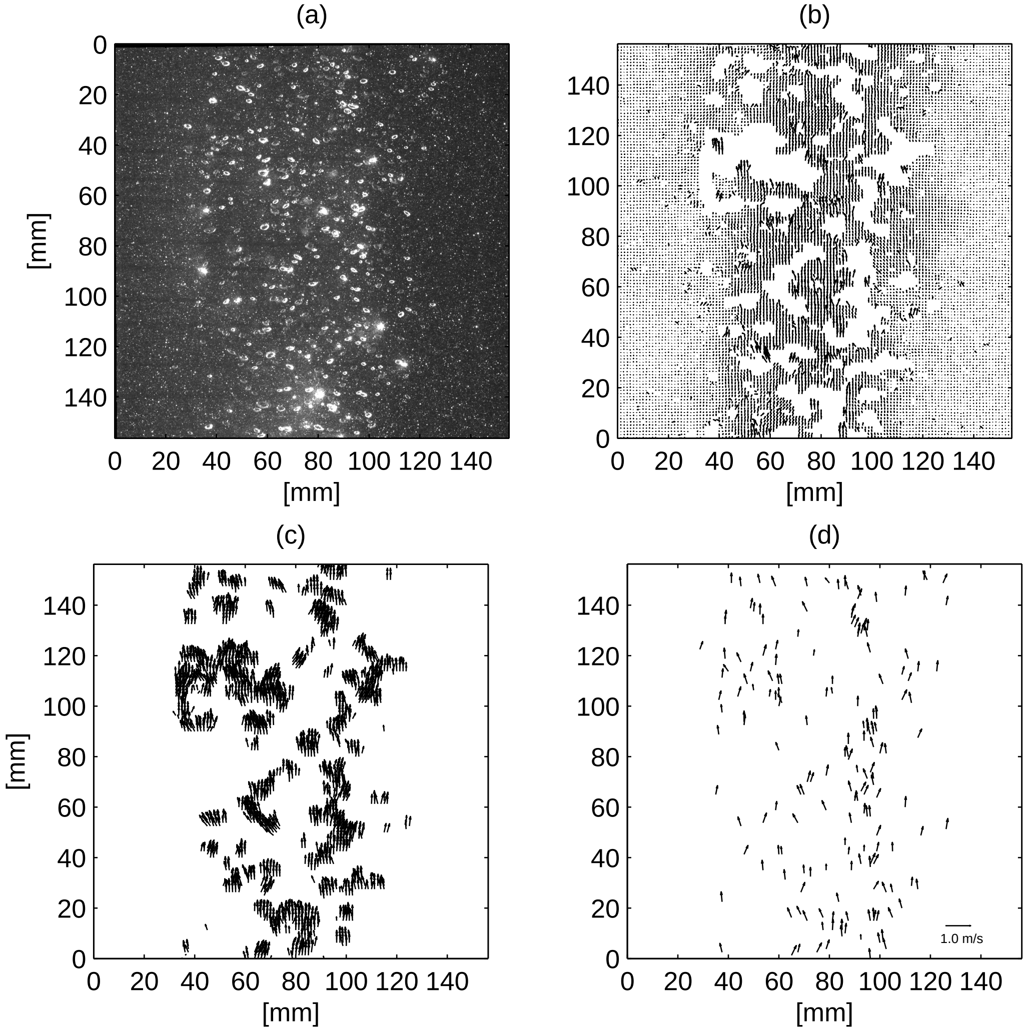

Fig. 2.6. Velocity vector filtering procedure: (a) raw image, (b) post-processed fluid-phase velocity map, (c) post-processed dispersed-phase vector map, and (d) PTV-processed dispersed-phase vector map.

in the figure, where bubble phase velocity vectors are removed, the continuous phase velocity map shows no data. By comparison to the camera image, these regions are relatively large due to the large size of the bubbles for this field of view, which was selected so that fine-scale details in the continuous phase could be studied (see the Section 2.6, below). The distribution and magnitude of the dispersed phase velocity vectors also agree with the vectors obtained by the PTV process. Because the phase separation algorithm is self contained, relying solely on data obtained from the mixed-phase images and not requiring fluorescent tracer particles, it can be applied at low cost using a single camera for many fields of view and without significant image processing.

2.5.2 Validation

To validate the proposed phase separation method, the vector post-processed velocity data are compared with the fluid-phase data from the optical separation method and with the fluid- and bubble-phase data from the image masked data. In some cases, the optically separated data obtain velocity vectors in regions where bubble velocity vectors have been removed by the phase separation algorithm. In the following discussion, error and correlation statistics are only presented for those regions where both data sets have velocity vectors.

Several error measures are used to quantify the effects of improperly categorized vectors in the post-processing algorithm on the measured instantaneous and time average properties of the plume. As a first measure, the mean velocity and standard deviation at each horizontal profile through the plume in the continuous phase data at each instantaneous vector map is investigated. These data can be interpreted in terms of the centerline velocity U_m and plume width b of a Gaussian profile through the plume. Fig. 2.7 illustrates scatter plots of U_m and b for each flow rate investigated;

symbols give the time average of these instantaneous quantities and error bars indicate plus and minus one standard deviation of the data over the experiment times series. We note that the error bars are presenting the variability in these bulk quantities due to turbulent fluctuations and not due to measurement errors; hence, good agreement should have similar horizontal and vertical error bars. The solid lines in the figure show the 45° perfect agreement line and the dash-dotted lines show a linear fit to the time average data along with 95% confidence intervals (dotted lines). Each dataset shows very good agreement with the perfect correlation line, as indicated by the fact that the 95% confidence intervals contain the perfect agreement line over the range of measured data with the only exceptions occurring for Fig. 2.7 (c) and (e). Comparison of the optically filtered data with the image masked data (Fig. 2.7 (c) and (d)), show the tightest agreement, which gives confidence to the image masking techniques and geometric correction used in the data analysis. For the post-processed data, agreement is achieved for the lower two gas flow rates, with deviations from the optically filtered and image masked results occurring for the highest gas flow rate (1.5 l/min). In all datasets, the error bars are also nearly symmetric, showing similar levels of turbulent fluctuations in each dataset. Based on these comparisons, the post-processing algorithm performs accurately for gas flow rates below 1.5 l/min for this field of view. This corresponds to a physical area void fraction of 1%, which for this field of view corresponds to 12% of the image area being occupied by bubbles. Thus, the method is limited to cases where <10% of the bubble plume area is occupied by bubbles in the PIV images.

To better understand the sources of error in the post-processed data, a small region of the instantaneous flow field for the fluid phase is shown in Fig. 2.8. This region was chosen to show the vector field around the largest error in this velocity map; all vectors shown in sub-plot (a) were identified as fluid-phase data by the phase

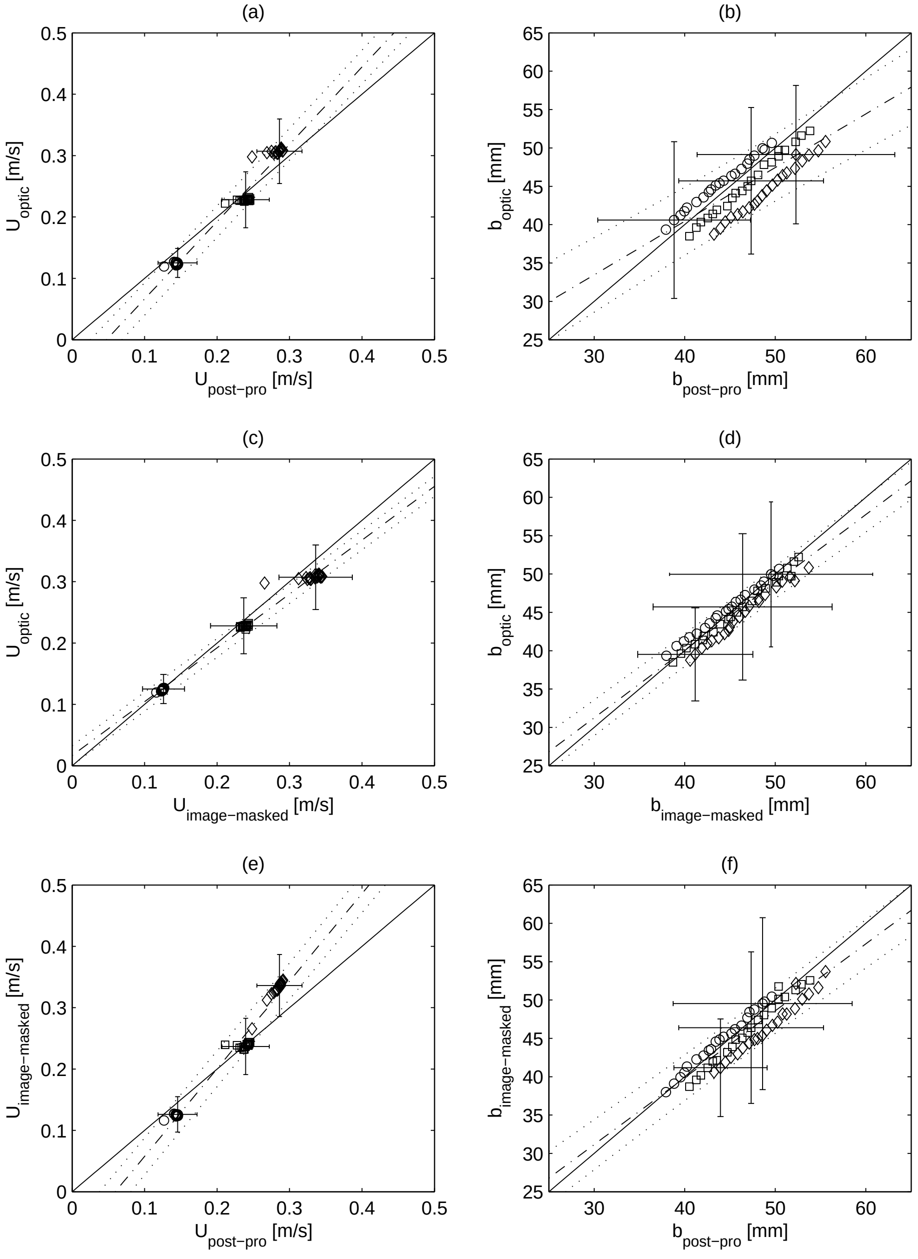

Fig. 2.7. Scatter plots of the fluid phase (a), (c), and (e) centerline velocity and (b), (d), and (f) plume width. Open circles are for 0.5 l/min, open squares are for 1.0 l/min, and open diamonds are for 1.5 l/min air flow rates. The solid lines give 45° perfect fit reference; dash-dot lines are linear fits to the time-averaged data, and the dotted lines show the 95% confidence intervals of the linear fit. Error bars show the standard deviation of the instantaneous data at one representative height for each gas flow rate used.

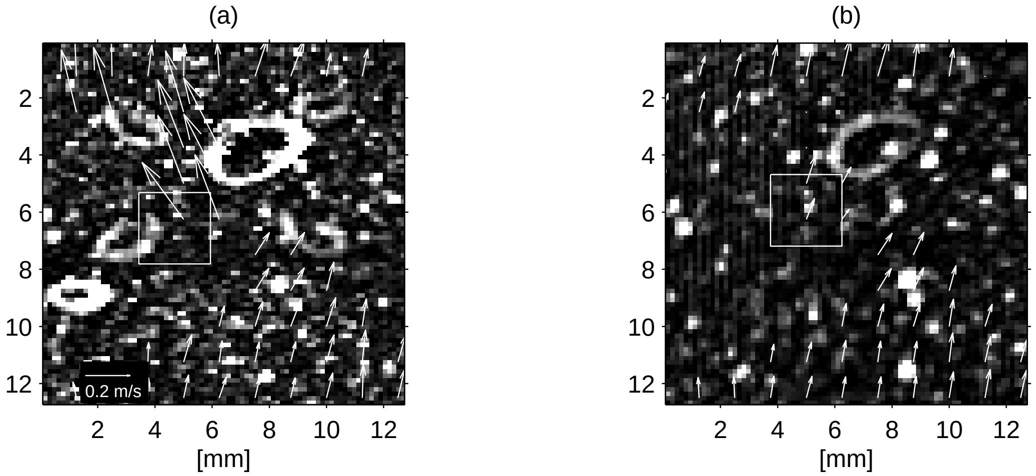

Fig. 2.8. Samples of fluid-phase velocity vector maps: (a) vector post-processed PIV, (b) optic-filtered PIV. Vectors are only displayed in (b) for points where vectors are present in (a) in order to aid in visual comparison of the data. The single vector surrounded by the white box is an error vector further investigated in Fig. 2.9.

separation algorithm. Also shown in each plot is the first image of the double frames used in the velocity calculation. From the comparison of these data sets, it is observed that the velocity data around the bubbles in the post-processed data are higher than nearby continuous phase vectors and sometimes show significant differences from the optically-filtered data. This is worst in the region identified by the white box in both sub-plots. Note also that the velocity vectors associated with bubbles in the lower left portion of this sub-region were correctly removed. Hence, in the regions immediately around a few bubbles, some vectors are identified as fluid-phase velocities by the post processing algorithm which are much greater in magnitude than corresponding vectors measured in the optically-filtered data.

To test whether the optically-filtered data may have errors in the wake regions behind bubbles, the cross-correlation field for one vector is investigated in Fig. 2.9. This vector is the one identified in the white box in Fig. 2.8. The cross-correlation

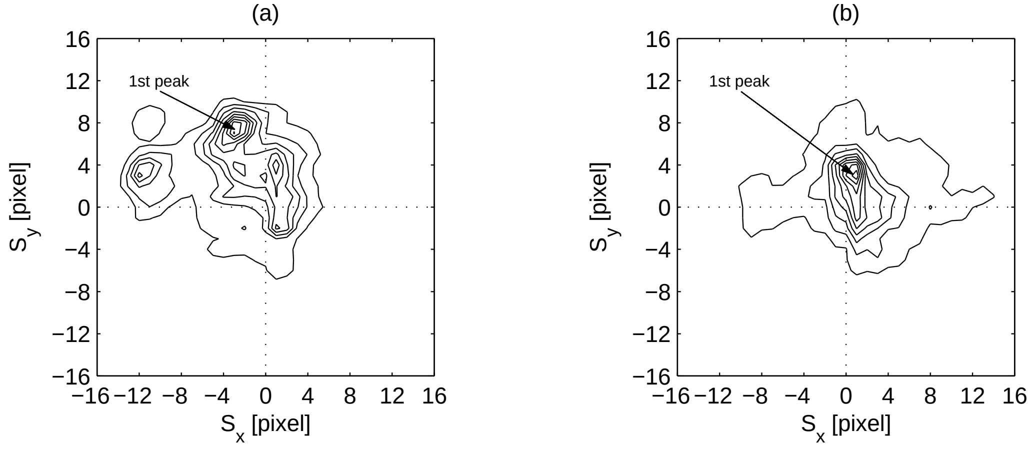

Fig. 2.9. Cross-correlation functions for the vector identified in Fig. 2.8 for (a) mixed-phase image and (b) optically-filtered image. The size of interrogation window is 16×16 pixels

field for the mixed-phase image (sub-plot (a)) clearly shows two distinct displacement peak and two secondary peaks. On the other hand, the cross-correlation field from the optically-filtered image (sub-plot (b)) has only one peak, and this peak is at the same position as one of the peaks in the mixed-phase image. From this, it can be inferred that the peak associated with the slower velocity is a real velocity associated with the fluorescent tracer particles, and that the higher-velocity peak in the mixed-phase image is associated with the movement of the bubbles. We also point out that using the secondary peak to obtain continuous phase velocity data is a common method in two-phase PIV. Because of the large size of the bubbles compared to the interrogation window size, errors may be introduced due to the large reflections from the bubbles. As seen in this correlations function, the bubble peaks are narrow and clearly identifiable, indicating a low velocity error. Furthermore, in the mixed-phase image, the higher velocities are clearly associated with bubble motion and are not real fluid velocity vectors in the bubble wakes. Thus, a few errors persist in the post-processed fluid-phase data.

To obtain information needed by integral models, the instantaneous flow fields were time-averaged to study the mean flow characteristics of the bubble plume. In the time average, the measured data were used with no attempt made to adjust the instantaneous plume centerline to account for plume wandering. As a result, the time average data will have slightly lower maximum velocities and wider plume widths than for data when wandering has been removed. This is a common artifact of time-average velocity data for laboratory experiments of bubble plumes (Seol et al. 2007). A typical profile of the time-averaged data is shown in Fig. 2.10. The bubble-phase data still show some noise, especially near the edge of the plume as identified earlier, and the data sets for the post-processed, image masked, and optically filtered data collapse to a consistent curve for the fluid-phase. The results of the ensemble cross-correlation method (Delnoij et al. 1999) using 15 images in each ensemble average and time averaging the 40 unique results are shown using the diamond symbols for comparison. These data have more scatter, likely due to the short measurement period, and give a good indication of the turbulence level in the plume. As witnessed by the close agreement of the post-processed data with the reference data sets, the errant velocity vectors in the post-processed data do not significantly affect the time average results when 150 s of data are taken. Thus, the post-processing algorithm is a reliable means to measure time-averaged quantities in multiphase flows.

For the global instantaneous and time-averaged flow fields of the continuous phase from the various methods the velocity errors were calculated and are depicted in Fig. 2.11. Calculated values for the three different air flow rates are plotted together to study the effect of bubble concentration. The left column of Fig. 2.11 (sub-plots (a), (c), and (d)) gives the instantaneous error based on Eq. (2.3) for one representative image, and the right column of Fig. 2.11 (sub-plots (b), (d), and (f)) shows the time average of these instantaneous results over all 600 vector maps. Comparing the vector

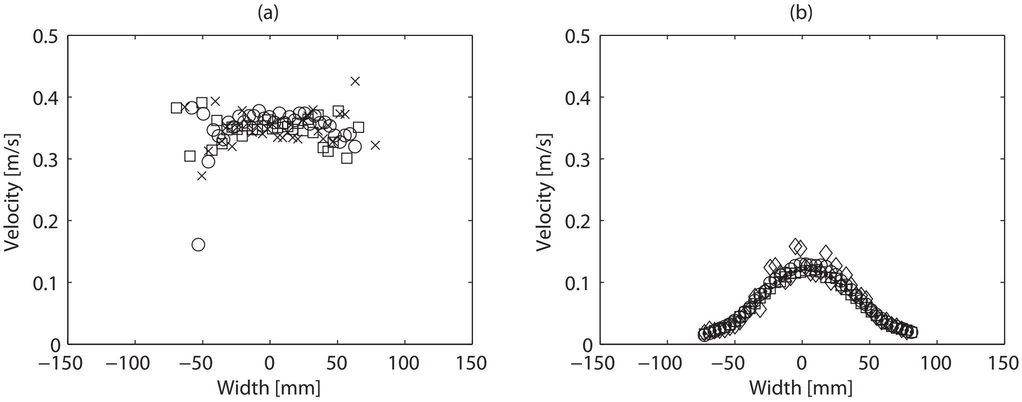

Fig. 2.10. Time-averaged velocity profiles for (a) bubble phase and (b) fluid phase. Crosses are PTV data, open squares are image-masked data, filled dots are optic-filtered data, open circles are vector post-processed PIV data, and open diamonds are ensemble correlation PIV data.

post-processed and image masked data (cross symbols), the errors tend to zero outside the plume in both the instantaneous and averaged results. Comparing either of these datasets to the optically filtered data indicate a base error level outside the plume of 4 to 10% in left column of Fig. 2.11 for one instantaneous image, but with errors tending to zero when averaged over all instantaneous results (right column of Fig. 2.11). This indicates that there are some differences between the optically filtered data and the other data sets, but that these differences are not likely due to camera registration or geometric correction of the images. We expect that the differences are due to image lighting characteristics, since the optically filtered data were slightly darker, and due to a few bubbles wandering outside the plume and into these lower-velocity regions. At the lowest flow rate, the image masked and post-processed data are nearly identical in the mean (sub-plot (b) with errors below 5%), with errors increasing to the order of 20 to 25% in the center of the plume for the higher gas flow rates (sub-plots (d) and (f)). We emphasize that these errors are for the instantaneous data; as seen in Fig. 2.11, errors are very low for the time average velocities. The high errors in Fig. 2.11 are also worst-case estimates because each misidentified bubble vector in the continuous phase data contributes a very large error to the overall error calculation in Eq. (2.3), which is only based on N =125 rows of velocity data for each data point in Fig. 2.11. We also note from the figure that the image masked data have similar errors to the post-processed data when each dataset is compared to the optically filtered data. Thus, there remains uncertainty in the continuous phase data, but the vector post-processing algorithm performs very well, especially at the lower flow rates.

One important consequence of the vector post-processing algorithm and the image masking method compared to the optically-filtered data is that many gaps appear in the velocity field around the bubbles that are not present in the optically-filtered data. Both the vector post-processing algorithm and the image masking methods have similar data coverage; Fig. 2.12 shows the data reduction rate δ

$$\delta(r) = \frac{n_v}{N} \tag{2.4}$$

where n_v is the number of continuous phase vectors identified in one row of data and N is the total number of possible vectors per row. In the center of the plume, δ approaches 20% at the low flow rates and exceeds 60% for the highest flow rate. These reduction rates can be adjusted by changing the field of view, but show the effect of image area void fraction on the data coverage for these experiments. When large fields of view are required that result in high image void fraction, optical phase separation is the only method of those presented here that will give high data coverage.

In summary, the post-processing algorithm works well for obtaining time-average data, but has some errant vectors near some of the bubbles in the instantaneous vector fields. As the flow rate of air increases, the method was shown to gradually break

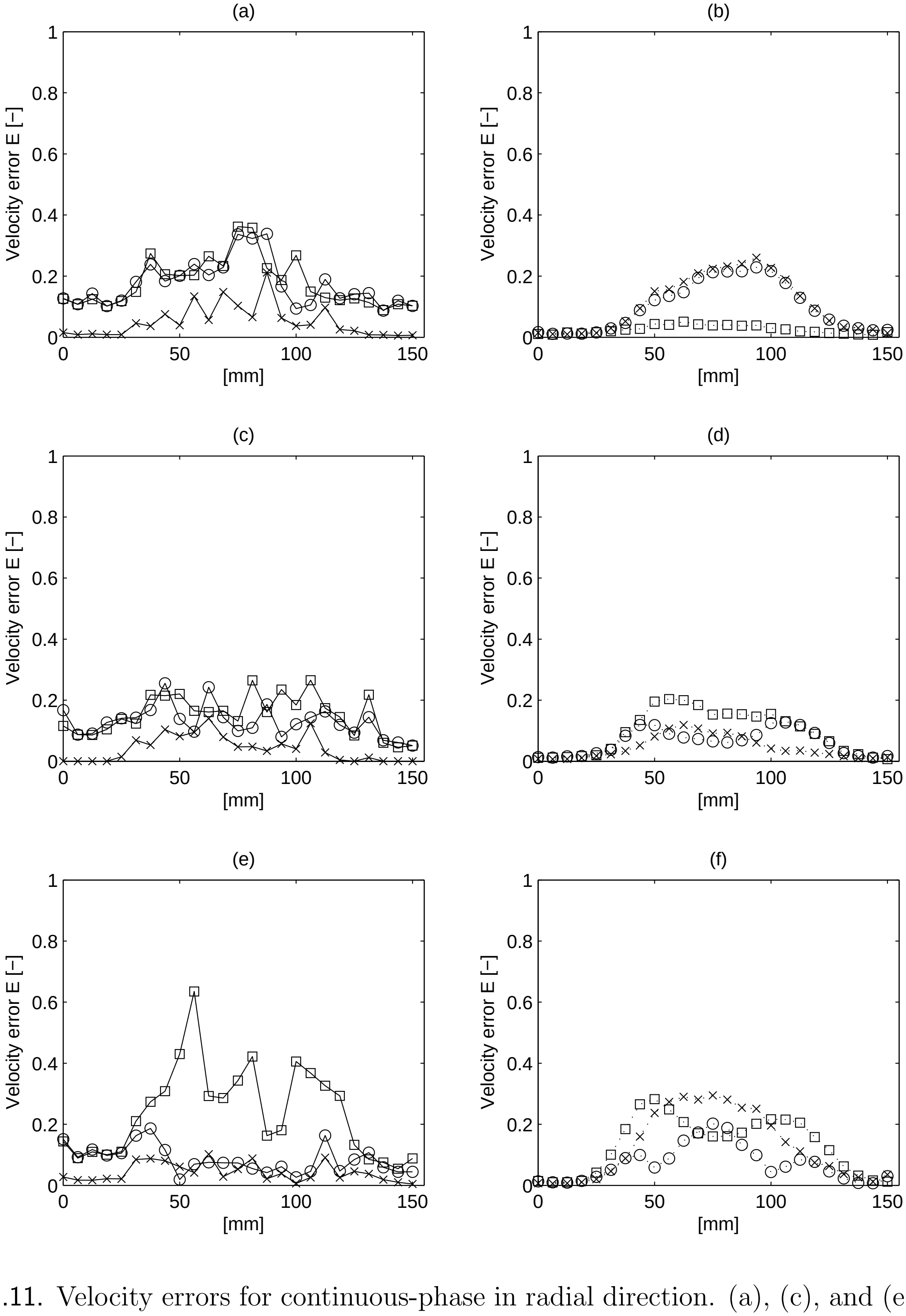

Fig. 2.11. Velocity errors for continuous-phase in radial direction. (a), (c), and (e) are for instantaneous data and (b), (d), and (f) are time-averaged data at 0.5, 1.0, and 1.5 l/min, respectively. Open circles compare vector post-processed and optically-filtered data, open squares compare image-masked and optically-filtered data, and crosses compare image-masked and vector post-processed data.

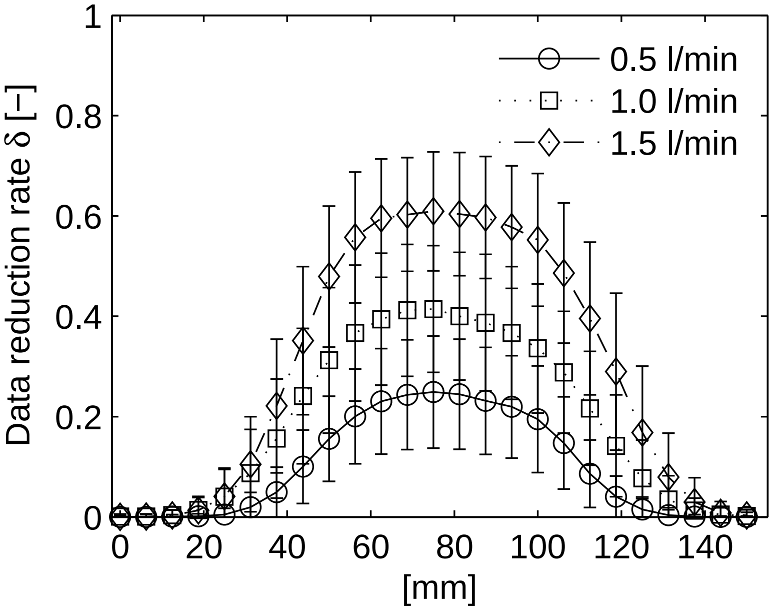

Fig. 2.12. Average data reduction rate as a function of the lateral coordinate and the gas flow rate. Error bars represent the standard deviation of data across all 600 vector maps in the time series.

down. For our experiments, a flow rate of 1.5 l/min had an image area void fraction of about 12% of the field of view within the plume, which appears to be the limit of this method for obtaining reliable continuous phase results. Many environmental and laboratory bubble-plume flows have similar low void fractions. For evaluating the velocity scales over which the method is applicable, the data analyzed here had a slip velocity of about 20 cm/s (net bubble velocity 40 cm/s) compared to an entrained fluid velocity of a similar magnitude (0 to 20 cm/s). The main effect of the different air flow rates tested was due to the void fraction and not the slip velocity. Moreover, these bubble slip velocities are typical of air bubbles over a wide range of bubble sizes; thus, for fluid and bubble-slip velocities of similar magnitude, the method is able to identify the majority of bubble phase vectors and remove them from the mixed-phase data. In addition, numerical models show that the entrained fluid velocity becomes nearly constant with height above the source, indicating that the method should be valid over a wide range of heights. Thus, for dilute laboratory- and field-scale bubble plumes using acceptable fields of view, this method is expected to apply.

2.6 Application

The vector post-processed data are applied in this section to study the instantaneous and mean-flow characteristics of an unbounded bubble plume in quiescent, unstratified ambient conditions. The instantaneous plume behavior is important to understand the physical interactions between the two phases and the mechanisms of entrainment.

Fig. 2.13 demonstrates the wandering behavior of the plume for a gas flow rate of 0.5 l/min. In the upper sub-plot (a), one cross-section of the plume is shown at a height of 430 mm above the diffuser, where the bubble column and entrained ambient fluid have significantly different centerline locations. The lower sub-plot (b) shows the locations of the bubble- and fluid-phase centerlines as a function of height. From sub-plot (a), it is clear that the entrained fluid velocity profile reacts on a different time-scale than the bubble column. This tendency for separation between the bubbles and entrained fluid has also been identified in cross flows (Socolofsky & Adams 2002) and for stratified ambient conditions (Socolofsky & Adams 2005). At this location the bubble column has moved out of the center of the tank into the ambient water, and the velocity profile of the entrained fluid has yet to react and follow the bubble column. The instantaneous snapshot of the centerline locations throughout the plume in sub-plot (b) shows similar behavior. Over much of the plume, the two phases (bubbles and entrained fluid) track each other, but occasionally the bubble column separates from the entrained fluid which is still accelerated upward along a different trajectory by its higher inertia.

An important property of bubble plumes is the entrainment of ambient fluid into the upward-rising continuous phase which is a result of capture of ambient fluid by eddies in the shear layer of the rising plume. Many means are available to identify eddy and coherent structures in turbulent flows, and we apply the swirl strength as suggested in Adrian et al. (2000). We calculate the swirl strength from the eigenvalues of the two-dimensional deformation tensor

$$D = \begin{bmatrix} \frac{\partial u}{\partial x} & \frac{\partial u}{\partial y} \\ \frac{\partial v}{\partial x} & \frac{\partial v}{\partial y} \end{bmatrix} \tag{2.5}$$

where u and v are the velocity components in the lateral (x) and vertical (y) directions. Because the velocity gradient operator has the effect of amplifying errors in the velocity field, we apply the least squares method over four velocity measurements to calculate the local velocity gradient as in Raffael et al. (1998). Local rotation is then identified when eigenvalues of Eq. (2.5) are complex, and the swirl strength is the imaginary part of the complex conjugate eigenvalue pair (Adrian et al. 2000). An eddy center is defined by a peak in the swirl strength, and the eddy extends out to a point where the swirl strength returns to zero. This method was applied to all three continuous phase velocity fields presented here to obtain probability distributions for eddy size in bubble plume core.

Fig. 2.14 shows the probability density function (PDF) for eddy size obtained from each PIV dataset for a gas flow rate of 0.5 l/min. The PDFs were calculated by classifying all eddies in each of the 600 vector maps. The PDFs from both the vector post-processed and image masked data are nearly identical, with very slight deviations at the largest eddy sizes, and the optically filtered data follow a slightly different trend. For the optically filtered data, relatively fewer small eddies and a

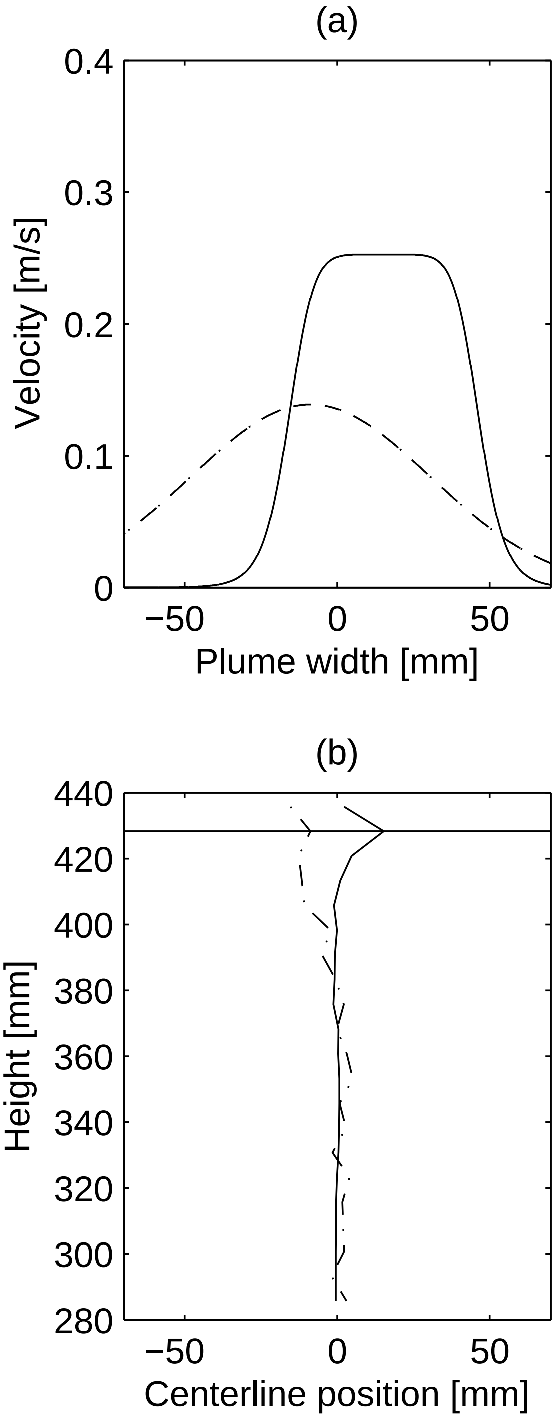

Fig. 2.13. Instantaneous comparison of the bubble and fluid phase centerline locations: (a) velocity profiles at one cross-section and (b) centerline location versus height. Solid lines are fitted to the vector post-processed bubble-phase data and dashed lines are fitted to the vector post-processed fluid-phase data.

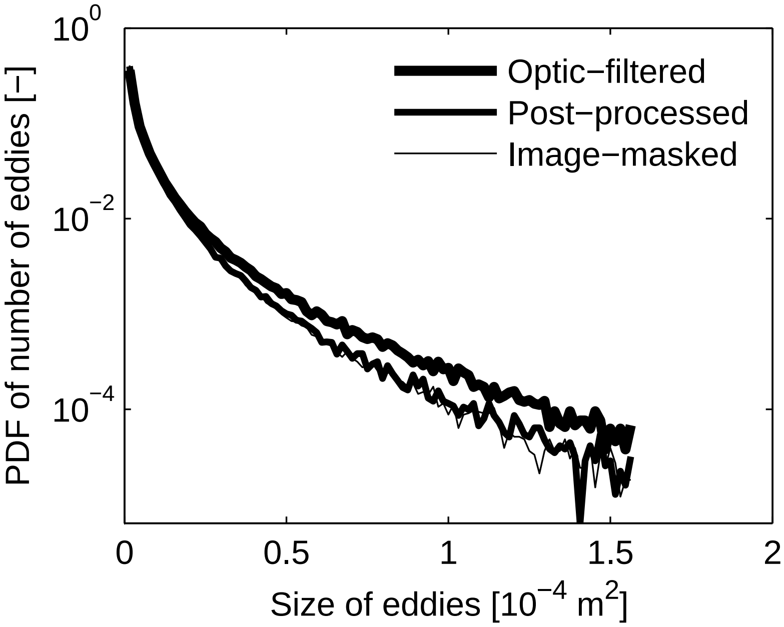

Fig. 2.14. Probability density functions of eddy size from the instantaneous continuous-phase data

larger number of large eddies (area greater than 0.5×10^{-4} m^2 or 8 mm equivalent diameter) are found compared to the vector post-processed or image masked data.

To understand this result, Fig. 2.15 presents the instantaneous result for one vector map using each velocity data set. Similarities are seen in the pattern of identified vortices between each plot. The main differences are in the number of identified eddies. The vector post-processed data has the fewest eddies, followed by the image masked and finally the optically filtered data. The image masked and vector post-processed data find fewer eddies due to the missing data that occur where the bubbles are present in the images. Based on the PDFs, even though the vector post-processed data identify fewer eddies, the identified eddies have the same statistical distribution as those identified in the image masked data. Both of these distributions are slightly different from the optically filtered data, which identifies a greater probability of large eddies. This is due to the fact that the image masked data do not have large gaps due

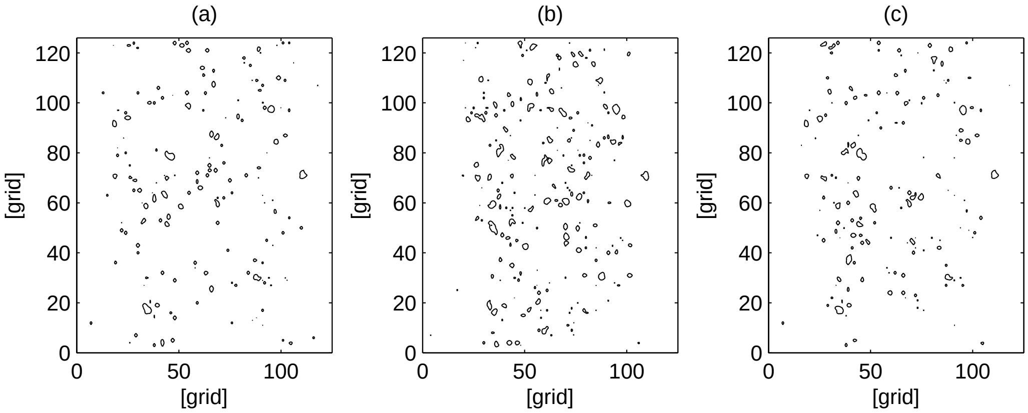

Fig. 2.15. Swirling strength instantaneous continuous-phase data. (a) Vector post-processed data, (b) optic-filtered data, and (c) image-masked data. The contour line are for swirl strength of 5 [1/sec].

to the bubbles and are more likely, therefore, to be able to capture the signatures of the largest eddies in the flow field. Nonetheless, the few misidentified velocity vectors in the vector post-processed data appear to have no effect on the identification of eddies; thus, the vector post-processing algorithm can also be applied to study the smaller scale (order of the spacing between bubbles) coherent structures in bubble plumes.

2.7 Conclusions

In this paper we evaluate the applicability of a vector post-processing algorithm for phase separation introduced by (Seol et al. 2007) to study the behavior of unconfined bubble plumes. To verify the phase separation method, synoptic mixed-phase and optically-separated data were collected using fluorescent tracer particles to track the continuous phase. The data are evaluated to yield a mixed-phase data set for testing and two reference data sets: the optically-separated fluid-phase data and fluid- and bubble-phase data obtained using digital masking techniques. From the error analysis among the data sets, the vector post-processing algorithm performs well, but contains small errors in the fluid-phase velocity field around some bubbles. The errors do not impact the evaluation of instantaneous velocity profiles through the plume or eddy size distributions based on swirl strength, and time-average velocity fields are also well-represented by the post-processed data. From this study, the following conclusions can be summarized:

1. The biggest errors for the fluid phase in the vector post-processed data compared to the optically-filtered or digitally-masked data were observed around some of the bubbles. These vectors were identified to be errant bubble velocity vectors that were not properly identified by the phase separation algorithm. Though a few of these false vectors are inevitable, the majority of bubble phase vectors were accurately identified. Moreover, instantaneous velocity profiles obtained from the vector post-processed data compare well with profiles from the reference data sets, with velocity field errors below 10 to 15% for most regions of the plume at the void fractions studied (10% of the field of view or less).

2. The analysis of the velocity errors and cross-correlation coefficients between the post-processed and reference data sets shows that the post-processing algorithm is sensitive to the bubble void fraction and that time-averaged results are accurate despite the few errant bubble vectors identified above. For area void fractions below 1% of the field of view, the method works sufficiently to study the entrainment properties and instantaneous plume wandering behavior of bubble plumes.

3. For the post-processing method to adequately identify bubbles, a significant bubble slip velocity is required. In the experiments presented here, the slip velocity and entrained fluid velocity were of similar orders of magnitude. This case

was also shown to be typical of environmental applications of bubble plumes; hence, the method is expected to perform well over a wide range of dilute laboratory and field-scale plumes.

4. Analysis of the bubble plume wandering illustrates the common behavior of separation occurring between the dispersed and continuous phases. Because the bubbles are not dissolved in the water, there is no requirement that the entrained fluid follow the bubble column as it wanders. Indeed, the much greater inertia for the entrained fluid causes the continuous fluid velocity to respond on a longer time scale than the bubble column. As a result, at several levels in the plume, the centerline tracks for the bubble column and entrained fluid are observed to diverge. This phenomenon has implications for integral plume or time-average modeling, where the two tracks are assumed to follow each other. Moreover, despite recent studies of plume wandering, the exact cause and effect mechanism for bubble core wandering is unknown. This phase separation method coupled with multiple, detailed fields of view over a wide spatial range of the plume may be helpful in elucidating the mechanisms controlling this behavior.

5. Analysis of the swirl strength indicates that both the vector post-processed and image masked data provide identical probability density functions of the eddy size, with a greater probability of larger eddies identified from the optically filtered data. This is due to the presence of gaps in the velocity field data in the vector post-processed and image masked data; hence, these data only provide reliable size distributions for eddies with diameters on the order of the spacing between bubbles. All eddy PDFs show a smooth size distribution resembling an exponential distribution.

CHAPTER III

PARTICLE IMAGE VELOCIMETRY MEASUREMENTS OF THE MEAN FLOW CHARACTERISTICS IN A BUBBLE PLUME[1]

3.1 Introduction

Multiphase flows occur in a wide range of engineered and natural systems. In contrast to many chemical and environmental engineering applications, where the multiphase flow fills the domain of interest (e.g. bubble columns, chemical reactors), many environmental applications involve unbounded plumes issuing from nearly point-source conditions. These applications include bubble plumes for reservoir aeration or destratification (e.g. McDougall 1978, Wüest et al. 1992, Asaeda & Imberger 1993, Lemckert & Imberger 1993), oil and natural gas plumes for assessing the fate of oil released from accidental undersea oil-well blowouts (e.g. Yapa et al. 1999, Socolofsky & Adams 2002, Socolofsky & Adams 2003), and the direct injection of liquid CO_2 in the deep ocean as a means to mitigate atmospheric build-up of greenhouse gases (e.g. Caulfield et al. 1997, Socolofsky et al. 2002, Socolofsky & Adams 2005). These later cases are commonly approximated as self-similar, axially-symmetric plumes, and integral plume models of various complexity have been applied to evaluate their behavior (e.g. McDougall 1978, Wüest et al. 1992, Asaeda & Imberger 1993). While several important characteristics of the axially symmetric two-phase flow have been measured, such as entrained fluid volume flux and plume width, it remains to mea-

---

[1] Reprinted with permission from "Particle image velocimetry measurements of the mean flow characteristics in a bubble plume." by Seol et al. (2007). *Journal of Engineering Mechanics*, Vol. 133, No. 6, pp. 665-676, Copyright[2007] by American Society of Civil Engineers.

sure detailed, full-field velocity for the unbounded case. Thus, we present laboratory experiments using non-intrusive measurement technology that capture instantaneous and time-averaged full-field velocity information for the continuous and dispersed phases of an unbounded bubble plume in quiescent, unstratified ambient conditions. These measurements are important to quantify the entrainment coefficient needed by integral models and to evaluate the interactions between the dispersed phase and the entrained ambient fluid.

Common image velocimetry methods, such as particle image velocimetry (PIV) and particle tracking velocimetry (PTV), have been developed and applied by other researchers to understand the flow characteristics and mixing properties of various two-phase flows (Gui & Merzkirch 1996, Gui et al. 1997, Delnoij et al. 1999, Brücker 2000, Deen 2001, Lindken & Merzkirch 2002). The major advantage of these image velocimetry methods is their ability to capture instantaneous velocity field information non-invasively. Both PIV and PTV employ similar data processing techniques, which include double-exposed or double-frame images of tracer particles illuminated by successively pulsed laser sheets and calculate the velocity by dividing the displacement of seeded particles with the time interval between laser pulses (Oakley et al. 1997). The difficulty in multiphase flows lies in the fact that the bubble phase and liquid phase exist together in the flow.

Thus, the challenge in applying PIV or PTV to multiphase flows is in separating the tracer particles tracking the entrained continuous phase from the dispersed phase particles, droplets, or bubbles. Previous methods to separate the gaseous and liquid phases to apply PIV or PTV can be summarized according to which stage in the analysis the phase separation has been made. First, at the image capture stage, two separate images can be generated for bubbles and fluorescent tracer particles using optical separation methods with two cameras and an optical filter (Sridhar et al.

1991, Hilgers et al. 1995, Deen 2001). PIV and PTV methods can be applied to the separated bubble and fluorescent particles images to obtain phase-separated velocity fields. Second, a single image can be captured for both phases simultaneously and then image processing techniques can be used to identify the bubble signature and separate the phases before applying PIV or PTV (Gui & Merzkirch 1996, Gui et al. 1997, Delnoij et al. 1999, Brücker 2000, Grota & Strauß 2000, Kiger & Pan 2000, Deen et al. 2002*b*). Gui & Merzkirch (1996) and Gui et al. (1997) used the size difference between bubbles and tracer particles, and Sakakibara et al. (1996) made use of gray-scale intensity differences to discriminate the two phases. Other methods include applying a median filter (Kiger & Pan 2000), edge detection algorithms (Brücker 2000), or digital masking techniques (Lindken et al. 1999, Gui & Merzkirch 1996, Grota & Strauß 2000). In each case, the bubbles and continuous phase tracer particles are separated into two images before PIV or PTV analysis. Third, the bubble signature can be removed during the PIV or PTV analysis using ensemble correlation methods based on the slip velocity (Delnoij et al. 1999, Deen et al. 2002*b*). The bubble phase and fluid phase have different correlation peaks in the correlation field, so that they can be separated based on their velocity, the higher velocities being attributed to the bubbles. Among these techniques, the optical phase separation method is preferred; however, it requires the use of two cameras per interrogation window and expensive fluorescent tracer particles. The single-image phase separation methods are also successful, but require computationally expensive image processing methods or customized PIV and PTV algorithms.

In contrast to these methods, we propose a simple, inexpensive method for phase separation that uses standard tools available in most PIV software. The primary difference in our method is that the phase discrimination is made after processing the mixed-fluid PIV images; whereas, previous methods remove the bubbles before PIV processing. In our method, single, mixed-fluid images are captured using one camera. A pixel intensity threshold is used to obtain images of the bubbles only. PTV is applied to these images, yielding the bubble velocity information. Regular PIV is then applied to the unprocessed mixed-fluid images. The velocity field obtained from PIV, therefore, contains vectors for both the bubbles and the entrained fluid. The bubble vectors are subsequently removed using a velocity threshold and median filter technique. The parameters of the median filter are calibrated so that the extracted PIV bubble vectors match the results of the PTV analysis. The remaining vectors constitute the entrained fluid velocity field. In this way, phase separated results are obtained using standard PIV and PTV software. These results are then used to study the behavior of the two-phase plume.

The main goal of this study is to apply simple PIV and PTV analysis to an unbounded bubble plume to obtain the mean-flow characteristics of the plume. The section 3.2 describes the experimental set-up and details the procedures for our phase separation algorithm. The section 3.3 first presents the mean flow characteristics of the bubble and fluid phases obtained from the laboratory measurements and then compares our results for the entrainment coefficient to those of other researchers. From these data, the entrainment coefficient in two-phase plumes is shown to depend on a dimensionless slip velocity.

3.2 Methods

The experiments were conducted in the Hydromechanics Laboratory of the Ocean Engineering Program at Texas A&M University. Fig. 3.1 shows the set up for the experiments. A Plexiglas tank with dimension of 38×38×80 cm was used in the experiments. The air was injected from an aquarium air diffuser with stone diameter

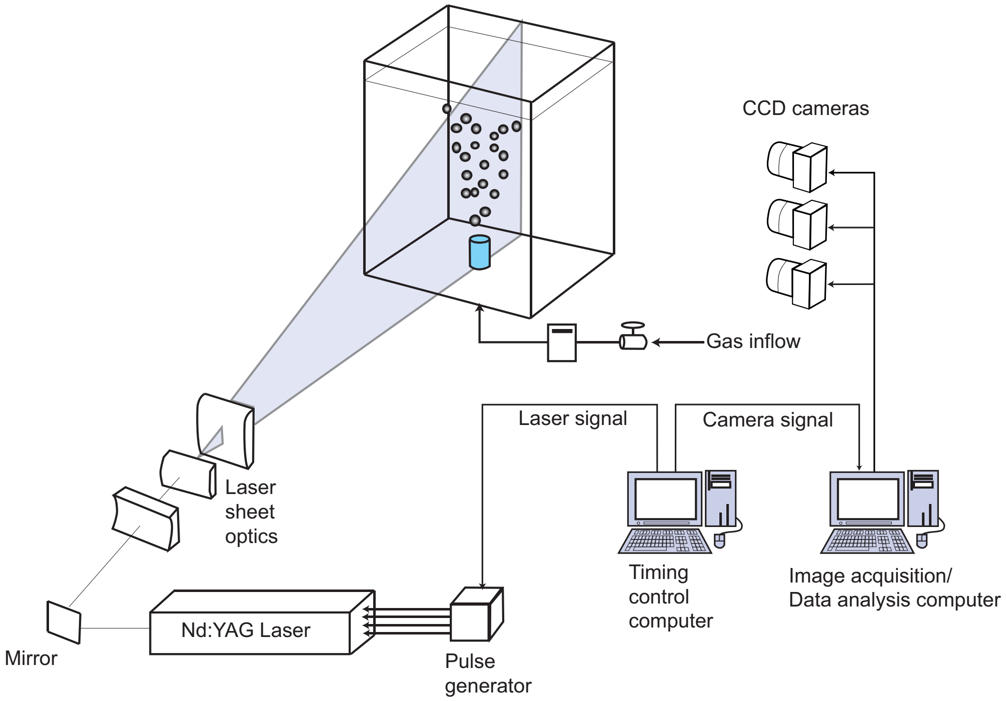

Fig. 3.1. Laboratory experimental setup for the PIV and PTV methods.

of 1.4 cm, which was fixed to the tank bottom. The characteristic diameter of bubbles generated from the airstone diffuser was 1.5 to 2.0 mm. A needle valve and gas mass flow meter (Alborg GFM 171) enabled precise control of the air flow rate from the air source. The air flow rates in the experiments were 0.5, 1.0, and 1.5 l/min at standard temperature and pressure (STP).

The setup for the experiments was typical of a PIV study. An Nd:YAG double-pulsed laser (wave length 532 nm, 320 mJ/pulse) was used to generate a light sheet using a spherical lens. The light sheet thickness was adjusted to 3 mm in order to increase the possibility of capturing wobbling bubbles. Due to availability, two different kinds of CCD cameras, a FlowMaster 3S camera (12-bit intensity depth with 1280×1024 resolution) and two Basler cameras (10-bit intensity depth with 1004×1004 resolution) were used. The cameras were positioned at different heights to take images of the whole plume from a height of 8 cm above the diffuser (the beginning of the zone of established flow) to a maximum height of 60 cm above the diffuser. The fields of view of each camera were 21×18 cm for the FlowMaster 3S camera at the bottom and 18×18 cm for the two Basler cameras at the middle and top of the plume, each field of view having 1 cm of overlap. In order to synchronize the cameras and laser, a careful timing control scheme was adopted. The three cameras and the pulse generator that controlled the laser (500A by Berkeley Nucleonics Corporation) were triggered using LabVIEW and a National Instruments PCI-6713 analog signal output board (12-bit × 8 channels).

Velocity fields are obtained for the entrained fluid and bubbles from a single set of images. As the bubbles released from the airstone diffuser rise with a velocity of approximately 40 cm/s (Socolofsky 2001), the time interval between image pairs was chosen as 4 ms, in which the average bubble displacement was around 10 pixels. Non-fluorescent tracer particles were added to the water to track the entrained fluid; the particles were white polyamide spheres with a characteristics diameter of 50 μm. Due to their different diameter and light scattering characteristics, the bubbles and the seeding tracer particles have different gray-scale values in the captured images. Specifically, the gray-scale intensities of the seeding tracer particles ranged from 1000 to 2000 in the high-resolution camera and from 200 to 400 in the low-resolution cameras; whereas, the gray-scale intensity of the bubbles was controlled to have nearly saturation intensity in both cameras (4095 in the high-resolution camera and 1024 in the low-resolution cameras). The lower light intensity of the seeding tracer particles is equivalent to using a camera with lower bit depth (Raffael et al. 1998). Because we are using 10 and 12 bit cameras, the particles were always imaged with a greater than 8 bit intensity depth so that the error in the particle displacement predicted by PIV is between 0.1 and 0.3 pixels, which is very near the limit of the resolution of the

PIV method at higher bit depth. As a result, we do not expect a significant difference in the uncertainty for velocity vectors obtained for the bubbles or the entrained fluid from the mixed-fluid images.

Although most of the bubble signature is bright, shadow effects cause some regions of the bubble signature to be rather dark. As a result, it was not possible to completely remove the bubble signature from the mixed fluid images purely on account of their gray-scale intensity. As discussed in the introduction, several images processing methods have been described in the literature to remove the bubble signature from the images before PIV or PTV processing. In the following, we describe an alternate phase separation method which is applied after the PIV and PTV processing.

3.2.1 Phase Separation Method

Because images are obtained that contain both the bubbles and the entrained fluid tracer particles, a data analysis method is required to obtain phase-separated results.

The bubble velocity field is obtained using the standard PTV method applied to an image containing only the bubble signature. The bubble-only image is obtained by selecting pixels from the mixed fluid image that lie above a threshold intensity value. Since there is nonuniformity in the laser intensity from top to bottom and since the opposite side of a bubble plume from the side the laser light enters is darker, some bubbles in the raw image have lower gray-scale intensity than the saturation intensity. Therefore, the threshold values are carefully chosen to ensure that most of the bubbles are extracted. The gray-scale values of 3000 for the high resolution camera and 500 for the low resolution camera were chosen as thresholds. Fig. 3.2 shows an example portion of the mixed fluid image (a) and the separated bubble image (b) after applying the threshold value. After thresholding, the true bubble velocities are obtained by

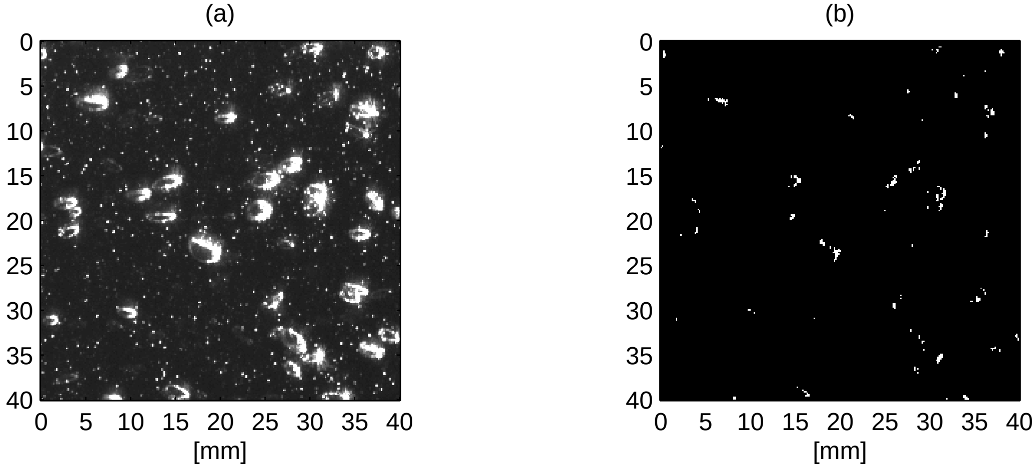

Fig. 3.2. PTV image processing: (a) raw image of the mixed fluid phases and (b) image containing bubbles only, obtained by applying a threshold filter to image (a).

applying PTV to the extracted bubble images.

The velocity field for the entrained fluid is obtained by post-processing of the mixed fluid PIV results. The PIV method detects the displacement of a particle in a divided small interrogation window. First, the standard PIV method is applied to the mixed fluid images with the interrogation areas chosen as 32×32 pixels at the first pass and 16×16 pixels at the second pass with an overlap of 50%. To obtain the entrained fluid velocity vector field, the unwanted bubble vectors were removed in a first, rough pass by specifying an allowable velocity range for the entrained fluid and in a second, final pass by applying the vector median filter to remove the remaining bubble vectors. In this study, the allowable maximum vertical velocity of the entrained fluid was set to 30 cm/s and the maximum horizontal velocity to 20 cm/s. The remaining bubble vectors were then filtered out using the vector median filter. The median filter is a nonlinear filter to remove outlier vectors (Westerweel 1994). The median filter sorts a specified number of neighboring vectors into ascending order and finds the median

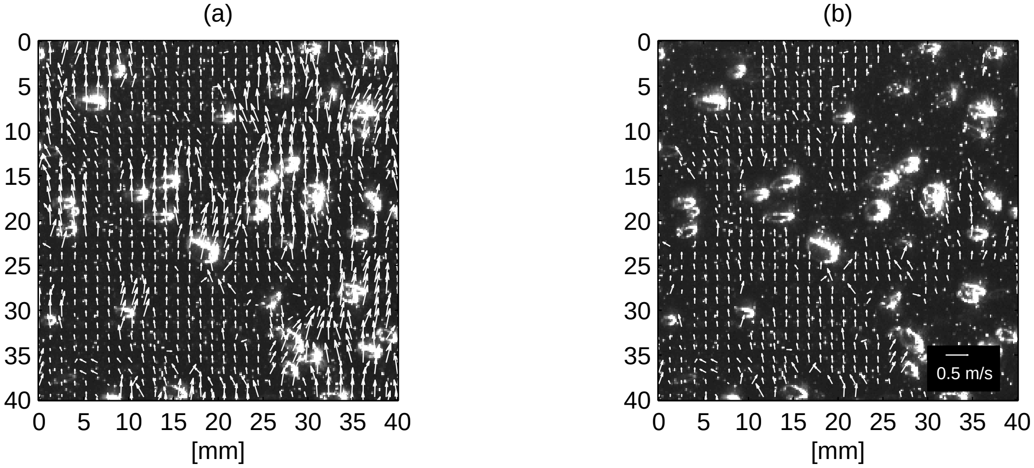

Fig. 3.3. Raw velocity vector map (a) and median filtered velocity vector map (b).

value of the velocities. Then, it determines the range of allowable vectors as follows:

$$U_{med} - fU_{rms} \leq U \leq U_{med} + fU_{rms} \tag{3.1}$$

where U denotes the allowed vector components in the x- and y-direction, and U_{med} and U_{rms} denote the median vector and standard deviation of all neighboring vectors, respectively (LaVision GmbH 2002). The parameter f for the median filter is specified to adjust the allowable vector range. The parameter f and the number of neighboring vectors taken into account are specified by careful visual examination of the raw image and velocity vector field. A sample median filtered vector map is shown in Fig. 3.3. The parameter values for the median filter were determined by examining the overlapped vector map with the raw image and selecting their values to remove all the bubble velocity vectors from the raw vector map. The results of this phase separation are verified by comparing the extracted vectors to the PTV analysis results. This is presented later in the Results and Discussion section.

Fig. 3.4 shows the complete procedure to obtain phase-separated vector maps from a raw image. Fig. 3.4(a) shows the raw image from the experiments. After applying PIV to this raw image, the fluid-phase velocity vector map (b) and the bubble-phase velocity vector map (c) can be separated using a velocity threshold and median filter as mentioned above. The bubble velocity vector map from the PTV analysis (d) is shown for comparison.

3.2.2 Limitations

We first point out that our phase discrimination method is not intended to be better than the optical phase separation methods using fluorescent particles and multiple cameras or image processing techniques that remove the bubble signature before PIV processing. Instead, we are proposing a simpler method that works adequately for the measurements we seek, which are of the mean flow field in dilute bubble plumes.

The phase-discrimination method proposed here has some limitations. First, the dispersed phase must have large bubbles or droplets compared to the size of the entrained fluid PIV tracer particles. This is required for two reasons: (1) the correlation peak for the bubble signature in an individual interrogation window must be much greater than that for the tracer particles and (2) there must be a significant slip velocity between the dispersed and continuous phase for the median filter to accurately identify bubble velocities.

Fig. 3.5 shows a sample PIV interrogation window in our experiments. For air, bubble sizes above 2 mm satisfy the requirements of our method given our experimental set-up. Second, the bubble concentration must be low enough that a significant number of entrained fluid vectors are obtained within the bubble plume core, otherwise, no information on the entrained fluid will be collected. In our set up, the bubble flow rate of 1.5 l/min had a void fraction of 3% near the bottom of the plume which was near the limit of the applicability of our method. For higher void fraction, a smaller field of view and greater magnification would have been required. Third,

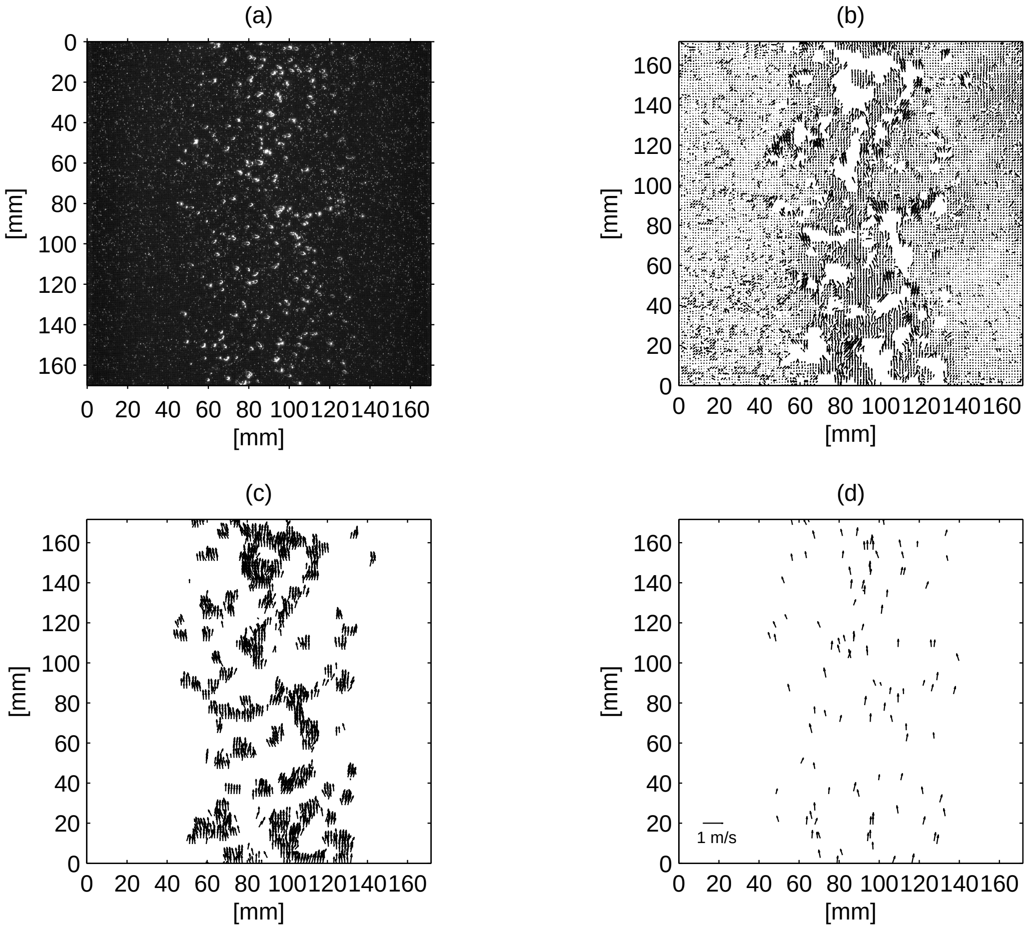

Fig. 3.4. Example of the phase separation method and the results of the PIV and PTV analysis: (a) raw image, (b) vector post-processed fluid-phase velocity map, (c) vector post-processed dispersed-phase vector map, and (d) PTV-processed dispersed-phase vector map.

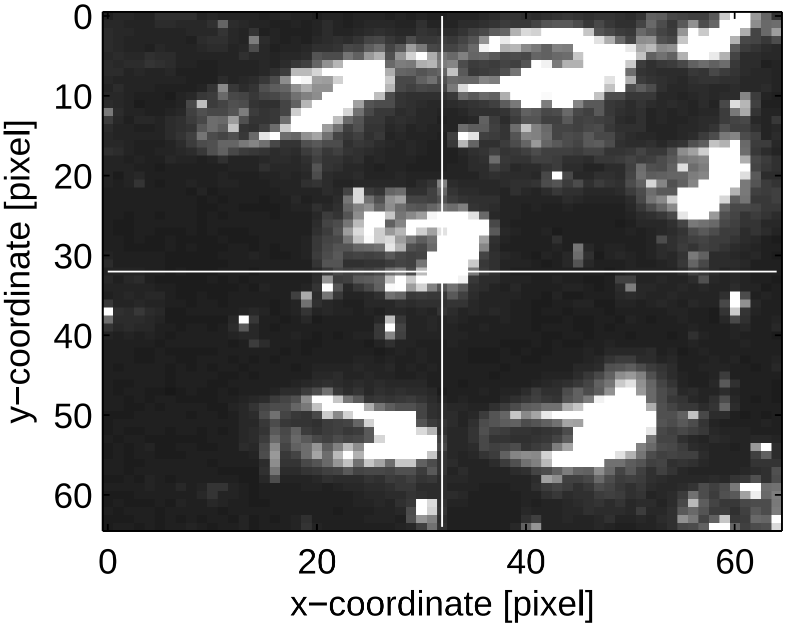

Fig. 3.5. Sample view of four 32×32-pixel interrogation windows showing the relative size of bubbles and entrained fluid tracer particles.

because continuous phase velocity vectors immediately behind the bubbles are similar to the velocity of the bubbles, our method treats them as a bubble velocity vector. As a result, the entrained fluid velocity has some bias toward lower than actual velocity. This error is unavoidable in this method. However, environmental applications deal with dilute plumes where the void fraction is well below 5%. Thus, the great majority of fluid is not traveling in the immediate wake of the bubbles and the results of our method should be adequate to capture the mean flow characteristics in dilute bubble plumes.

3.2.3 Data Analysis

To obtain mean velocity profiles for the dispersed and continuous phases, the instantaneous velocity data were processed to remove the plume wandering effect and then time averaged. Plume wandering is the tendency for the plume centerline to meander slowly during an experiment, which can be significant in a closed, unstratified tank. To remove the plume wandering effect in the data, we had to identify the instantaneous plume centerline and then shift the data so that the centerline was moved to the middle of the tank. Because of the patchiness of the phase-separated data, a spatial average was applied to obtain the instantaneous velocity averaged over ten rows of PIV vectors (about 2 cm vertical extent of the plume). A Gaussian profile was then fit to the filtered data and the center of the Gaussian profile was taken as the instantaneous plume centerline. The raw velocity data were finally shifted so that the plume wandering was removed. In shifting the data, plume wandering was not severe enough that the plume interacted with the walls of the tank. After the instantaneous data were shifted, time-average velocity fields were obtained by averaging 600 double frames of velocity data (150 seconds).

From the time-averaged velocity fields, the velocity profiles for the bubble phase and fluid phase can be found. From the data, the fluid velocity profile follows a Gaussian distribution described by

$$U(z,r) = U_m(z)\exp\left(-\left(r/b\right)^2\right) \tag{3.2}$$

where b is the plume width, and $U_m(z)$ is the centerline velocity of the fluid phase velocity profile; z and r denote the vertical and horizontal direction coordinates, respectively. The parameters of the Gaussian curve, b and U_m, are determined by non-linear least-squares regression applied to the time-averaged velocity field information. These centerline values along the plume height provide the fluid volume flux and momentum flux. Moreover, the bubble velocity profiles more closely resemble a top-hat profile, and the curve fitted to the data is the reverse of a shallow water wake profile suggested by Monkewitz (1988), given by

$$U(z,r) = \frac{U_b(z)}{1 + \sinh^{2\beta}(r/b_b)} \tag{3.3}$$

where $U_b(z)$ and b_b are the maximum value and width of the bubble velocity profile. These values are also determined from non-linear least-squares regression in the same manner as for the fluid phase. β is a parameter that adjusts the flatness of the central part of the profile. Taking $\beta = 1$ gives a profile very similar to the Gaussian profile. In this study, $\beta = 3$ was chosen as the best match to the measured data.

3.3 Results and Discussion

Experiments were performed for bubble flow rates of 0.5, 1.0, and 1.5 l/min at STP. The results of these experiments are discussed in the following.

3.3.1 Velocity Profiles and Verification of Phase Separation Method

To verify the phase separation method used to remove the bubble velocity vectors from the mixed fluid PIV results, the PIV data are compared to the PTV data for the bubble velocity. Fig. 3.6(a) and (b) show the time-averaged velocity profiles for the bubble phase at different heights. The bubble velocity data were fitted to the Monkewitz curve (Eq. (3.3)) as suggested in the previous section. The profiles of the rise velocity resemble a top-hat profile with a maximum velocity around 40 cm/s and zero over the outside of the plume.

In Fig. 3.6(a) and (b) the data from the PTV analysis ($\times$) are plotted together with the bubble data removed from the PIV results using the median filter ($\circ$). The fitted value of f for the median filter varied between 1 to 1.5 to obtain the best fit. The number of neighboring vectors for the median filtering was 4. From the figure, it

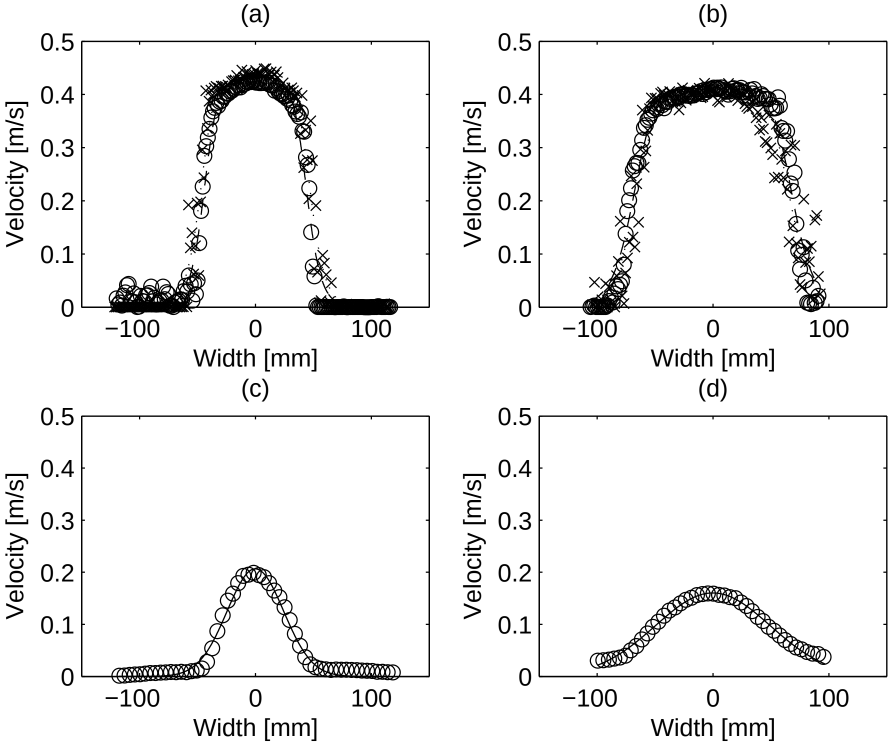

Fig. 3.6. Velocity profiles for the bubble phase (a and b) and the entrained fluid phase (c and d). Symbols denote measured data from the PIV (○) and PTV (×) analysis and lines present the fitted Monkewitz (a and b) and Gaussian (c and d) curves.

is confirmed that the extracted bubble velocity data from the PIV are in agreement with the bubble velocity data from the PTV. We also conclude that the remaining continuous phase vectors in the PIV data do not include the bubble signature.

Fig. 3.6(c) and (d) illustrates the average velocity profile of the fluid phase at two heights for the flowrate of 0.5 l/min. The Gaussian curve fit to the entrained fluid shows good agreement with the measured data. According to these profiles, water is carried upward with a maximum velocity of 20 cm/s near the center of the profile. The fluid phase velocity profiles also show plume-like behavior. In other words, the velocity profiles become wider as they go to a higher part of the plume, while the maximum velocity gets slower.

Fig. 3.7 shows the normalized entrained fluid velocities at different heights. The fluid velocity was normalized with the centerline velocity, and the plume radius was normalized with plume width obtained from the best-fit Gaussian curves. The data in the figure show that the Gaussian velocity profile matches the data well throughout the zone of established flow.

3.3.2 Mean Flow Characteristics

From the fitted Gaussian and Monkewitz curves to the time-averaged velocity field data, average flow characteristics are obtained. Fig. 3.8 illustrates the non-dimensionalized centerline velocity and plume width for the bubble phase (a and c) and the fluid phase (b and d). To compare the results for different gas flow rates, the centerline velocity and plume width have been non-dimensionalized by the height in the plume z and the kinematic buoyancy flux B, which is defined as

$$B = Q_0 \frac{\Delta\rho}{\rho_w} \frac{H_A}{H_T} g \tag{3.4}$$

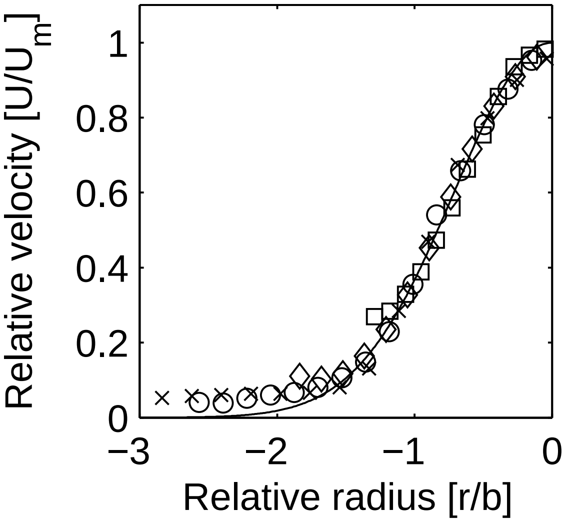

Fig. 3.7. Normalized fluid phase velocity at $z = 100$ mm($\circ$), $z = 200$ mm($\times$), $z = 350$ mm($\diamondsuit$), $z = 500$ mm($\square$).

where Q_0 is the volume flow rate of air bubbles at STP, H_A is the atmospheric pressure head (10.4 m), and $H_T = H_A + h$ is the static pressure head at the diffuser, where h is the depth of the diffuser. $\Delta\rho$ is the density difference between fresh water ($\rho_w = 1000$ kg/m^3) and air ($\rho_a = 1.4$ kg/m^3). Then, the non-dimensional parameters for a simple bubble plume can be given by dimensionless centerline velocity U_m^*, dimensionless height from the release point z^*, and dimensionless plume width b^* as follows:

$$U_m^* = \frac{U_m(z)}{(B/z)^{1/3}} \tag{3.5}$$

$$z^* = \frac{z}{H_T} \tag{3.6}$$

$$b^* = \frac{b(z)}{z} \tag{3.7}$$

These non-dimensional combinations are the common choice for presenting plume data.

As shown in Fig. 3.8(a), the non-dimensional centerline velocity for the bubble

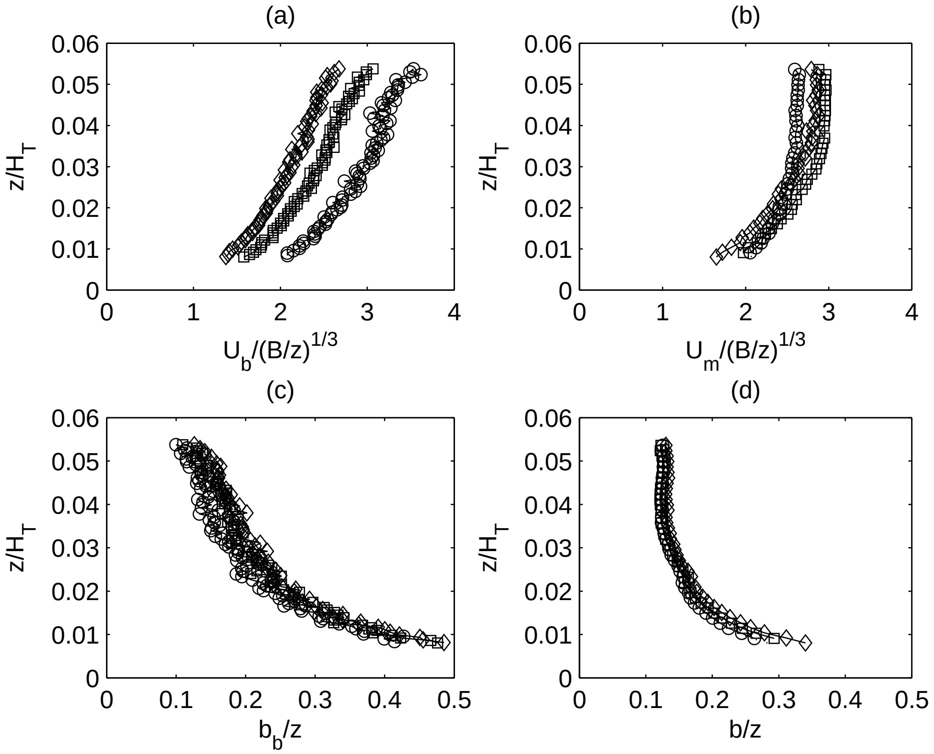

Fig. 3.8. Centerline velocity for the bubble phase (a) and entrained fluid phase (b) and plume width for the bubble phase (c) and the entrained fluid phase (d) for bubble flow rates of 0.5 l/min (○), 1.0 l/min (□), 1.5 l/min (◇).

phase steadily increases with plume height, but also with bubble flow rate. The effective bubble slip velocity (velocity difference between a bubble and the mean flow of the surrounding water) varies with bubble size and bubble concentration (Schlüter & Räbiger 1998) and increases with increasing air flow rate in our experiments. Each air flow rate results in a slightly different bubble size and group swarm characteristics; hence, each air flow rate has a different characteristic bubble slip velocity. The dimensional combination $(B/z)^{1/3}$ is a characteristic velocity of the entrained ambient fluid that does not reflect the dependence of slip velocity on bubble flow rate. Thus, we would not have expected a collapse of the data in sub-plot (a) and the lack of data collapse is due to the variable effective slip velocity across experiments.

The other profiles in Fig. 3.8 do show good collapse of the data. For all flow rates, the non-dimensional centerline velocities of the fluid phase (sub-plot (b)) become steady above 0.035 in the non-dimensional plume height units. For both the bubbles and the entrained fluid, the variation of the non-dimensional plume width is steep in the lower part of the plume and shallower in the upper part of the plume. This variation of plume width with height shows that the bubble plume does not strictly follow self-similarity.

Based on the Gaussian profiles of the fluid velocity, the volume flux of the fluid phase can be calculated by integrating the fluid velocity profile curves. The volume flux of the plume water is then defined as

$$Q = \int_0^\infty 2\pi r(1 - C(z,r))u(z,r)dr \tag{3.8}$$

where $C(z,r)$ is the void fraction of air bubbles and $u(z,r)$ is the fluid velocity profile. For the experimental profiles, limits of the numerical integration were chosen as the half width of the tank; we also make the dilute plume assumption $(1 - C \approx 1)$. By

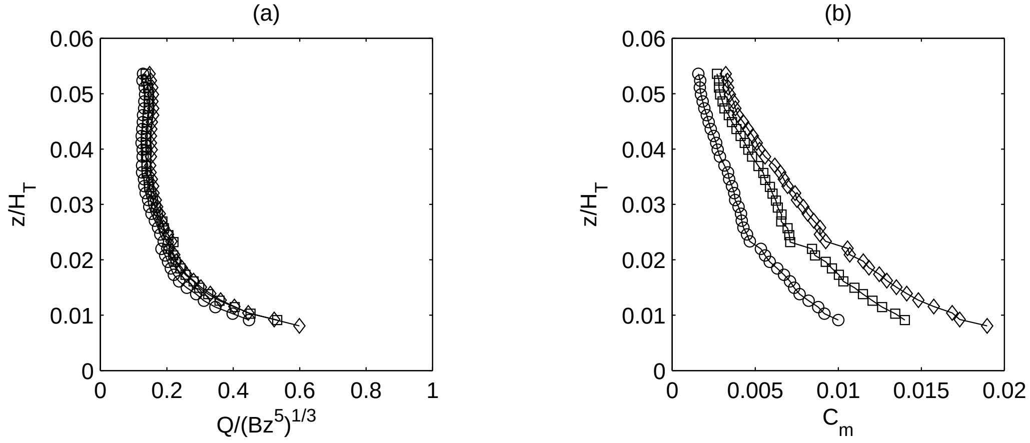

Fig. 3.9. Calculated entrained fluid flow rate (a) and void fraction (b) for bubble flow rates of 0.5 l/min (○), 1.0 l/min (□), 1.5 l/min (◇).

dimensional analysis, the entrained fluid flow rate is non-dimensionalized as follows

$$Q^* = \frac{Q}{(Bz^5)^{1/3}} \tag{3.9}$$

The calculated volume flux over the plume height is presented in Fig. 3.9(a). The non-dimensional volume flux of the fluid phase decreases sharply at the beginning but becomes steady as it rises. For different flow rates, there is no significant difference in non-dimensional fluid volume flux with non-dimensional height. This graph shows that the volume flux of the fluid phase depends on the initial buoyancy flux and plume height rather than the slip velocity.

The void fraction in the plume can also be calculated by assuming isothermal expansion of the bubbles. Using the ideal gas law, the known bubble flow rate is set equal to the bubble flux assuming a Gaussian distribution of bubbles (typical of integral plume models). The void fraction C is then computed from

$$Q_b(z) = \frac{Q_0 H_A}{(H_T - z)} = \int_0^\infty 2\pi r C(z,r)(u(z,r) + u_s)dr = \pi b^2 C(z)\left(U_m(z) + u_s\right) \tag{3.10}$$

where $Q_b(z)$ is the gas volume flux at any given height, $C(z)$ is the void fraction, and

u_s is the bubble slip velocity. The bubble slip velocity was estimated based on the mean equivalent bubble diameter. Here, the equivalent bubble diameter is defined as the diameter of a spherical bubble with the same volume as the ellipsoidal bubble in the raw images. The mean equivalent bubble diameters d_e in the experiments were extracted from the images as 1.51 mm, 1.71 mm, and 2.02 mm for 0.5 l/min, 1.0 l/min, and 1.5 l/min, respectively. The slip velocities for these bubble diameters were 16.76 cm/s, 18.26 cm/s, and 20.41 cm/s in tap water (Motarjemi & Jameson 1978). These velocities are in good agreement with the measured data. These values were used to calculate the void fraction as shown in Fig. 3.9(b). The calculated void fraction ranges 1 to 1.8% at the bottom and 0.2 to 0.7% at the top. These data verify the dilute plume assumption and also show that the void fraction is a function of bubble flow rate, which is to be expected.

3.3.3 Entrainment Coefficient

From the measured data, the effective entrainment coefficient α can be calculated by the relationship between the maximum mean velocity of the fluid phase and the volume flux into the plume (Milgram 1983), which is given by

$$\frac{dQ}{dz} = 2\pi b \alpha U_m \tag{3.11}$$

The gradient of volume flux was determined by fitting the volume flux data of Fig. 3.9(a) to a smooth curve to eliminate the noise amplification that occurs when applying dQ/dz to the raw PIV data. Using the obtained volume flux gradient and centerline values, the entrainment coefficients were determined as shown in Fig. 3.10. Until the non-dimensional water depth of 0.035, which is comparable with distance to 35 cm from the diffuser, the entrainment coefficient continuously decreases and lies in the range of 0.08 to 0.05. This agrees well with the pure plume value of 0.083 (Fischer

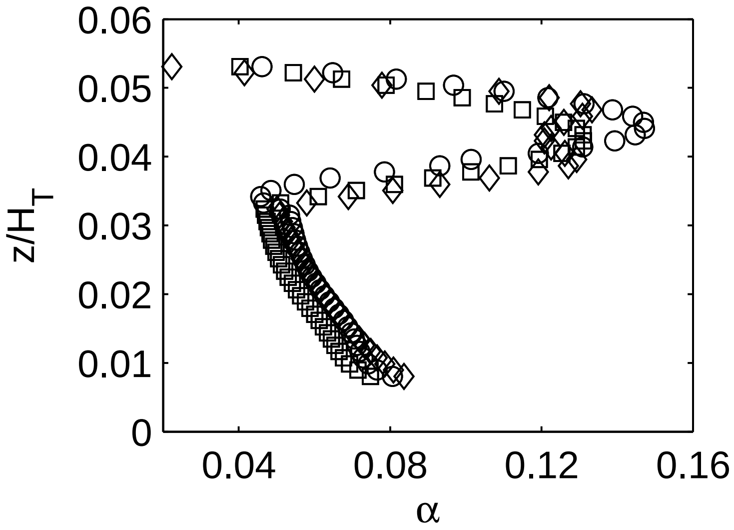

Fig. 3.10. The entrainment coefficient as a function of non-dimensional height for bubble flow rates of 0.5 l/min (○), 1.0 l/min (□), 1.5 l/min (◇).

et al. 1979). In this region, the plume behaves like a simple plume in an unbounded domain, and the non-constant entrainment coefficient value indicates that the plume is not strictly self-similar. Beyond this height, however, the entrainment coefficient grows abruptly up to 0.15 and then drops quickly near the water surface. This can be attributed to the water surface effect. In other words, after the plume hits the water surface, the plume fluid propagates outward from the plume center. This surface current causes a recirculation flow that influences the plume above $z^* = 0.035$. Hence, pure plume entrainment coefficients can only be inferred below the height of $z^* = 0.035$.

Milgram (1983) proposed the bubble Froude number as a scaling factor to provide a functional relationship between the entrainment coefficient and other local independent variables of a bubble plume. Using dimensional analysis, he found the bubble Froude number, which is the ratio of the mixing distance of bubble motions

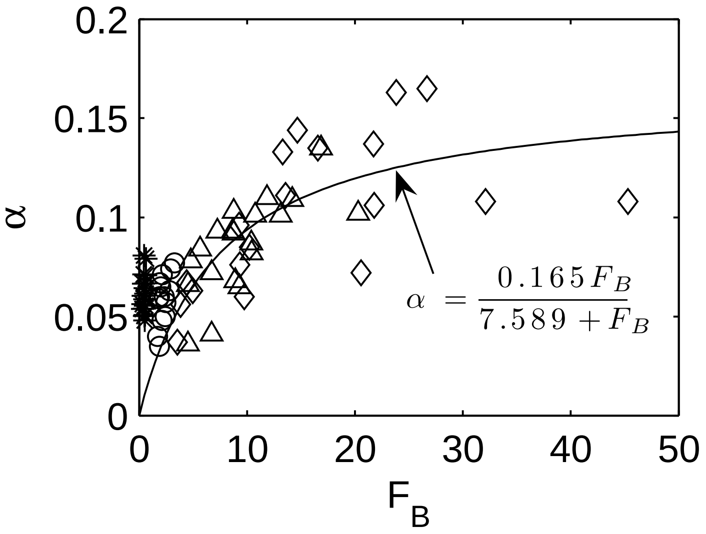

Fig. 3.11. Dependence of the plume entrainment coefficient on the bubble Froude number. Data from the present study are depicted by $*$. Other symbols present Kobus (1968) ($\circ$), Fennelop & Sjoen (1980) ($\triangle$), and Milgram (1983) ($\diamond$).

in the turbulence to the characteristic distance between bubbles, and is expressed as:

$$F_B = \left(\frac{Q_b^2}{g}\right)^{1/5} \frac{C^{1/3}\sqrt{g\Delta\rho}}{\sqrt{T}} \tag{3.12}$$

where T is the surface tension between an air bubble and water (0.072 N/m). Fig. 3.11 shows the correlation of α with F_B for our data along with the data presented in Milgram (1983). F_B ranged in our experiments between 0.25 and 0.65, whereas Milgram compared to data with F_B between 1 and 45. Although Milgram's correlation indicates $\alpha \to 0$ as $F_B \to 0$, the low F_B data from our experiments predict a minimum threshold value of $\alpha = 0.05$ to 0.04, which is also consistent with Milgram's data. Hence, a better correlation is required for α at low F_B.

In order that the effective entrainment coefficient for our three experiments can be collapsed to one regression curve, a relationship between the entrainment coefficient and the plume parameters was derived. Here, the independent plume parameters are B, z, and u_s. We use u_s as a single parameter that includes the effects of d_e,

T, and $\Delta\rho$. Using our three independent parameters, the dimensionless slip velocity can be expressed as $u_s/(B/z)^{1/3}$. This parameter is the ratio of the slip velocity to a characteristic entrained fluid velocity $(B/z)^{1/3}$. Socolofsky & Adams (2002) used this ratio to predict when multiphase plumes in crossflow would loose their plume behavior due to downwind detrainment, and this parameter is the analog of the non-dimensional slip velocity proposed by Socolofsky & Adams (2005) for a stratified ambient, $U_N = u_s/(BN)^{1/4}$, where N is the buoyancy frequency and $(BN)^{1/4}$ is a characteristic velocity. Then, the entrainment coefficient based on our experimental data below $z^* = 0.035$ gives the functional relationship

$$\alpha = \frac{B/u_s^3}{8.221z} + 0.0469 \tag{3.13}$$

Fig. 3.12 shows the relationship between the entrainment coefficient and the dimensionless slip velocity derived above. Entrainment coefficients measured by previous researchers (Kobus 1968, Fenneløp et al. 1991, Milgram 1983, Hugi 1993) are also plotted together for comparison. The data indicate the dependence of entrainment coefficient on the height from the source, initial buoyancy flux, and slip velocity. As shown in the graph, the entrainment coefficient decreases as the plume rises. Likewise, the higher the bubble flow rate, the larger the entrainment coefficient. This collapse of the data shows that the slip velocity together with the buoyancy flux and plume height can influence the entrainment in a simple bubble plume.

3.4 Summary and Conclusions

The PTV and PIV methods have been applied to obtain full-field velocity information in an unbounded air bubble plume in a quiescent, unstratified ambient condition. To keep the experiments and post-processing as simple as possible, a new phase

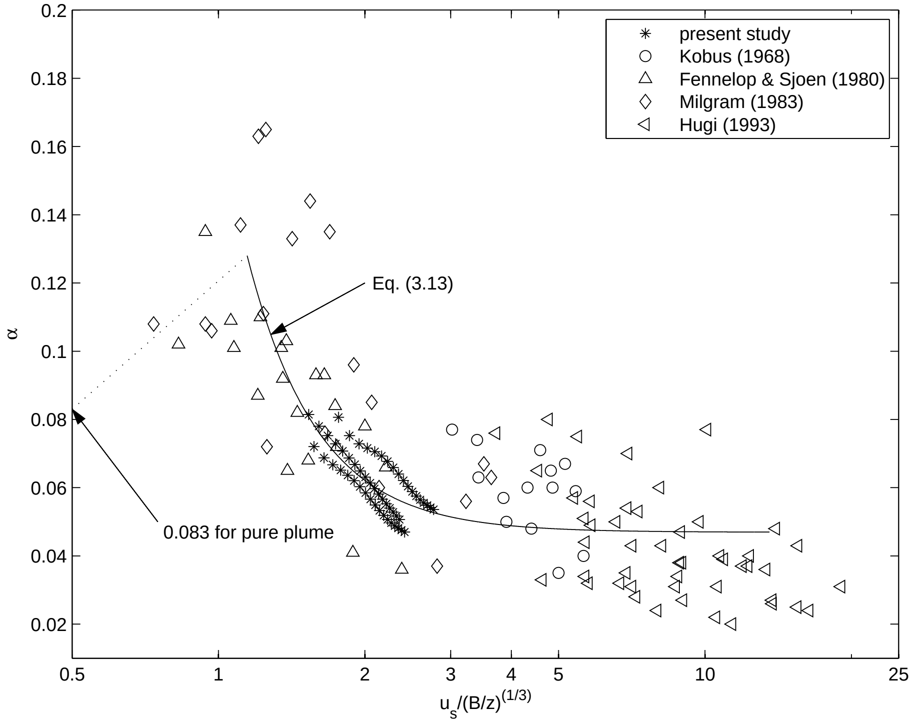

Fig. 3.12. The entrainment coefficient as a function of $u_s/(B/z)^{1/3}$.

separation method has been proposed. Mixed-fluid images are obtained during the experiments. Because the bubble phase reflects brighter than the PIV tracer particles, a gray-scale intensity threshold is applied to obtain images that contain the bubble signature only. These images are processed using the standard PTV method and then time-averaged to obtain the average velocity field data for the bubbles. The raw images are simultaneously processed using the standard PIV technique, resulting in vector maps containing the bubble and entrained fluid signatures. A maximum velocity threshold and vector median filter is applied to remove the bubble vectors; the parameters of the median filter are adjusted to give a match between the extracted bubble vectors from the PIV and the PTV data of the bubbles only. The remaining PIV vectors are interpreted to be the velocity field of the entrained ambient fluid. More detailed phase separation methods are available in the literature. However, this method is shown to be adequate for obtaining mean flow properties and is inexpensive, simplifying the task of phase separation, because it relies only on standard PIV and PTV functions available in most software packages.

From the phase separated velocity data, time-averaged results are obtained. The entrained fluid velocity data match well with the Gaussian profile, while the bubble velocity data match closer to a top-hat profile. By fitting Gaussian profiles to the entrained fluid data, results are obtained for the centerline velocity, plume width, entrained fluid volume flux and dispersed phase void fraction. These data are integrated to give a measurement of the bubble-plume entrainment coefficient as a function of height.

The important conclusions from these data are summarized as follows:

1. Time average results for the entrained ambient fluid of the centerline velocity, plume width, and volume flux can be non-dimensionalized using the governing

parameters B and z to achieve a good collapse of the data. This indicates that the slip velocity of the bubbles do not significantly affect these variables.

2. The entrainment coefficient evaluated from these data shows a significant dependence on slip velocity and height above the diffuser, likely due to variation in void fraction. This supports the understanding that a bubble plume is not self-similar.

3. By comparison to entrainment coefficient data from other researchers, there appears to be a minimum value of the entrainment coefficient in a bubble plume of around 0.04. This invalidates the dependence of the entrainment coefficient on the bubble Froude number as proposed by Milgram (1983) for bubble Froude number below about 2.

4. A new correlation of the entrainment coefficient in a simple bubble plume has been proposed that is a function of the non-dimensional slip velocity $u_s/(B/z)^{1/3}$ which is the cube of the ratio of the slip velocity to a characteristic velocity in the plume. Hence, entrainment depends on the relative velocity of the bubbles as compared to the velocity of the entrained ambient fluid.

CHAPTER IV

ACCOUNTING FOR BUBBLE EFFECTS IN CONCENTRATION FIELD MEASUREMENT IN A BUBBLE PLUME USING PLANAR LASER-INDUCED FLUORESCENCE (PLIF)[1]

4.1 Introduction

Multiphase plumes occur in many environmental applications, including air bubble plumes for reservoir destratification (Asaeda & Imberger 1993, Schladow 1993, Lemckert & Imberger 1993) and aeration (Wüest et al. 1992, Wain & Rehmann 2005, García & García 2006), liquid CO_2 plumes for direct ocean carbon sequestration (Liro et al. 1992, Adams et al. 1997, Alendal & Drange 2001), and deep-sea accidental blow-outs of oil and natural gas (McDougall 1978, Yapa & Zheng 1997, Zheng & Yapa 1998, Yapa et al. 1999, Johansen 2000), among many others. To assess the near-field mixing properties of multiphase plumes, it is important to understand the spatial and temporal variability of intermittent scalar field parameters as a result of turbulent motion in the plume (e.g. pH, O_2, N_2, or CO_2 concentration, temperature, etc.). This can be important to predict instantaneous dissolution rates of dissolving dispersed-phase constituents (Roy & Duke 2004) and to assess the effect of variable concentration fields on biologic communities (Caulfield et al. 1997). Most numerical models, including both integral and Reynolds average models, are designed to predict the time average concentration field, which is important to predict average

---

[1] This chapter has been submitted to *Experiments in Fluids* as Seol et al. (2008), "Accounting for bubble effects in concentration field measurement in a bubble plume using planar laser-induced fluorescence (PLIF)."

plume behavior and chronic toxicity. However, the actual plume concentration field is very intermittent, possibly containing frequent regions of acute toxicity levels, and this *in situ* patchy concentration field is what is experienced by passive organisms swept through the plume. To measure the instantaneous full-field concentration in a multiphase plume, we adapt the planar laser induced fluorescence (PLIF) method for application in a dilute bubble plume and present results for passive scalar intermittency. These data are important to understand the role of the dispersed phase to possibly alter scalar intermittency from that measured in single-phase plumes and to incorporate this understanding with numerical modeling results to predict the biologic impact of multiphase plumes in the environment.

An important example of a multiphase plume requiring careful design to avoid negative environmental impacts is a direct ocean carbon sequestration plume at mid-ocean depths (order 1000 m depth). Environmental impacts could be associated with the dissolved CO_2 concentration, which creates a narcotic effect at certain levels, and with the reduced pH due to reaction of the CO_2 with seawater (Caulfield et al. 1997). Deepwater microbial communities would be chronically affected by changes in pH, for instance, at levels on the order of 0.1 pH units (Adams et al. 1997, Riebesell et al. 2000). To design ocean carbon sequestration plumes, previous researchers used numerical techniques based on the integral model of a CO_2 droplet plume or based on two- and three-dimensional Reynolds average Navier-Stokes models to predict the pH change in the density-stratified near and intermediate field (Liro et al. 1992, Caulfield 1996, Caulfield et al. 1997, Alendal & Drange 2001). Even when acceptable near-field mixing is achieved to avoid chronic toxicity levels on average, intermittent concentration levels within the plume in the vicinity of the dissolving CO_2 droplets may exceed acute toxicity levels. Very fine-scale models, such as direct numerical simulation models in bubbly flows (Koynov et al. 2006), provide insight on bubble-scale intermittency, but larger-scale applications require experimental data.

The planar laser-induced fluorescence (PLIF) method has been widely used to quantify the scalar concentration field as well as to visualize the flow structure qualitatively of fluid flows in environmental fluid mechanics. This scalar measurement technique has been used in studying turbulent mixing around single-phase jets and plumes (e.g. Koochesfahani & Dimotakis 1985, Dahm & Dimotakis 1986, Ferrier et al. 1993, Cowen et al. 2001, Webster et al. 2003). Measurements of the concentration field with the PLIF technique are implemented using a fluorescent dye tracer excited with light at a wavelength within its absorption range. The dye emits longer-wavelength light with intensity which is proportional to the local dye concentration and incident laser power so that it is possible for a camera system to be calibrated based on the relationship between image intensity and local dye concentration. An optic filter is also used to record only the fluorescent light from the dye and block the laser light (Webster et al. 2003). After careful calibration, the digital images of the instantaneous intensity distribution are converted to the concentration field. Because the concentration depends on the incident laser light which is affected by the dispersed phase in a multiphase plume, we adapt the previous methods to account for reflection and obstruction by bubbles, particles, or droplets in multiphase flow.

Previous applications of LIF in multiphase flows have been applied to avoid the complicating effects of the bubbles. Socolofsky & Adams (2003) measured the fluorescence profile in a tank around a bubble plume with an *in-situ* point-measurement fluorometer after stopping the injection of bubbles to provide direct measurements of the average liquid fluxes. In Roy & Duke (2004), a dye quenching LIF method was used to directly measure the oxygen concentration around a single bubble. Koynov et al. (2006) studied the mass transfer and chemical reactions in multiphase flow using fixed bubble-shaped particle grids to avoid optical interference of bubbles. They argued that any single bubble rising through these grids experiences the same complex flow fields as the bubble swarm. However, the hydrodynamic interactions between bubbles are ignored in their study. Here, we measure the concentration field in a bubble plume by taking the light scattering characteristics of the bubbles into account to obtain instantaneous full-field concentration maps throughout the bubble plume and surrounding ambient fluid.

The principal purpose of this study is to describe the experimental techniques used to measure the passive scalar concentration field in a bubble plume. The results demonstrate that the proposed techniques are capable of providing quantitative measurements of scalar structure in a bubble plume with acceptably low levels of uncertainty. In the following Methods section, the designed experimental setup and the image correction methods are explained in detail. In particular, the calibration procedures to take the bubble interference into account are presented in this section along with verification of the proposed bubble reflection correction to demonstrate the applicability of the proposed method to a bubble plume study. The Results section presents the statistical properties of the concentration field of a bubble plume and compares the results to published values for single-phase plumes.

4.2 Methods: Experimental Setup

The experiments are conducted in a glass tank (Oceanic Co.) with dimension of 2 m long by 1 m wide by 1.5 m deep in the Ocean Engineering Wave Tank of the Zachry Department of Civil Engineering at Texas A&M University. Fig. 4.1 shows a sketch of the experimental set up. The large tank was used to minimize recirculation effects for the short-duration experiments presented here. The tank is filled with distilled water for the experiment since residual chlorine in city tap water reacts with Rhodamine

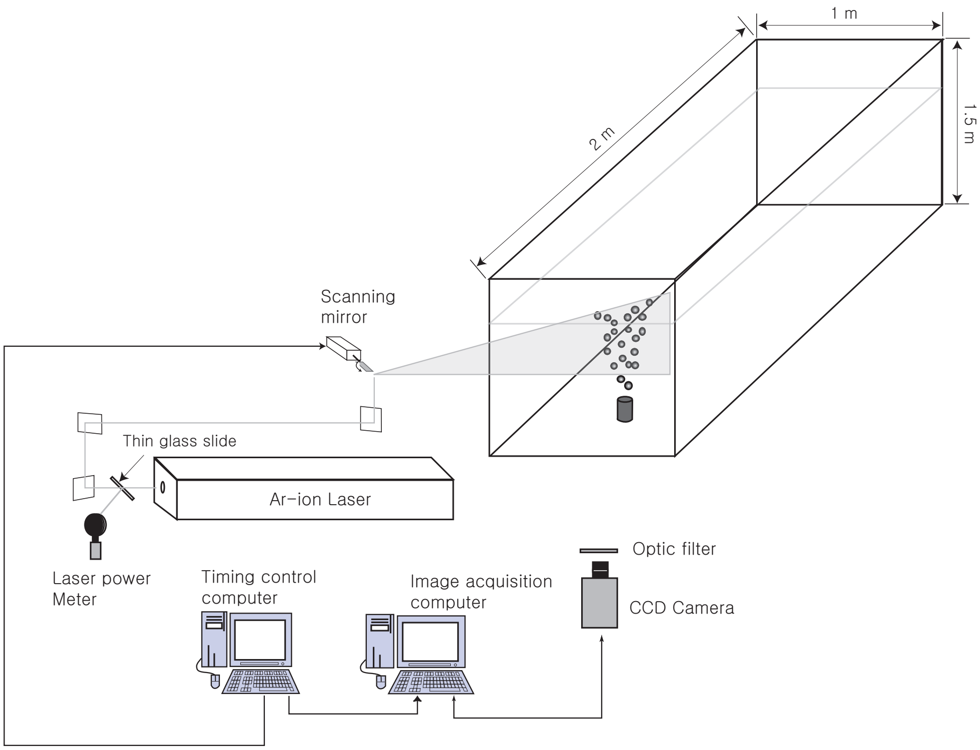

Fig. 4.1. Experimental set up.

6G to cause decay in dye concentration (Webster et al. 2001). The air is injected from a porous aquarium airstone diffuser with a diameter of 1.4 cm, which is fixed to the tank bottom. A needle valve and gas mass flow meter (Alborg GFM 171) enable precise control of the air flow rate from the air source. For the present experiments, the air flow rate is controlled to maintain 0.5 l/min at standard temperature and pressure. From careful inspection of raw bubble images, the average effective bubble diameter is 0.151 cm. The bubble slip velocity in pure water is determined as 33.46 cm/s based on Clift et al. (1978). The calculated Eötvös number is 0.3026 and the Reynolds number is calculated as 501.85. As observed in the experiments, bubbles should be wobbling ellipsoidal (Clift et al. 1978).

The measurement of the scalar structure of the bubble plume is based on PLIF techniques. A 6 watt Argon-Ion continuous laser (Stabilite 2017, Spectra-Physics Co., wavelength 514 nm) and one orthogonal fast galvanometer scanning mirror (Model6220, Cambridge Technology, Inc.) are used to produce a planar laser light sheet by scanning with uniform intensity through the centerline of a bubble plume. To monitor the laser power fluctuation, a standard microscope slide is placed in front of the laser aperture so that about 10 % of the laser beam power is reflected to a power meter (FieldMaxII-Top, Coherent, Inc.) (Cowen et al. 2001). A solution of fluorescent Rhodamine 6G dye is injected through a collar diffuser at the base of the plume so that it is well-mixed with entrained water at the injection point and follows the fluid phase of the bubble plume. Rhodamine 6G is efficiently excited by the laser light with a wave length of 524 nm and emits fluoresced light with a peak wavelength of the emission spectrum near 555 nm (Crimaldi & Koseff 2001). The dye is continuously injected with a consistent flow rate of 4.3 ml/s at a concentration of 1.5 mg/l from a Marriott bottle.

A high-resolution CCD camera (FlowMaster 3S, 12-bit intensity depth with

1024×1280 resolution) is employed to capture the highly-dynamic range of the concentration field of the small-scale flow structures. The size of the field of view is 14.6 cm in the horizontal direction and 17.5 cm in the vertical direction, the base of which is 29.5 cm above the diffuser, yielding a pixel resolution of 0.14 mm/pixel. From our previous research (Seol et al. 2007), the plume widths in the measurement area range from 4 cm at the lower part of the field of view to 6 cm at the top part of the field of view. The buoyancy length scale to describe the relative importance of momentum and buoyancy fluxes is calculated as 1.0212 cm with initial mean velocity of 50 cm/s at the diffuser followed by Papanicolaou & List (1988). The estimated height of the zone of flow establishment is 7.28 cm above the diffuser (Lee & Chu 2003). Thus, the field of view is in the fully-developed, buoyancy-dominated region of the plume. The measurement is conducted in the half of the plume on the side where the laser is incoming. The camera is equipped with a cut-on optic filter centered at 543 nm (543AELP, Omega Optical, Inc.) to block the original green laser light (514 nm) and transmit the fluorescent light (555 nm) from the fluorescent dye. Image recording is continued for 40 seconds, which totals 160 images (image acquisition frequency is 4 Hz). A 10 ms camera exposure time is used to capture one sweep of the laser beam through the tank from top to bottom. During the experiment, no contamination is observed due to recirculation of dye from the ambient water.

Three different types of experiments were conducted with this base experimental set up in order to obtain quantitative results. To calibrate a relationship between dye concentration and camera pixel intensity, the tank is filled with uniform dye concentration of known quantities. First, the uniform concentration tank is imaged in the absence of bubbles. This is identical to the calibration phase of the standard PLIF method. Second, the uniform concentration tank is imaged with the bubble plume flowing at the same flow rate as will be used in the quantitative experiments.

The combination of these two data sets allow the laser attenuation due to the bubbles to be evaluated as described in the next section on data analysis. For both these experimental steps, the laser beam is scanning one scan per camera frame as described above. Third, for one of the uniform concentration tanks with the bubble plume, the laser scanning is turned off so that the beam remains constant at one level through the tank for several images. This allows the light-scattering effects of the bubbles to be clearly seen in regions outside the beam path. This is necessary since the weak scattered light signal is lost when scanning since the laser scan is much brighter than the scattered light. This third set up is used to support our proposed method to account for laser attenuation due to bubbling. After these three steps are completed, the PLIF method is fully calibrated as ready for application in the measured plume case having zero background concentration.

4.3 Methods: Data Analysis

The calibration steps required for PLIF in bubble plumes are similar to the standard PLIF method with a few extra steps required to account for the presence of the bubbles. The whole calibration process is described in this section.

4.3.1 Raw Image Processing

All raw images captured in all phases of the calibration and measurement process must be corrected for CCD background noise and camera lens vignette. This is done following Tian & Roberts (2003) using a standard image, the uniformly back-lit image, and a blacklevel image, recorded with camera cap on, and processed according to Tian & Roberts (2003):

$$I_{c1}(i,j) = K\frac{I_{raw}(i,j) - I_b(i,j)}{I_s(i,j) - I_b(i,j)} \tag{4.1}$$

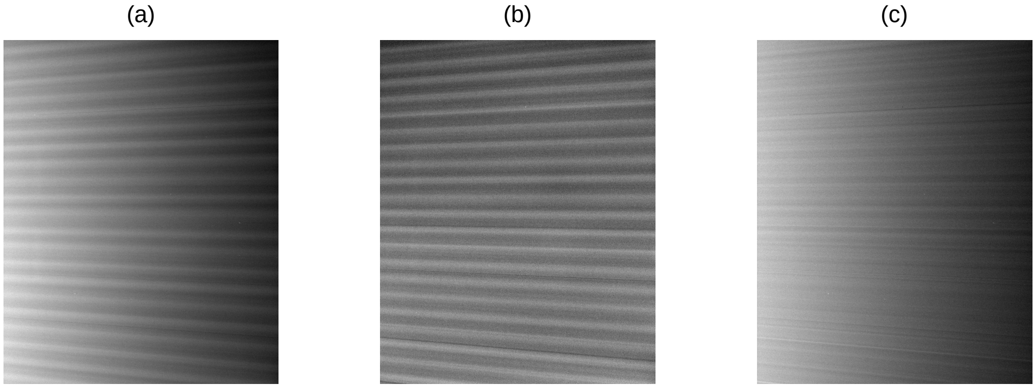

Fig. 4.2. Correction for vertical non-uniformity of laser intensity: (a) raw image, (b) correction base image, and (c) corrected image.

where $I_{c1}(i,j)$ is a corrected image intensity for background noise and lens vignette, K is the average pixel value in the standard image, $I_{raw}(i,j)$ is a raw image intensity, $I_b(i,j)$ is a blacklevel image, and $I_s(i,j)$ is a standard image. i and j are indices in a pixel coordinate system at horizontal and vertical direction, respectively.

Due to the refraction of the laser beam through the glass tank wall, horizontal line-like features were also observed in the raw image (Fig. 4.2(a)). In the figure, the laser is incoming from left to right of the field of view. To correct these defects, 50 images of uniform dye solution (e.g., 30 μg/l) were recorded using the PLIF method and averaged. In this average image, each column was then normalized by the mean intensity value of the column to obtain a correction base image (Fig. 4.2(b)). Raw images were corrected by dividing with the correction base image similarly to Ferrier et al. (1993). The result is shown for one of the uniform dye intensity images in Fig. 4.2(c). This correction is made for all recorded PLIF images.

4.3.2 Accounting for Bubble Signatures in the PLIF images

During all of the experiments with bubbles, bubble signatures are present in the images due to reflection of the fluoresced laser light off the bubble interface and due to shadows created by bubbles that block the laser beam path. Bubbles and shadows created by bubbles were removed after correcting the raw images for CCD background noise, camera lens vignette, and vertical non-uniformity, but before processing the images for quantitative concentration measures.

For the experiments with uniform background concentration, the bubbles are clearly identifiable as dark spots in the images. In this case, bubbles are removed using standard image processing techniques (image segmentation, area open, and digital masking) as described in Seol & Socolofsky (2008). After applying the digital mask, the remaining image contains only entrained and ambient fluid.

For the experimental measurements with zero background concentration, the bubble signatures cannot be automatically detected because of similar image characteristics for the dark, entrained ambient fluid. However, bubble signatures can be discerned by eye. To remove bubbles in this case, bubble mask templates are created by choosing bubble images from the raw image. The bubble mask templates are generated by assuming the bubble shape is an ellipse. Bubbles are identified manually in the raw images and separated into 2 size classes through visual inspection. The center of each bubble is then found by hand and recorded in a bubble location matrix for each image. The diameters of bubbles in this study are between 11 pixels to 28 pixels, which is comparable to 1.5 mm to 4 mm in diameter for small and large bubbles. By applying prepared bubble mask templates to the bubble location matrix, a binary bubble mask template is generated (0 for bubbles and 1 for the other area) for each image. By multiplying this binary bubble mask template with a raw image, bubbles are removed. On average, 210 bubbles are identified and removed from each instantaneous concentration field. This step was performed by hand to insure that all bubble are removed and no data are lost.

Shadows in all of the experimental images are also removed by hand. The thickness of shadows depends on the size of bubbles. Since the shadows are parallel to the laser beam path, they are easily found and removed in a radial coordinate system using a similar binary mask template. Here, the radial coordinate system refers to the transformed coordinate system of laser scan angle (θ) and radius of the laser beam (r) from the pixel coordinate system of i and j.

4.3.3 Correction for Laser Attenuation

The bubble- and shadow-removed images are next corrected for laser attenuation. The laser beam is attenuated by the local concentration of dye, bubbles and water itself. We follow the general PLIF method and assume that these effects are incorporated into a combined attenuation coefficient given by

$$a = a_w + ca_d + \alpha a_v \tag{4.2}$$

where a_w is the laser attenuation coefficient due to water, a_d is the laser attenuation coefficient due to local dye concentration, and a_v is the laser attenuation coefficient due to the bubble plume; c is the local dye concentration, and α is the local time-average void fraction in the bubble plume. The third term in this equation is the main contribution of this paper. Each of the attenuation coefficients a_w, a_d, and a_v is evaluated separately, the first two following standard, well-known procedures.

To measure the laser attenuation in water a_w, a small Plexiglas bottle containing very low concentration of dye solution (3 μg/l) is imaged at different locations along the laser beam path in the field of view. Each location is 2 cm apart from the other. The measurement has been made at 5 different locations. The height of the test bottle is adjusted to have the same height as the scanning mirror so that the image intensities are sampled along the 0° scanning angle. Since the laser power decays exponentially with distance (Koochesfahani & Dimotakis 1985, Ferrier et al. 1993,

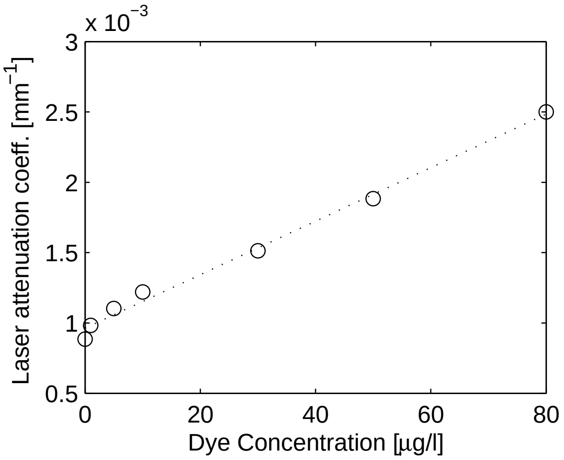

Fig. 4.3. Laser attenuation coefficients for sample dye concentrations.

Tian & Roberts 2003), the exponential decay curve fitting is applied to the mean image intensities of the test bottle along the beam path to find the laser attenuation coefficient for water. a_w is obtained from the Plexiglas bottle tests and is given by $8.33\times10^{-4}\text{mm}^{-1}$ for the distilled water used in our experiments.

To evaluate the laser attenuation due to dye a_d, LIF images are obtained for uniform dye concentrations in the absence of bubbling. Six different uniform concentration levels (0, 5, 10, 30, 50, and 80 μg/l) are prepared in the tank. For each concentration level, 50 images are captured and averaged to generate a single calibration image. As explained in the previous paragraph, a laser attenuation coefficient for each concentration level is determined by applying exponential decay curve fitting to a single horizontal line of a calibration image. The measured laser attenuation coefficients for different concentration levels are shown in Fig. 4.3. The laser attenuation coefficient for local dye concentration is determined as $1.841\times10^{-5}(\mu\text{g/l})^{-1}\text{mm}^{-1}$ by finding the slope of the fitted graph in the figure (Ferrier et al. 1993).

To investigate the effects of the bubbles on the concentration measurements, we first interrogate the images takes for uniform dye concentration with bubbles but

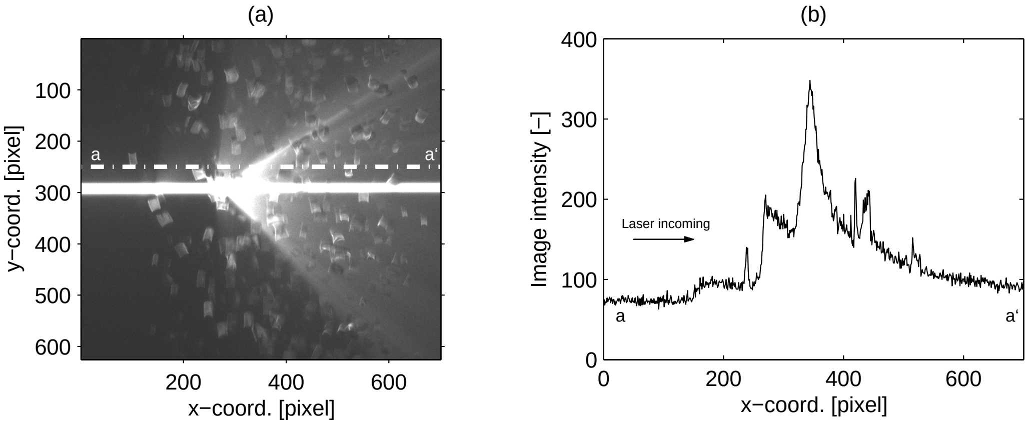

Fig. 4.4. Light scattering properties of bubbles. Sub-plot (a) shows a close up region for a non-scanning laser case. Sub-plot (b) shows the image intensity along the path a-a' in sub-plot (a).

without laser beam scanning. In this set up, the laser beam remains fixed at one level so that reflections and scattering from the beam by bubble interference can be clearly seen. We observe that the light scattering after the laser beam hits a bubble is confined to a cone-shaped region projecting in the along-beam direction as shown in Fig. 4.4. Fig. 4.4(b) shows the image intensity profile from cross-section a-a' in sub-plot (a). The region of the image upstream of the bubble was not affected by reflections from the bubbles. From these images, we conclude that the measurements upstream of the bubbles should be unaffected by the bubbles, and we observe that a wide region downstream of a bubble interaction is affected by diffuse scattered light. When the laser beam sweeps, many bubbles at many different locations will interact with the beam, creating superposition of diffuse background reflections in the recorded images. Thus, we expect that the effect of bubble interference with the laser beam will be to create a diffuse brightening effect that should increase where there are more bubbles and should not affect measurements outside the bubble column.

To account for the scattered laser light within the bubble plume, we hypothesize that the image intensity by bubble light scattering is proportional to the probability that the laser beam hits a bubble, which is comparable with the local void fraction α as follows (Cartellier & Achard 1991, Simiano et al. 2006):

$$\alpha(i,j) = \frac{\sum_i T_{G,i}}{T} \tag{4.3}$$

where $T_{G,i}$ are the gas presence time and T is the total duration of measurement. The local time-averaged void fraction was calculated using the calibration images from uniform dye concentrations with bubble injection (total 300 images comparable to 75-second data sets). Then, the local void fraction at a single pixel point in an instantaneous image is calculated by counting 0 when the liquid phase is present and 1 when the gas phase is present. A bubble is assumed to stay at a local point for the full camera exposure time (e.g., 10 ms). The number of exposures when a bubble is present is recorded as n. If T is the total measurement time (e.g., 75 sec), the local time-averaged void fraction is defined by

$$\alpha(x_i) = \frac{n\Delta t}{T} \tag{4.4}$$

where x_i is a local pixel point and Δt is the camera exposure time. The calculated local time-averaged void fractions at different heights are presented in Fig. 4.5. The local time-averaged void fraction ranges from 0.3 % to 1 % along the plume centerline. The error bars in the figure represent the standard deviation of measured void fractions from several sets of images (50 images per set).

The laser attenuation coefficient for the bubbles was then obtained by adjusting image intensity profiles of the uniform dye solution with bubble injection to align on the average value (the dotted lines in the figure) within 3 % error as shown in Fig. 4.6. Fig. 4.6(a) shows image intensity profiles of the uniformly mixed dye solutions with bubble injection after correcting attenuation by only water and dye concentration.

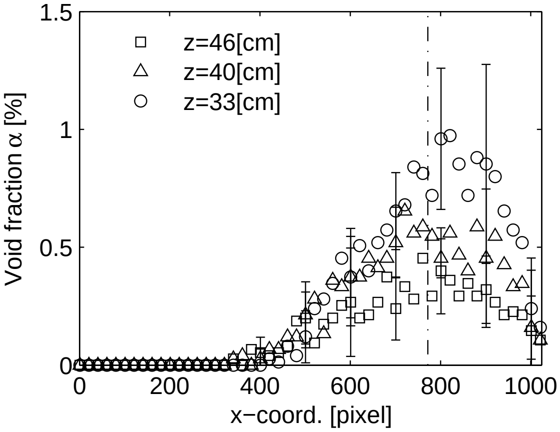

Fig. 4.5. Local time-averaged void fraction. The vertical dash-dotted line shows the bubble plume centerline.

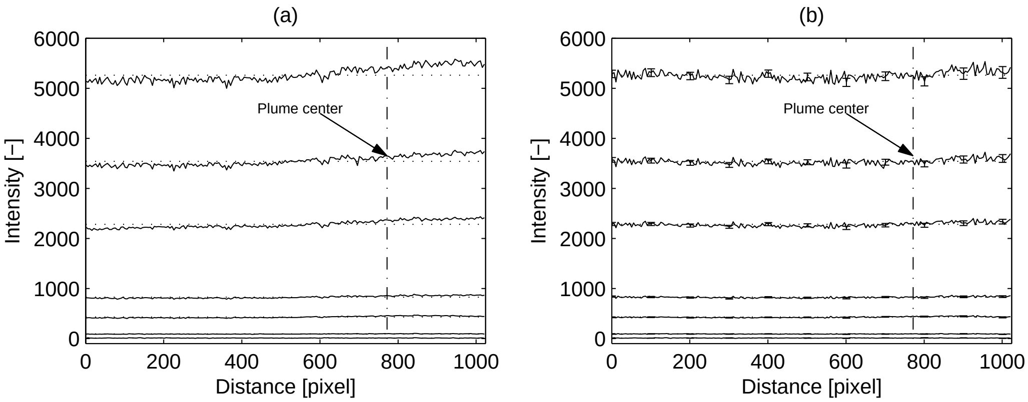

Fig. 4.6. Image intensity profiles for uniform dye calibration solutions after correcting for attenuation by bubbles. The error bars represent the standard deviation for each column in the image at the reported radial distance.

The intensity profiles are obtained by averaging 50 images for each dye concentration. After calibrating to obtain a straight profile, the obtained a_v is $-7 \times 10^{-4}\%^{-1}\mathrm{mm}^{-1}$; the negative sign indicates that the bubbles disperse laser light so that the laser power increases in the bubble plume, as expected from Fig. 4.4. Fig. 4.6 (b) shows the image intensity profiles after correcting attenuation by bubbles. The image intensity profiles are much more uniform than before correction. Note that the dotted lines are mean intensity profiles from the corrected images and the error bars in the sub-plot (b) represent the standard deviation of the image intensity along each column. The standard deviations around the bubble plume center show relatively higher values than outside plume, as would be expected.

4.3.4 Dye Concentration Calibration

The final step to obtain quantitative concentration measurements is to relate the corrected image intensities to concentration. The local dye concentration required in Eq. (4.2) is computed from the calibration relationship between the image grayscale intensity and the concentration of dye obtained from the calibration experiments without bubbles. After transforming each raw image to a radial coordinate system along the beam path, local dye concentration c is computed from

$$c(r,\theta) = \frac{I_c(r,\theta) - B(r,\theta)}{A(r,\theta)} \tag{4.5}$$

where $I_c(r,\theta)$ is the image intensity corrected for CCD background noise, camera lens vignette, and vertical non-uniformity and transformed to the radial coordinate system. $A(r,\theta)$ and $B(r,\theta)$ are the slope and intercept obtained from the average uniform dye calibration images before laser attenuation correction.

After determining the local dye concentration c, further laser attenuation correc-

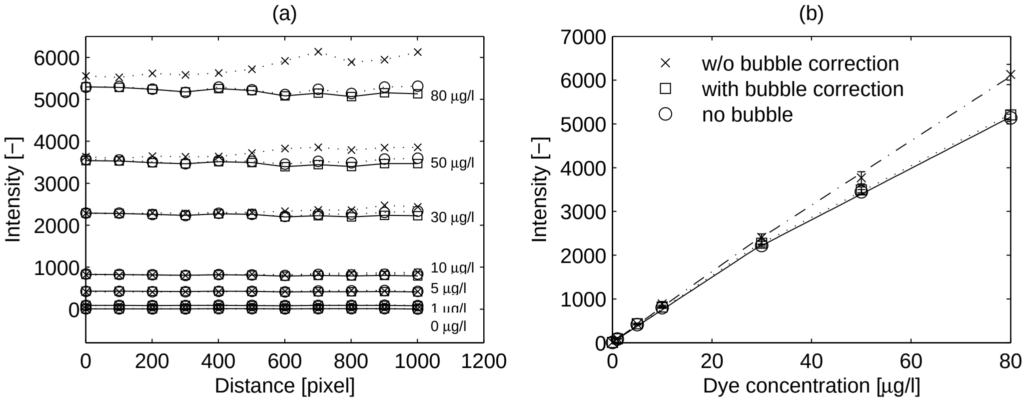

Fig. 4.7. Corrected uniform dye concentration profiles (a) and dye calibration results (b).

tion is made by integrating Eq. (4.2) pixel-by-pixel along the beam path as follows

$$I_{cc}(r,\theta) = \frac{I_c(r,\theta)}{-\exp\left(\int_0^r a dr\right)}. \tag{4.6}$$

After this attenuation correction, the images were transformed back to a pixel coordinate system of i and j. The corrected calibration images were used to calculate new correlation coefficients $A^{'}(i,j)$ and $B^{'}(i,j)$ for the slope and intercept relating corrected image intensity I_{cc} to the actual dye concentration at each pixel $C(i,j)$. This concentration is then computed for all images by

$$C(i,j) = \frac{I_{cc}(i,j) - B^{'}(i,j)}{A^{'}(i,j)} \tag{4.7}$$

The concentration maps $C(i,j)$ then contain the true dye concentrations in the full camera field of view.

Fig. 4.7 shows corrected uniform dye concentration profiles taken from 36.7 cm above the diffuser (a) and dye calibration results at a pixel point inside the plume (b). The maximum standard deviation of the concentration measurement was 2.9 %. Note that the results from the bubble injection case are obtained by averaging

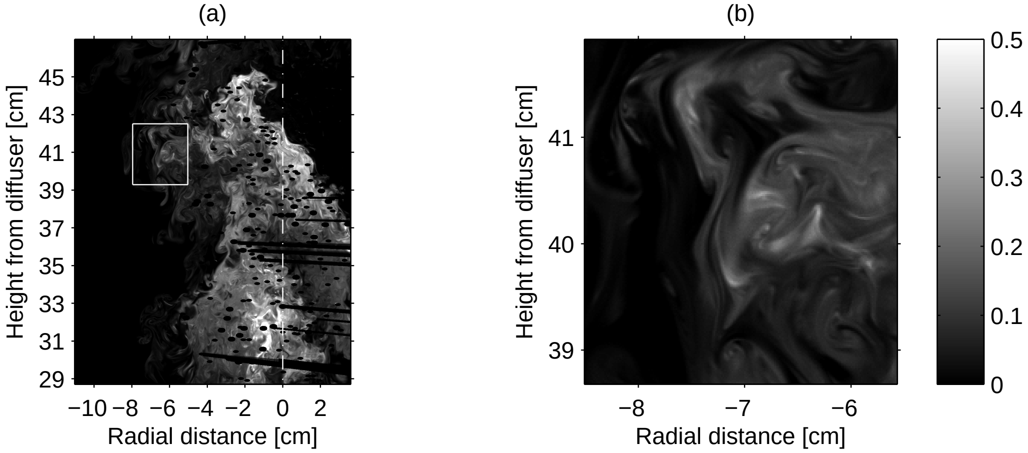

Fig. 4.8. (a) Instantaneous concentration field of bubble plume. (b) Close-up concentration field of box from figure (a). Vertical dashed line shows bubble plume centerline.

instantaneous calibration images after removing bubbles and shadows.

4.4 Results and Discussion

4.4.1 Instantaneous Concentration

Using the slope of the dye calibration results (Fig. 4.7(b)), raw images are corrected and converted to dye concentration fields. Fig. 4.8 shows sample concentration fields of the instantaneous flow structure of a bubble plume for the measurement experiments. In Fig. 4.8 (a), the plume center line is plotted as dashed lines. The concentration is normalized with the maximum concentration over the instantaneous concentration field. Note that the normalized concentration scale has been reduced for better display.

In the instantaneous concentration field, some well-known flow structural features are visualized. High concentration patches wander off the plume center, which demonstrates the turbulent intermittency and entrainment. This may be attributed to plume wandering or also to large-scale vortices in the plume. The instabilities of the shear layer are shown as dye-laden fluid is mixed with the entrained surrounding fluid by various sizes of vortices. The high variability of the spatial distribution in the instantaneous concentration field is also observed such that patches of high concentration are found in the area around the center of the plume and the concentration level is getting less on near the edge of the plume. However, large regions throughout the plume centerline also have low concentrations. Fig. 4.8 (b) shows a magnified view of the concentration image near the edge of the plume. Highly intermittent features are exhibited in the figure, which is attributed to the entrainment of ambient water into the plume region (Papanicolaou & List 1989).

4.4.2 Time-Averaged Concentration and RMS of Concentration Fluctuation

The time-averaged concentration field is used to calculate the concentration statistics. The duration of the averaged instantaneous data is 40 seconds, which is comprised of 160 instantaneous images. On average, it takes 1.125 seconds for generated vortices in this plume to travel from the bottom to the top of the field of view. The characteristic time scale (L/u_s) for the plume is estimated using the height of the field of view (L=17.5 cm) and bubble slip velocity (u_s=16.76 cm/s) as 1.044 seconds. Based on this time scale, about 38 flow cycles are captured in this measurement. Using the time-averaged concentration field, the instantaneous concentration fields are decomposed into the sum of the time-averaged concentration ($\bar{C}$) and the concentration fluctuations ($c^{'}$). The time-averaged concentration fields are shown in Fig. 4.9. The strength of concentration fluctuation can be quantified by the root mean square (RMS) value of the concentration fluctuation ($c^{'}$). Fig. 4.10 shows the image of the RMS concentration fluctuation. Note that this data is normalized with the maximum concentration value from the time averaged concentration field.

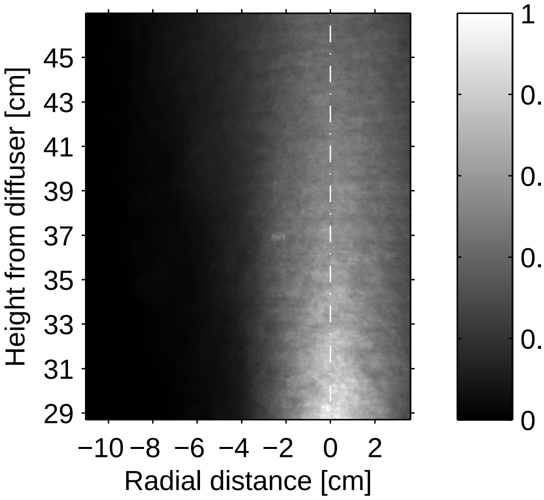

Fig. 4.9. Time-averaged concentration field.

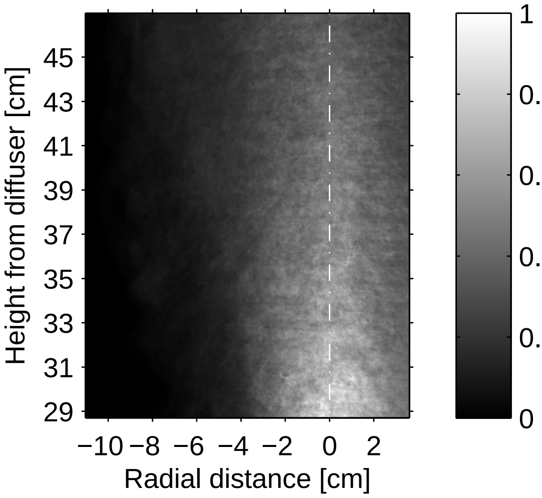

Fig. 4.10. Time-averaged RMS of fluctuation concentration field normalized by the maximum time-averaged concentration.

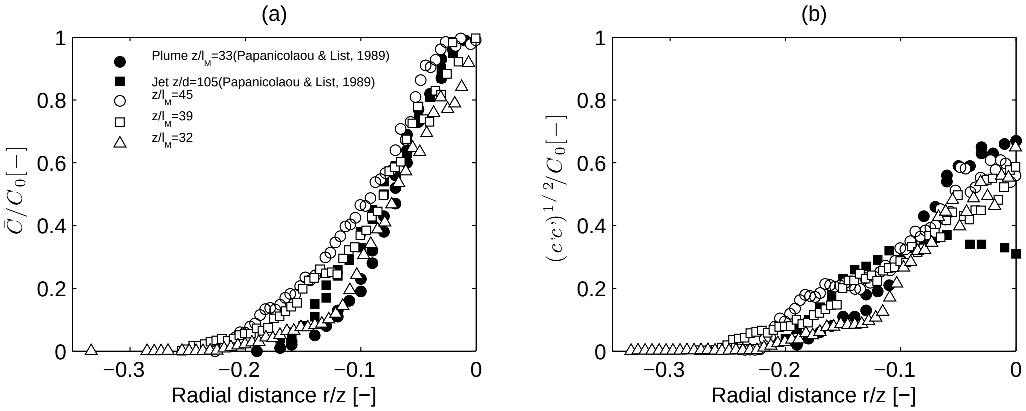

Fig. 4.11. Time-averaged concentration profiles (a) and RMS fluctuation profiles (b).

In Fig. 4.11, mean concentrations and rms values of concentration fluctuation at different heights are plotted. Here, the height is non-dimensionalized with the buoyancy lengthscale (l_M) defined as

$$l_M = \frac{M^{\frac{3}{4}}}{B^{\frac{1}{2}}} \tag{4.8}$$

where M is specific momentum flux ($= QU$, Q is the initial volume flux and U is the source mean velocity) and B is the initial buoyancy flux ($= g\Delta\rho Q/\rho_a$) (Papanicolaou & List 1989). The x-coordinate is non-dimensionalized with height. Fig. 4.11 (a) shows that the plume concentration properties are not strictly self-similar, which is a well-known attribute of a bubble plume. In Fig. 4.11 (b), the radial profiles of RMS concentration fluctuation are plotted together with previous results for a single-phase buoyant plume and jet (Papanicolaou & List 1989). Comparing to the single-phase plumes, intermittency is similar in shape for the bubble plume, but slightly lower in magnitude along the plume centerline. The results for the single-phase jet have peak values in the shear layer and decrease at the plume centerline. Bubble plumes have been shown to have both plume and jet characteristics, and the reduced intermittency along the plume centerline compared to a single-phase case is consistent with this observation. Results in the shear layer and edge of the plume are consistent with single-phase results, which would be expected since the bubble column is confined near the plume center. The lower intermittency for the multiphase plume in the center is also likely due to the enhanced turbulence from the dispersed phase wakes, which increase the turbulent diffusion.

4.4.3 Probability Density Function of Concentration

The converted dye concentration fields can be used to calculate the concentration probability density function (PDF) to study mixing properties in the bubble plume. Fig. 4.12 shows the measured concentration PDFs at different heights above the injection along plume center (a), middle point between plume center and edge (b), and plume edge (c). Here, we found the plume center as the location of the maximum time-average concentration at each level. From the obtained plume center, we defined the plume edge as the radial location to the point with $1/e$ of the maximum concentration. The middle point is the point with the same distance from the plume center and plume edge. The concentration PDFs are obtained after normalizing the concentration maps by the maximum concentration of the concentration field averaged over all 160 images. As shown in the figure, the concentration PDF is more uniform lower in the plume, indicating a wide range of high and low concentrations. As the dye is mixed over the height, the concentration PDF exhibits positive skew, giving a preference to the lower, mixed concentrations. Along the radial direction, low concentrations are observed more frequently as we move away from the plume center. As shown in Fig. 4.11, the greatest intermittency is exhibited along the plume center line.

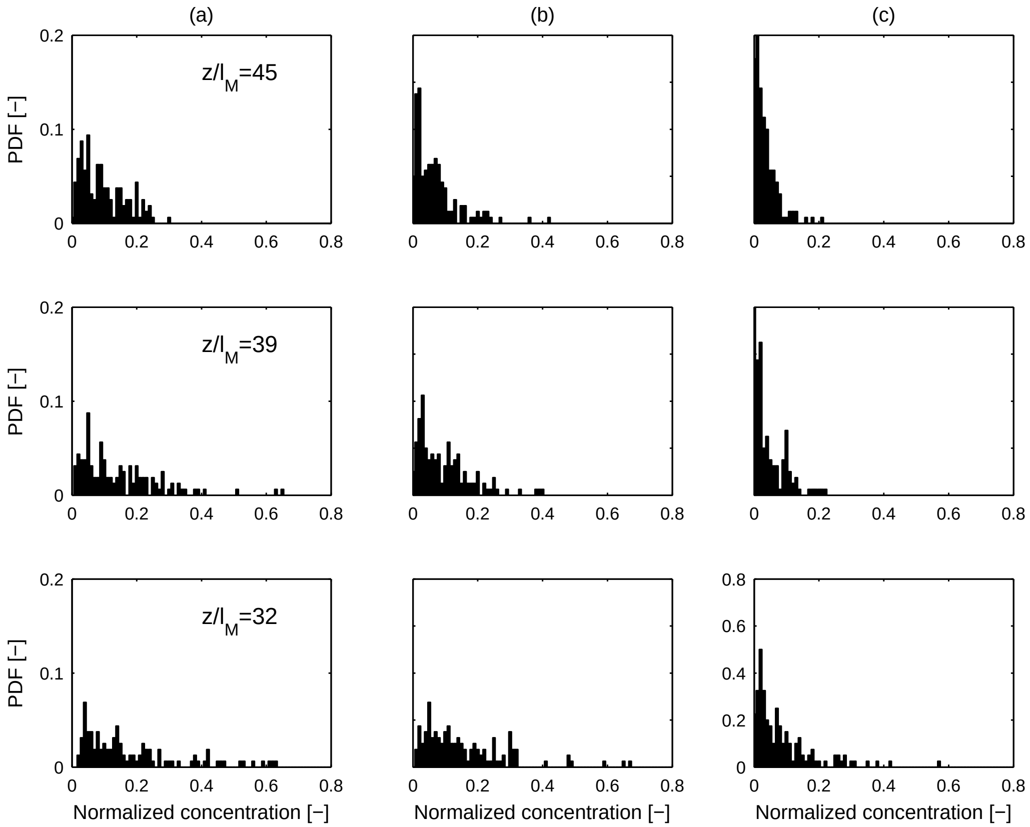

Fig. 4.12. Concentration PDFs at different heights above the bubble diffuser along the plume center (a), the middle point between plume center and edge (b), and the plume edge (c).

4.5 Summary and Conclusions

In this paper, we described a concentration measurement technique to quantify the scalar structure of a bubble plume. The instantaneous full-field concentration information in a bubble plume is measured by using the PLIF technique. To resolve problems caused by bubble reflection, the bubble signatures and shadows by the bubbles are removed using image post-processing. The light scattering properties of bubbles are taken into account in the dye calibration step by relating the laser attenuation to local void fraction. The sample results demonstrate some of the flow structural features of a bubble plume. The observed main features of the plume flow structures are summarized below:

1. The measured instantaneous concentration field demonstrates the entrainment process of the ambient fluid by continuous engulfment of zero-concentration ambient fluid.
2. The time-averaged concentration field shows that the plume concentration properties are not strictly self-similar; this is consistent with previous results for bubble plumes.
3. The RMS of concentration fluctuations show that highest fluctuation of concentration exists along the plume center-line. This observation is in qualitative agreement with previous measurements for single-phase plumes (Papanicolaou & List 1989).
4. The fluctuations in the center are lower in bubble plumes than in single-phase plumes, and both levels of fluctuations converge in the plume shear layer and near the edge.

5. The calculated concentration PDFs reveal that a large occurrence of low concentration is also observed at the plume center. As the plume rises, the PDF graphs exhibit positive skew for all locations.

CHAPTER V

MEASUREMENT OF BEHAVIORAL PROPERTIES OF ENTRAINED AMBIENT WATER FOR STRATIFIED BUBBLE PLUME USING PLIF AND PIV

5.1 Introduction

Understanding the flow and mixing processes induced by a bubble plume in density stratification is of primary concern in the design of air bubble diffusers for lake/reservoir destratification and reaeration (Lemckert & Imberger 1993, McGinnis et al. 2004) and planning of deep sea CO_2 sequestration (Crounse et al. 2007). Air bubble plumes in density stratified environments have been the subject of numerous studies using lab-scale experiments (e.g. McDougall 1978, Leitch & Baines 1989, Baines & Leitch 1992, Zic et al. 1992, Asaeda & Imberger 1993, Lemckert & Imberger 1993, Socolofsky & Adams 2003, Socolofsky & Adams 2005), field-scale measurements (e.g. Lemckert & Imberger 1993, McGinnis et al. 2004), and numerical modeling (e.g. McDougall 1978, Schladow 1993, Wüest et al. 1992, McGinnis et al. 2004). In stratified multiphase plumes, the entrained ambient fluid driven by the dispersed phases is detrained (peeled) when the negative buoyancy force of the entrained fluid exceeds the drag force of the dispersed phase. The detrained water creates an annular structure of downdraught outer plume fluid and descends to a neutral buoyancy level, where lateral intrusion of the fluid takes place (Asaeda & Imberger 1993, Socolofsky & Adams 2003). Asaeda & Imberger (1993) and Socolofsky & Adams (2005) classified different types of bubble plume behavior based on the strength of density stratification, the slip velocity of the dispersed phase, and the buoyancy flux. This plume classification is closely related to the form of lateral intrusion of detrained water. When the detrained water descends and intrudes, it entrains ambient water and is reentrained into the bubble plume as well (Lemckert & Imberger 1993). Leitch & Baines (1989) and Baines & Leitch (1992) measured entrained liquid volume flux due to a bubble plume in a stratified and confined environment by measuring the temporal variation of density interface height. Socolofsky & Adams (2003) measured the entrained liquid volume fluxes by comparing salinity profiles before and after injecting bubbles combined with dye tracer profiles. In both these approaches, the unsteady effect of turbulence is neglected by ignoring instantaneous and local flow properties. Knowledge of the temporal behavior of detrained water is important, however, to understand plume dilution (entrainment) processes. To observe the spatial structure of a bubble plume in stratification, we apply particle image velocimetry (PIV) and planar laser-induced fluorescence (PLIF) methods to laboratory scale plumes. While this data is largely qualitative due to the complications from the stratifying agents (salt and ethanol), these data are useful to study the instantaneous flow and mixing processes induced by a bubble plume in density stratification.

The velocity fields of a stratified bubble plume are captured using PIV. Standard PIV methods have been adapted to measure the instantaneous and time-averaged properties of various two-phase flows (Gui & Merzkirch 1996, Gui et al. 1997, Delnoij et al. 1999, Brücker 2000, Deen 2001, Lindken & Merzkirch 2002). The major challenge in applying PIV to multiphase flows is in separating the velocity information from both the entrained continuous-phase and the dispersed phase, such as particles, droplets, or bubbles. Discrimination of one phase from another can be made in several ways, such as by generating two different images for each phase using optical separation (e.g. Hilgers et al. 1995), applying image processing techniques to a single image containing both phases to remove one phase based on particle size, brightness, or shape (e.g. Khalitov & Longmire 2002), or using the different properties of the statistical cross-correlation peaks in the PIV calculation to extract results for one of the phases in a mixed-phase image (e.g. Delnoij et al. 1999). Recently, Seol et al. (2007) and Seol & Socolofsky (2008) proposed a simple approach for phase separation in bubble plumes using PIV vector post-processing techniques. This method uses bubble velocity information from particle tracking velocimetry (PTV) analysis for real-time validation of the post-processing algorithm to discriminate entrained fluid velocity from the mixed-phase PIV velocity maps (Seol et al. 2007). This method requires a discernible difference between bubble velocity and fluid velocity and performs well at very sparse bubble regions (less than 10 % of the bubble plume image occupied by bubbles) (Seol & Socolofsky 2008). For this study, the bubble slip velocity is around 6 cm/s and most of the plume area is occupied by bubbles (more than 10 %) so that the phase discrimination is not performed. Thus, we compute the air-water mixture velocity in the plume region and the water velocity outside the plume, similar to Ryu et al. (2005) for breaking wave slamming.

Qualitative measurement and flow visualization of the detrained water are made with the PLIF technique. PLIF has been used in single-phase flow to quantify the scalar concentration field as well as to visualize the flow structure qualitatively. In multiphase flow, it is difficult to measure the whole concentration field when the dispersed phase scatters the laser light and creates shadows behind it as is the case in bubble plumes. To avoid light interference of bubbles in measuring dye concentration, Socolofsky & Adams (2003) measured the fluorescence profile of the tank water after stopping injecting bubbles with an *in-situ* fluorometer. Roy & Duke (2004) used the PLIF technique to measure the mass transfer rate through the interface of a single bubble, where the fluorescence directly represents the oxygen concentration. Koynov et al. (2006) studied the mass transfer and chemical reactions in multiphase flow using fixed bubble-shaped particle grids to avoid optical interference of bubbles. They argued that any single bubble rising through these grids experiences the same complex flow fields as the bubble swarm. Seol et al. (2008) measured the concentration field in a bubble plume by taking the light scattering characteristics of the bubbles into account to obtain instantaneous full-field concentration maps throughout the bubble plume in an unstratified ambient. In their study, a fluorescent dye is injected to follow the fluid phase of the bubble plume from the bubble injection depth. We adopted this method to measure the qualitative behavioral properties of the entrained/detrained water, but do not account for scattering from bubbles or present quantitative results.

The main purpose of this work is to measure the behavioral properties of the entrainment/detrainment of ambient water using PIV and PLIF techniques in a bubble plume in a quiescent, density-stratified ambient. The significance of this study is to provide information on the relationship between the flow characteristics and the scalar mixing process. Especially, these experiments will be focused on identifying coherent structures and mechanisms controlling mixing by multiphase plumes. In the following Method section, the designed experimental setup and the data processing methods are explained in detail. The Results section presents PIV measurement data. The measured PLIF images are presented to show flow properties of the bubble plume in density-stratified ambient.

5.2 Method

The experiments are conducted in a Plexiglas tank with dimension of 38 cm square and 80 cm in height in the Ocean Engineering Wave Tank Laboratory of the Zachry Department of Civil Engineering at Texas A&M University. The tank is stratified with salt and ethanol using the two-tank method (Socolofsky & Adams 2003). Ethanol is added in proportion to the salt concentration to create a uniform refractive index throughout the stratification (McDougall 1978, Daviero et al. 2001). To match the refractive index of two different solutions, one tank contains a mixture of ethanol and fresh water and another tank is filled with salt water. Note that the second tank is filled with only salt water for PLIF measurement and the mixture of salt water and tracer particles for PIV measurement so that the tracer particles stay in the test tank during the measurement and it is unnecessary to disturb the stratification to mix the tracer particles before PIV measurement; PIV and PLIF experiments are conducted separately. The refractive index from the two solutions are matched using a hand refractometer (Model S-10E, ATAGO). The initial density profiles are measured by extracting samples from the tank and using an Anton-Parr density meter (Model DMA32N). The measured initial density profiles for PLIF and PIV measurements are shown in Fig. 5.1. Taking the approximately linear regions from the density profiles (0 to about 30 cm from the diffuser), the buoyancy frequencies, $N = [-(g/\rho)(\partial\rho/\partial z)]^{1/2}$, for PLIF and PIV measurements are 0.6425 and 0.7033 sec^{-1}, respectively.

The bubbles are injected from a porous aquarium airstone diffuser with a diameter of 1.4 cm, which is fixed to the tank bottom. A needle valve and gas mass flow meter (Alborg GFM 171) enable precise control of the air flow rate from the air source. For the present experiments, the air flow rate is controlled to maintain 0.1 l/min at standard temperature and pressure. The size and shape of a bubble depend on the fluid properties as well as flow rate. From careful inspection of raw bubble images, the effective bubble diameter is 0.12 cm and the shape of bubbles is spherical. Based on this effective bubble diameter, the calculated bubble slip velocity was 6.16 cm/s. The calculated non-dimensional slip velocities $U_N = u_s/(BN)^{1/4}$ are 1.053 and 1.077 for PIV and PLIF, respectively, where the plume can be categorized as type 1*

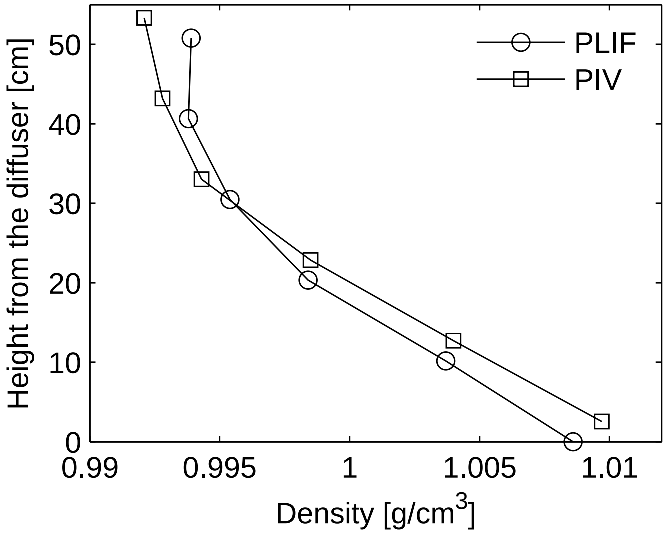

Fig. 5.1. Initial density profiles.

(Socolofsky & Adams 2005).

For both PIV and PLIF measurements, three cameras are used to cover the extent of the plume in the vertical direction. Two different kinds of CCD camera, a FlowMaster 3S camera (LaVision GmbH, 12-bit intensity depth with 1024×1280 pixel resolution) and two Basler cameras (10-bit intensity depth with 1004×1004 pixel resolution), are set up vertically to take the images of the entire plume above the diffuser. All cameras are equipped with Nikkor 50 mm focal length lenses. The sizes of fields of view of each camera are about 15×15 cm for the Basler cameras and 16×20 cm for the FlowMaster 3S camera. Note that PLIF and PIV measurements are made separately due to the limited resources of experimental equipment, such as CCD cameras and optic filter.

PLIF measurements are made to visualize the behavior of the entrained ambient fluid qualitatively. The measurements are made from 2.2 to 46 cm from the diffuser. As light sources, a continuous Ar-ion laser (Stabilite 2017, Spectra-Physics Co., λ=514 nm, 6 watt) is used to continuously generate 2D planar light sheets in combination with scanning mirror (Model6220, Cambridge Technology, Inc.) for the measurement. While the scanning mirror is configured to sweep the field of view from top to bottom once over 10 ms, the cameras are open for exposure during the sweep.

The PLIF image acquisition is started by turning on the bubble injection. A solution of fluorescent Rhodamine 6G dye is injected at the base of the plume so that it is well-mixed with entrained water at the injection point and follows the fluid phase of the bubble plume. Rhodamine 6G is efficiently excited by the laser light with a wave length of 524 nm and emits fluoresced light with a peak wavelength of the emission spectrum near 555 nm (Crimaldi & Koseff 2001). The dye is continuously injected with a consistent flow rate of 4.3 ml/s at a concentration of 1.5 mg/l from a Marriott bottle. 300 single-frame images were obtained from the PLIF measurements, which is comparable of 75 seconds of data duration. The characteristic time scale (L/u_s) for the plume is estimated using the height of the field of view (L=15 cm for the middle Basler camera) and bubble slip velocity (u_s=6.16 cm/s) as 2.43 seconds. Based on this time scale, about 30 times of flow cycles were captured in the experiments for each camera.

The velocity fields of the stratified bubble plume are measured using PIV. The three cameras covers the plume from 14 to 56 cm from the diffuser. A double-pulsed Nd:YAG laser (Spectra-Physics Quanta-Ray PIV-400, λ=532 nm, 320 mJ/pulse) and light-sheet optics are used to create 2D planar light sheets with 4 ms time interval. A pulse generator (Berkeley Nucleonics Corporation, Model 500A) is employed to externally trigger the laser. The pulse generator and the two cameras were synchronized using LabVIEW and a National Instruments PCI-6713 analog signal output board (12 bit by 8 channels). The image acquisition frequency of double-frames for PIV measurements is 4 Hz.

For PIV, non-fluorescent tracer particles are added to the water to track the entrained fluid at the stratification generation stage as mentioned earlier; the particles are white polyamide spheres with a characteristic diameter of 50 μm. Total number of acquired images are 90 double-frame images for PIV, which is 22.5 seconds of data duration. Based on the estimated characteristic time scale (L/u_s), 9.25 times of flow cycles were captured for PIV measurements for each camera.

5.3 Data Processing

As indicated in the previous section, PLIF and PIV measurements on stratified bubble plumes are made separately. Therefore, different data processing on the raw images obtained from the experiments are necessary. In this section, it is described in detail how the acquired images are processed to obtain quantitative data.

Raw images from the PLIF measurement are corrected for image distortion and adjusted for scale calibration. Before running the experiments, the images of a grid plate are recorded with the three cameras, which are set to cover around 43 cm of the whole plume vertically. Each camera is adjusted to overlap by 1 to 2 cm in each field of view. The grid plate image from the middle camera is selected as the base image for the scale calibration. The scale calibration is made with this base image and grid plate images from the other two cameras at the top and the bottom of the tank. The overlapping fields of view of the two cameras were geometrically corrected for image distortion using images of a single calibration grid plate based on the image dewarping algorithm (Willert 1997). In this way, three different cameras are aligned in one scale calibration. Then, the images from three different cameras are combined together to generate a single field of view image.

Different grayscale intensity depth from different cameras is also taken into account for image processing. The Basler cameras and the FlowMaster3S camera used in this study have 1024 and 4096 counts of maximum intensity depth, respectively. The raw images are normalized with the maximum intensity depth so that images from different cameras have the same intensity depth of 0 to 1. After time-averaging all images, however, we still find a discontinuity of image intensity between the Basler and the FlowMaster 3S cameras. Image intensities from the Basler cameras are higher than the ones from the FlowMaster 3S camera by around 26 %. By taking this difference into account, matched grayscales from two different cameras were obtained. Then, a threshold on image intensity is applied to define the entrained ambient liquid represented by fluorescent dye. The threshold value is carefully chosen when the entrained tracer dye is peeled off by looking at the created animations to visualize the entrainment/detrainment process. Using the built-in Matlab® image processing function and image threshold (e.g., 5%), raw images are converted to black-and-white images. In these black-and-white images, the entrained ambient water is represented by white (grayscale 1 count). Then, the peel height is defined as the maximum height where white area is observed.

The trap height is obtained by calculating the center of mass of the lateral intrusion of the detrained fluid outside the plume. For the calculation of trap height, the plume edge is pre-defined by obtaining the location with $1/e$ of the plume centerline velocity from time-averaged velocity field data. The defined plume edge is located at about 2 to 3 cm from the plume center. Then, the mass of the laterally intruding water is defined as the tracer dye image outside of the plume edge (Socolofsky & Adams 2003). The center of mass is calculated by finding the centroid of the area identified as the intruding liquid.

Raw PIV images are corrected for image distortion and adjusted for scale calibration before processing as with PLIF images. The cropped overlapping areas from the raw images are processed with the standard cross-correlation PIV algorithm. Due to the high number density of bubbles inside the plume and small bubble size, phase discrimination schemes fail to obtain separate velocity field information for the two phases. We employ an adaptive multi-pass PIV process using interrogation windows of 64×64 pixels at the first pass and 32×32 pixels in the second pass with 50% overlap at each pass.

5.4 Results and Discussion

The current study applies standard PLIF and PIV techniques to a bubble plume in density-stratified ambient conditions to study flow properties of the entrained ambient fluid. The following are the detailed description of the results of the measurements and the discussion.

5.4.1 Flow Structure of Entrained Ambient Fluid using PLIF

Fig. 5.2 shows a sample PLIF image (sub-plot (a)) and entrained ambient fluid obtained by applying threshold (sub-plot (b)). The figure clearly shows the intrusion of plume water into ambient water. Note that the dashed lines represent the location of the plume centerline and the two dotted lines in the sub-plot (b) specify the peel and trap heights. After converting to black-and-white to identify the area of entrained fluid, it was observed that very low concentration of ambient water is also entrained into the intrusion represented as black spots in sub-plot (b).

Fig. 5.3 shows the measured peel and trap height of the entrained ambient fluid (sub-plot (a)) and results of spectral analysis for the time-series data of the peel and trap height (sub-plot (b)). Initially, the detrained fluid due to the negative buoyancy goes down below the average trap height because of the downward momentum. It

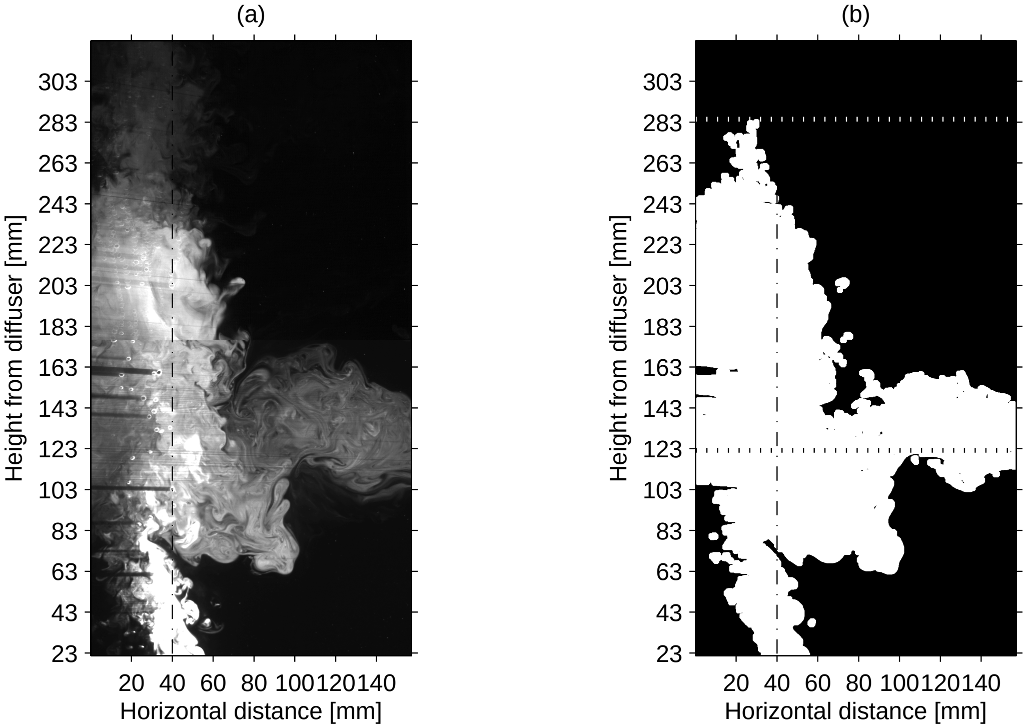

Fig. 5.2. Sample of PLIF image (a) and thresholded image (b) of a stratified bubble plume. The dashed lines represent the location of plume center, and upper and lower dotted lines represent the peel and trap heights in sub-plot (b), respectively.

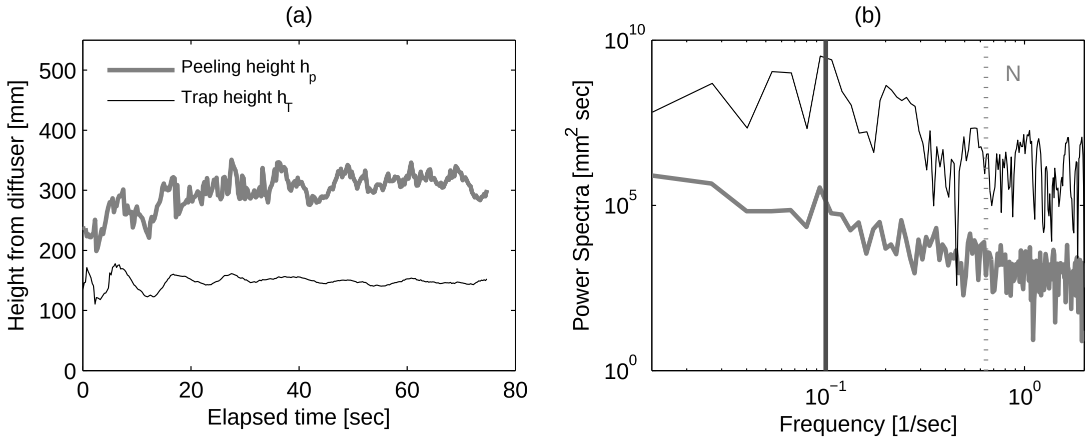

Fig. 5.3. Time series of measured peel and trap heights (a) and spectrum analysis results for the time-series peel/trap heights (b). In sub-plot (b), the shaded area indicates the identical frequency of peel and trap height fluctuation. The dotted line represents the buoyancy frequency of the ambient stratification.

bounces back and forth before reaching a stabilized trap height. In the sub-plot (b), the peaks of the calculated power spectra for the peel and trap heights coincide around 0.1 Hz as shaded in the figure. This shows that both the peel and trap height fluctuate in the early stage and then stabilized in the almost identical frequency as 0.0933 Hz and 0.0936 Hz for peel and trap heights, respectively. For comparison, the buoyancy frequency (N=0.64 s^{-1} for PLIF experiments) is also plotted as the dotted line in sub-plot (b). This discrepancy between the fluctuation frequency of the peel/trap height and the buoyancy frequency means there is no physical connection between the two; the observed oscillation is independent of the stratification.

To identify the nature of the discrepancy between the fluctuation frequency of the peel/trap height and buoyancy frequency, we compared the observed plume peel/trap hight oscillation frequency with plume oscillation frequencies from previous studies on plume wandering in unstratified cases as shown in Fig. 5.4. To compare with previous results, we non-dimensionalized the plume oscillation frequency (f) with

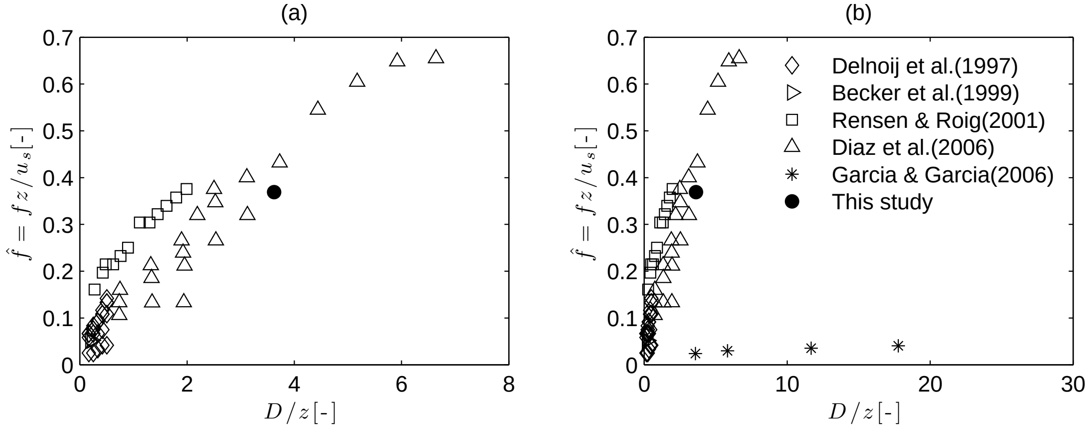

Fig. 5.4. Comparison of non-dimensional peel frequency with previous studies on plume wandering.

the total kinematic buoyancy flux, $B = gQ_b(\rho - \rho_b)/\rho$, bubble slip velocity u_s, and the measurement height z. Then, we obtained the non-dimensional plume oscillation frequency $\hat{f} = fz/u_s$ and the plume parameter $D/z = B/4\pi\alpha^2 z u_s^3$ defined by Bombardelli et al. (2007), where α is the entrainment coefficient (taken as 0.083). As shown in the sub-plot (a), all data are collapsed very well, which means the plume oscillation frequency is independent of the stratification. However, data from García & García (2006) do not collapse with other data due to the fact that the aspect ratio of their tank is much smaller than the other studies, as listed in Table 5.1. It should be noted that the measurement height for Delnoij et al. (1997) is assumed as 25 cm.

Correlations between time-averaged plume peel and trap heights from this study and previous studies are shown in Fig. 5.5. Data points and curves plotted in the figures are non-dimensionalized and plotted as suggested by Socolofsky & Adams (2005). The black square data points and error bars in the figure represent the time-averaged value and standard deviation of the heights from this study. Note that only the first peel (detrainment) event is considered as indicated in Socolofsky & Adams (2005).

Table 5.1. Physical parameters governing bubble plume wandering frequency

References	Aspect ratio (H/W)[a]	$Q_b[10^{-5}\ \mathrm{m}^3/\mathrm{s}]$	u_s [m/s]	z [m]	f [Hz]	D/z [−]
Delnoij et al. (1997)	1.2∼4.06	1∼3	0.3	0.25	0.07∼0.16	0.16∼0.5
Becker et al. (1999)	2.25	1.34	0.3	0.25/0.29	0.059/0.062	0.19∼0.22
Rensen & Roig (2001)	3.1∼4.3	3.06 to 16	0.26	0.465	0.1∼0.2	0.27∼2
Díaz et al. (2006)	9	1.8∼17	0.2	0.363	0.058∼0.33	0.7∼6.67
García & García (2006)	0.49	330∼1600	0.3	3.9	0.0018∼0.0028	3.7∼17.8
this study	1.84	0.1	0.063	0.25	0.1	3.7

---

[a] where H is the tank height and W is tank width.

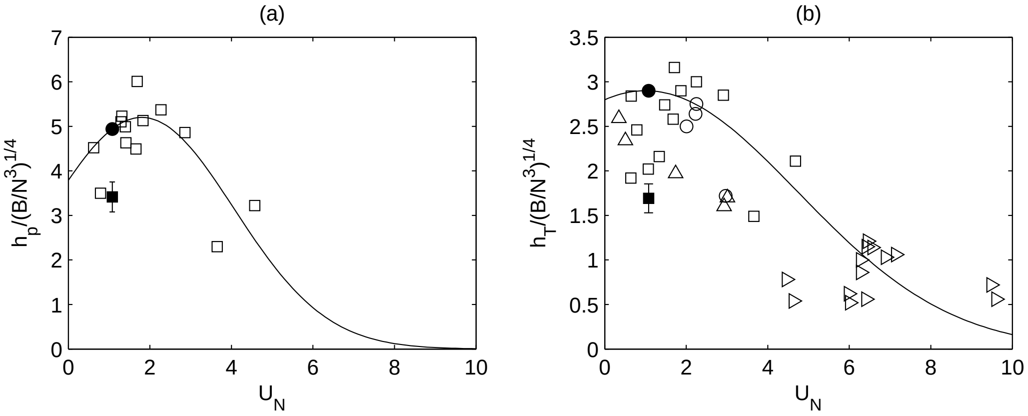

Fig. 5.5. Correlation of plume peel height (a) and plume trap height (b) to U_N. Open circles are data from Asaeda & Imberger (1993), right-pointing triangles are from Lemckert & Imberger (1993), triangles are from Reingold (1994), and open squares are from Socolofsky & Adams (2005). Filled circles are predicted data based on Socolofsky & Adams (2005), and filled squares are measured from this study. Error bars represent the standard deviation of the measured data.

Fig. 5.6 shows the time-averaged PLIF image. It clearly shows the first peel and trap event. The bright area in the plume center represents the bubble core with high number density of bubbles. This bubble core constitutes the inner plume and the less bright area right next to the bubble core is the outer plume of entrained ambient water (McDougall 1978). The outer plume starts to spread out at 63 mm above the diffuser and forms a lateral intrusion from 63 to 163 mm. This lateral intrusion was also measured in the PIV measurements with maximum intrusion velocity of 1 cm/s (Fig. 5.9). Above the intrusion height, the outer plume region becomes narrower until the peel height (upper dotted line), where a second plume starts. This time-averaged PLIF image demonstrates the double-plume model suggested by McDougall (1978) by showing inner plume of bubble core and the outer plume of entrained water.

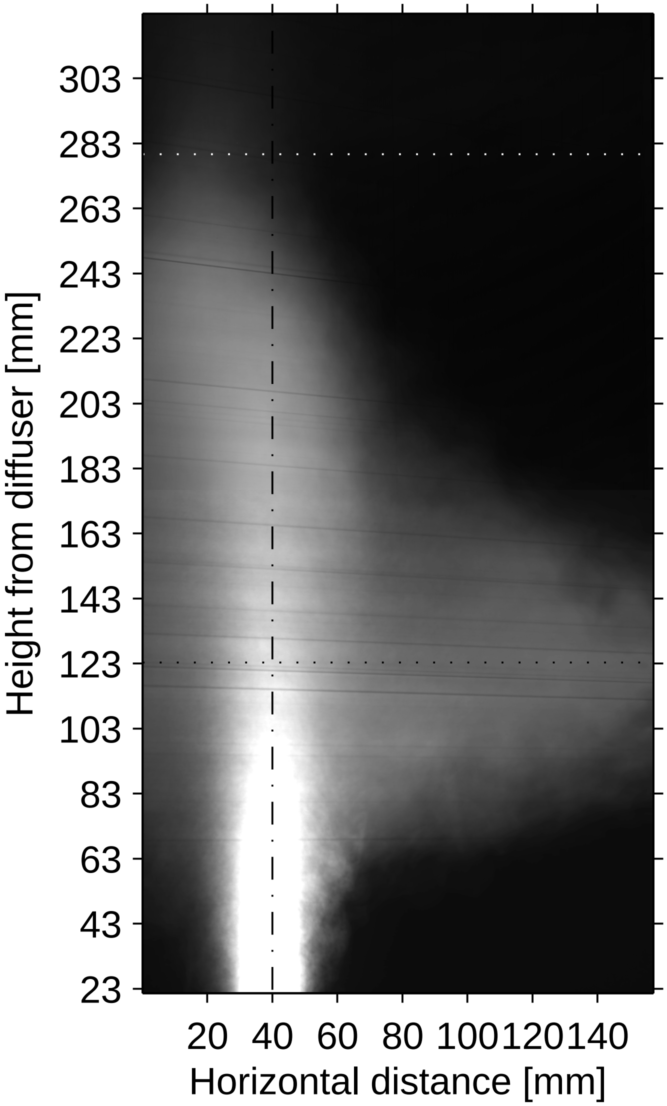

Fig. 5.6. Time-averaged PLIF image. The dashed lines represent the location of plume center, and upper and lower dotted lines represent the peel and trap heights, respectively.

5.4.2 Recommendations for Quantitative PLIF

Quantitative measurements of the concentration field requires precise matching of refractive index of the solution (Daviero et al. 2001). For this purpose, it is necessary to quantify laser intensity variations according to the concentration of the materials (e.g., salt and ethanol for this study) for the refractive index matching. This study also intended to obtain quantitative information on the concentration field of a bubble plume in density-stratified ambient. However, it was found that measurement of both salt and ethanol concentration from the mixture of both solutions is quite difficult with the current experimental setup. Therefore, we here discuss the possibilities to deal with this problem in obtaining quantitative PLIF measurements.

Two-layer fluid density stratification can be one of the possibilities. The lower fluid layer can be a solution of saline water and dye, and the upper layer can be a solution of ethanol. The refractive index of these two different solution can be easily matched using a portable refractometer. In this case, it is possible to predict the ethanol concentration due to its tracking with the dye (Troy & Koseff 2005).

Unlike the above option, linear stratification can be generated using the two-tank method (Daviero et al. 2001). One tank is prepared with solution with salt and water. And, another tank contains the mixture of ethanol, water, and dye for one solution. From careful calibration on the concentration of dye in this solution, the concentration of ethanol in the mixture can be predicted. Thus, it possible to quantify the amount of ethanol in the varying density stratification.

5.4.3 PIV Measurements on a Stratified Bubble Plume

Fig. 5.7 presents instantaneous (sub-plot(a)) and time-averaged (sub-plot (b)) velocity fields of a bubble plume in stratification. In the instantaneous flow field (sub-plot

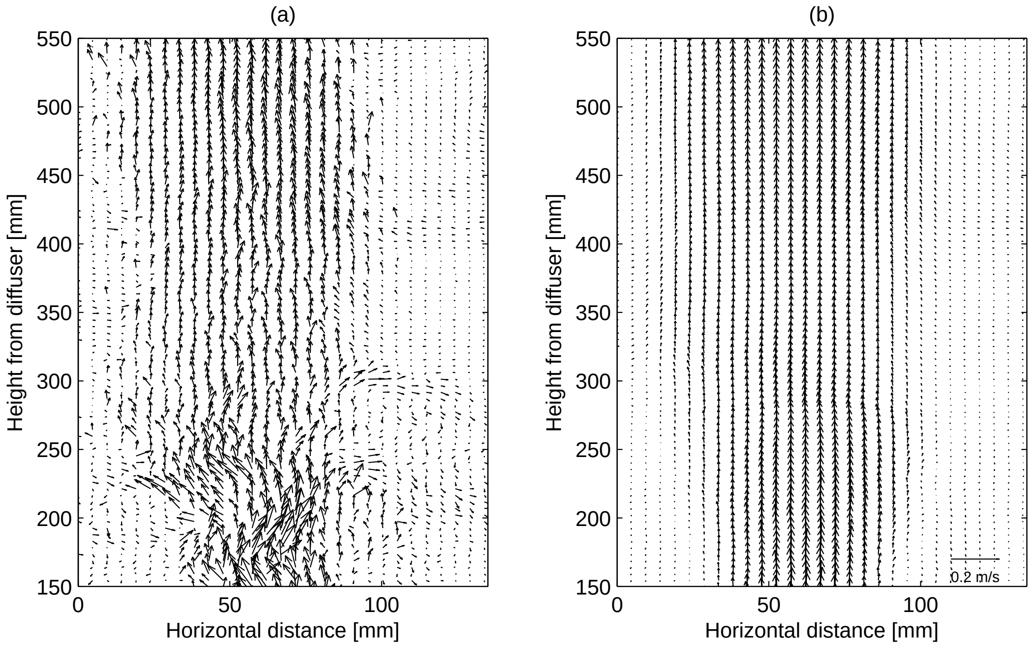

Fig. 5.7. Instantaneous (a) and time-averaged (b) velocity field.

(a)), it can be observed that entrained ambient fluid detrains around 30 cm above the diffuser and intrudes laterally around 20 cm above the diffuser. After the plume detrains entrained fluid, it starts a second plume around 32 cm height, where strong flow into the plume can be observed. Fig. 5.7 (b) shows the time-averaged velocity field of 90 instantaneous velocity maps (22.5 seconds data duration). It can be observed that the strong flow region of the plume center gets narrower from 20 cm to 35 cm, then it gets wider. This can be considered second plume forming after detraining entrained ambient water.

Fig. 5.8 shows contour maps for the horizontal velocity component u (sub-plot (a)) and vertical velocity component v (sub-plot (b)) obtained from the time-averaged velocity field (Fig. 5.7 (b)). The velocity unit in the figure is [m/s]. In the sub-plot (a), positive horizontal velocities are observed at the bottom of the figure. Then, negative velocities, representing flow into the plume, are found at the top of the plot.

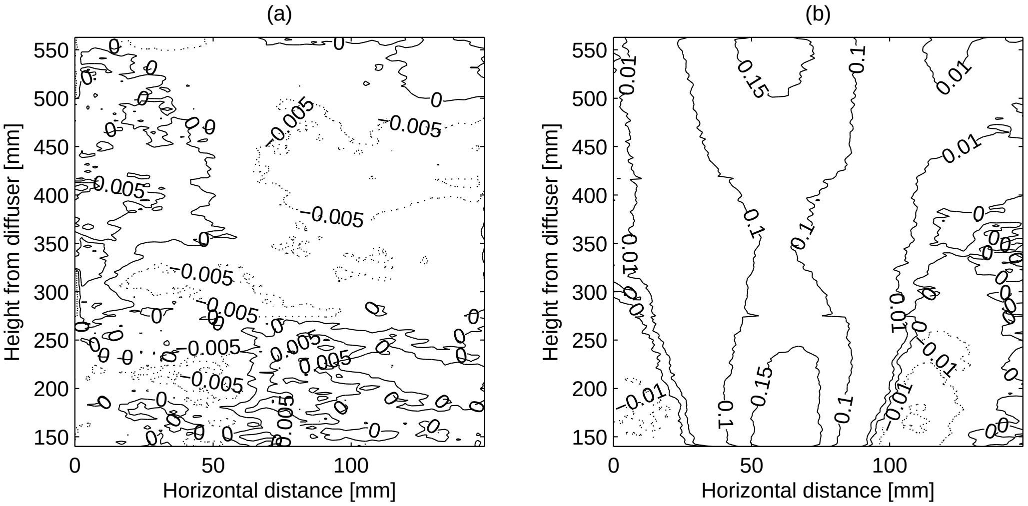

Fig. 5.8. Contour maps for horizontal (a) and vertical (b) velocity components. The negative velocity contour lines are plotted as dotted lines. Note that the velocity unit is [m/s]

In sub-plot (b), strong upward velocity fields are observed along the plume center. Note that we processed bubble velocities together with fluid velocities for this study. It is very interesting to observe that the width of strong upward flow field in the plume center gets narrower and wider around 35 cm above the diffuser. This signifies the generation of second plume after detraining.

Fig. 5.9 shows lateral profiles for horizontal and vertical velocity components at various heights. Columns in sub-plot (a) and (b) represent horizontal and vertical velocity components, respectively. Note that the plume center is located around 6 cm in the horizontal direction. It can be observed that the outward flows from the plume center are found until 18.5 cm at the two bottom plots in column (a). At the same time, there are downward flows outside the plume as shown in the two bottom plots in column (b).

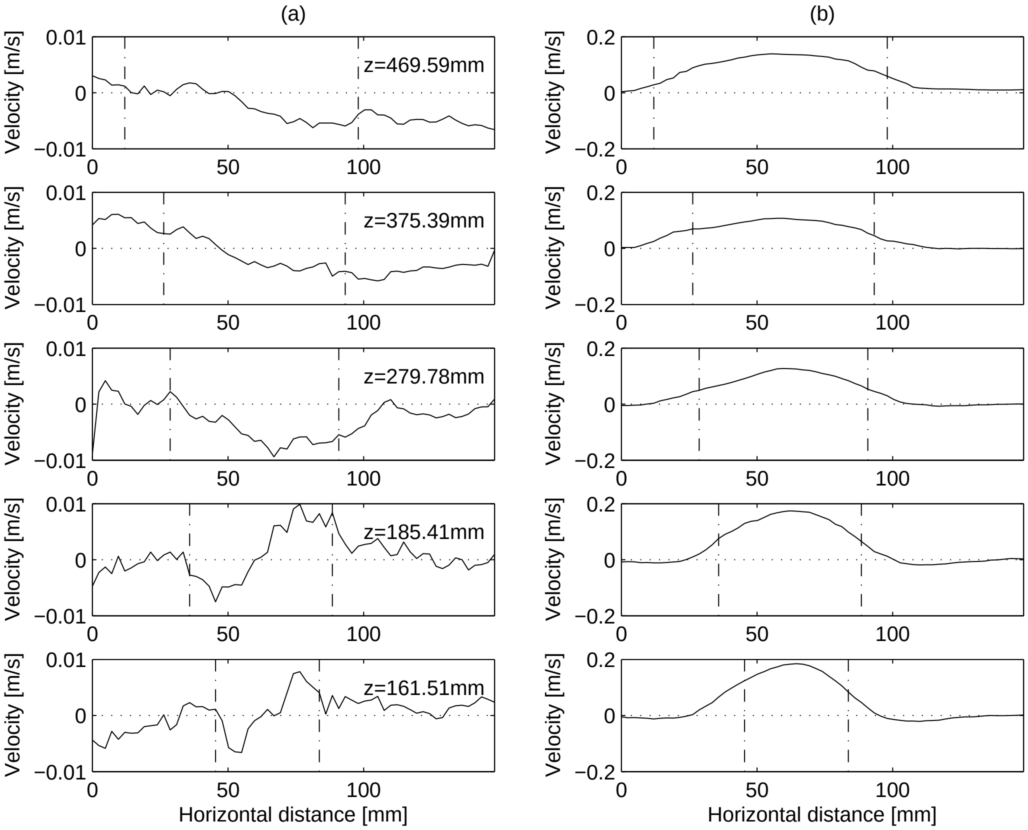

Fig. 5.9. Velocity profiles at various heights. The dashed lines are plume width identified by locating $1/e$ of the maximum velocity.

5.5 Summary

This chapter presents laboratory experiments of a bubble plume in density-stratified ambient conditions using PLIF and PIV measurement techniques.

The entrained ambient fluid are identified by applying a grayscale threshold to PLIF images. From the thresholded image, the peel and trap heights are obtained by finding the maximum height of entrained plume water area and calculating the center of mass at the outside of the plume. Time-series data of peel and trap heights showed that those heights are fluctuating in the early stage and become stabilized. The fluctuation frequencies for both peel and trap heights were identical at around 0.1 Hz. By comparing to previous results in unstratified cases, it was found that the plume fluctuation is closely related to the initial buoyancy flux and bubble slip velocity. The time-averaged peel and trap heights were 25 and 12 cm above the diffuser, respectively.

The velocity field of a stratified bubble plume was measured using the PIV technique. Phase separation for the bubble and liquid phases were not made due to the high bubble concentration inside the bubble column. The measured instantaneous velocity fields captured complex flow properties of entrained water in density-stratified ambient. From the time averaged velocity field, it was observed that the width of the plume gets narrower at the peel height, and later the plume width become wider again where the second plume starts. Lateral intrusion flow with velocity around 1 cm/s was measured around the trap height as well as downward flow.

CHAPTER VI

SUMMARY AND FUTURE RESEARCH

6.1 Summary

This dissertation is focused on the study on the flow and concentration field of a bubble plume using standard measurement techniques in fluid mechanics, such as particle image velocimetry (PIV) and laser-induced fluorescence (LIF). The followings is a summary of the major findings from each section of this dissertation:

- Chapter I: A simple phase separation method using vector post-processing techniques is evaluated to measure velocity fields in a bubble plume. To provide for validation, fluorescent seeding is used, and two sets of synoptic images are obtained: mixed-phase images containing bubbles and fluorescent particles, and fluid-phase images containing only fluorescent particles. A third dataset is derived by applying a digital mask to remove bubbles from the mixed-phase images. All datasets are processed using cross-correlation particle image velocimetry (PIV). The resulting vector maps for the raw, mixed-phase data contain both bubble and continuous-phase velocity vectors. To separate the phases, the vector post-processing algorithm applies a maximum velocity threshold for the continuous phase velocities coupled with the vector median filter to identify remaining bubble velocity vectors and remove them from the mixed-phase velocity field. Because the maximum threshold velocity as well as the two parameters of the vector median filter are unknown, particle tracking velocimetry (PTV) data derived from bubble signatures extracted from the mixed phase images by grayscale thresholding is used for calibration. The optimal post-processing parameters for phase separation are obtained when the best agreement is achieved between the PTV data and the bubble velocity vectors separated from the mixed-phase PIV. To validate the phase separation algorithm, the post-processed fluid-phase vectors are compared to PIV results obtained from both the optically separated and digitally-masked data. The comparison among these methods shows that the post-processed mixed-phase data have small errors in regions near some bubbles, but for dilute environmental flows (area void fraction below 1% and slip velocity approximately equal to the entrained fluid velocity), the algorithm predicts well the instantaneous and time-averaged velocity profiles through the bubble plume and the entrainment properties.

- Chapter II: A direct measurement method for the velocity field in multiphase flows using the particle image velocimetry (PIV) and particle tracking velocimetry (PTV) methods is developed to study the flow characteristics of an unbounded bubble plume in quiescent, unstratified ambient conditions. A single camera is used to obtain images containing both bubbles and fluid tracer particles. Using gray-scale thresholding, phase-separated images of the bubbles are produced, and bubble velocities are obtained from these images using the standard PTV method. Regular PIV is applied to the mixed fluid images, and bubble vectors are removed using a velocity threshold and vector median filter that is calibrated to the PTV result. From the separate velocity fields, the time-averaged flow characteristics of a bubble plume are studied. Gaussian velocity profiles match the entrained fluid velocity, and top-hat velocity profiles match the bubble velocity. Time-averaged values are also presented of velocity, plume width, entrained fluid volume flux, and void fraction as a function of height. From these data, the entrainment coefficient for the entrained ambient fluid is calculated and lies between 0.08 near the plume source and 0.05 in the upper reaches. The results for the entrainment coefficient, together with those from the literature, are correlated to a non-dimensional velocity, given by the ratio of the bubble slip velocity u_s to a characteristic velocity in the plume $(B/z)^{1/3}$, where B is the kinematic buoyancy flux and z is the height above the source.

- Chapter III: The scalar concentration field of a bubble plume is measured using an adaptation of the planar laser-induced fluorescence (PLIF) technique. Due to the light scattering properties of the bubbles, correction of the laser attenuation and diffusion by bubbles is made in the dye concentration calculation by the use of a new attenuation coefficient that depends on the local time-averaged void fraction in the plume. Corrections for laser attenuation by water, dye concentration, and bubbles are made along the laser beam path of a scanning laser light sheet. The bubble signatures and shadows created by bubbles are removed from the raw images using image post-processing. Quantitative evaluation of the dye concentration field is obtained from the corrected image intensity field. The results show similar behavior to single-phase plumes, with greatest concentration fluctuations on the plume centerline. The measured concentration fluctuations are slightly lower on the plume centerline in the bubble plume compared to a single-phase plume due to enhanced turbulent diffusion from the bubble wakes; concentration fluctuations in the plume shear layer and at the edge, both residing outside the bubble column, match those measured in single-phase plumes.

- Chapter IV: The flow properties of a bubble plume in density-stratified conditions are studied using planar laser-induced fluorescence (PLIF) and particle image velocimetry (PIV) techniques. Entrained ambient fluid is identified by applying an intensity threshold to the PLIF images of the passive dye tracer. The peel and trap heights are measured from the thresholded PLIF images. Initial fluctuation of the peel and trap heights are found from the time-series data. Spectral analysis on the time-series of peel and trap height have almost identical peak oscillation frequencies around 0.1 Hz. This plume oscillation frequency is compared with previous studies on plume wandering and shows good agreement based on the non-dimensionalization of frequency ($\hat{f}$) and plume parameter (D). The time-averaged PLIF image shows that the lateral intrusion of the entrained ambient water takes place around 12 cm above the diffuser, while the entrained water detrains around 30 cm above the diffuser. From the PIV measurements, the velocity of plume lateral intrusion was measured as 1 cm/s with downward flow in the outer, detraining fluid of similar velocity.

6.2 Future Research

The following are future research ideas to improve the measurement techniques used and for further understanding of the mixing and flow properties of the multiphase plumes.

- It is necessary to clearly elucidate the limitations of the developed two-phase PIV methods. The proposed vector post-processing method is limited by high void fraction, since the bubble velocity vectors will cover most of the field of view: not many fluid vectors can be found in this case. To deal with this problem, the field of interest needs to be closed up so that the flow situation between bubbles can be captured. The limit of this two-phase PIV can be tested using different source of dispersed phase, such as glass beads, so that the physical properties of dispersed phase (e.g. size and slip velocity) can be easily controlled. Errors in velocity evaluation also can be quantified for velocity gradient between the phases and size difference by generating controlled two-phase flow.

- The state-of-the-art experimental study will provide detailed information and new insight on the flow field around bubble plume. By combining PIV and LIF measurement, temporally evolving velocity and concentration fields in a bubble plume can be measured simultaneously. These data can be used to develop turbulence numerical model for a multiphase flow. The developed numerical model will be very useful to predict flow and concentration field of interest and help assessing biological impact of the contaminant to the surrounding biosphere.
- The developed non-intrusive optical measurement techniques for multiphase plumes enable to capture the small structure of turbulence of a bubble plume in density stratified condition. The measured lab experiment data will provide spatial and temporal turbulent statistics including velocity and concentration field. This information on the small flow structure provides a new insight on entrainment and detrainment process. This also can be incorporated to a numerical model to accurately simulate the entrainment and detrainment process of stratified multiphase plumes.

REFERENCES

Adams, E. E., Caulfield, J. A., Herzog, H. J. & Auerbach, D. I. (1997), 'Impacts of reduced pH from ocean CO_2 disposal: Sensitivity of zooplankton mortality to model parameters', *Waste Management* **17**(5–6), 375–380.

Adrian, R. (1991), 'Particle-imaging techniques for experimental fluid mechanics', *Annu. Rev. Fluid. Mech.* **23**, 261–304.

Adrian, R. J., Christensen, K. T. & Liu, Z.-C. (2000), 'Analysis and interpretation of instantaneous turbulent velocity fields', *Exp. Fluids* **29**, 275–290.

Alendal, G. & Drange, H. (2001), 'Two-phase, near-field modeling of purposefully released CO_2 in the ocean', *J. Geophy. Res.: Oceans* **106**(C1), 1085–1096.

Asaeda, T. & Imberger, J. (1993), 'Structure of bubble plumes in linearly stratified environments', *J. Fluid Mech.* **249**, 35–57.

Baines, W. D. & Leitch, A. M. (1992), 'Destruction of stratification by bubble plumes', *J. Hydr. Engrg.* **118**(4), 559–577.

Bech, K. (2005), 'Dynamic simulation of a 2d bubble column', *Chem. Eng. Sci.* **60**(19), 5294–5304.

Becker, S., Bie, H. D. & Sweeney, J. (1999), 'Dynamic flow behaviour in bubble columns', *Chem. Eng. Sci.* **54**, 4929–4935.

Bombardelli, F. A., Buscaglia, G. C., Rehmann, C. R., Rincón, L. E. & García, M. H. (2007), 'Modeling and scaling of aeration bubble plumes: A two-phase flow analysis', *J. Hydr. Res.* **45**, 617–630.

Bröder, D. & Sommerfeld, M. (2002), 'An advanced LIF-PLV system for analysing the hydrodynamics in a laboratory bubble column at higher void fractions', *Exp. Fluids* **33**, 826–837.

Brücker, C. (2000), *PIV in two-phase flows*, Von Karman Institute for Fluid Dynamics, Chapter Lecture series 2000-01.

Bulson, P. (1967), 'Theory and design of bubble breakwaters', *Dock and Harbour Authority* **42**(560), 47–54.

Cartellier, A. & Achard, J. L. (1991), 'Local phase detection probes in fluid/fluid two-phase flow', *Rev. Sci. Inst.* **62**, 279–303.

Caulfield, J. A. (1996), 'Environmental impacts of carbon dioxide ocean disposal: Plume predictions and time dependent organism experience', MS thesis, Dept. of Civ. Env. Engrg., MIT, Cambridge, MA.

Caulfield, J. A., Adams, E. E., Auerbach, D. I. & Herzog, H. J. (1997), 'Impacts of ocean CO_2 disposal on marine life: II. Probabilistic plume exposure model used with a time-varying dose-response analysis', *Env. Model. and Assess.* **2**(4), 345–353.

Cederwall, K. & Ditmars, J. D. (1970), Analysis of air-bubble plumes, Technical Report KH-R-24, W. M. Keck Laboratory of Hydraulics and Water Resources, Division of Engineering and Applied Science, California Institute of Technology, Pasadena, California.

Chen, D. & Jirka, G. H. (1999), 'LIF study of plane jet bounded in shallow water layer', *J. Hydraul. Eng.* **125**(8), 817–826.

Clift, R., Grace, J. R. & Weber, M. E. (1978), *Bubbles, Drops, and Particles*, Academic Press, New York, NY.

Cowen, E. A., Chang, K.-A. & Liao, Q. (2001), 'A single camera coupled PTV-LIF technique', *Exp. Fluids* **31**, 63–73.

Crimaldi, J. & Koseff, J. (2001), 'High-resolution measurements of the spatial and temporal scalar structure of a turbulent plume', *Exp. Fluids* **31**, 90–102.

Crounse, B. C., Wannamaker, E. J. & Adams, E. E. (2007), 'Integral model of a multiphase plume in quiescent stratification', *J. Hydr. Eng.* **133**(1), 70–76.

Dahm, W. & Dimotakis, P. (1986), 'Measurements of entrainment and mixing in turbulent jets', *AAIA Journal* **25**, 1216–1223.

Daviero, G. J., Roberts, P. J. W. & Maile, K. (2001), 'Refractive index matching in large-scale stratified experiments', *Exp. Fluids* **31**, 119–126.

Deen, N. (2001), 'An experimental and computational study of fluid dynamics in gas-liquid chemical reactors', PhD thesis, Aalborg University, Esbjerg, Denmark.

Deen, N. G., Westerweel, J. & Delnoij, E. (2002*a*), 'Two-phase PIV in bubbly flows: Status and trends', *Chem. Eng. Technol.* **25**(1), 97–101.

Deen, N., Westerweel, J. & Delnoij, E. (2002*b*), 'Two-phase PIV in bubbly flows: Status and trends', *Chem. Eng. Technol.* **25**(1), 97–101.

Delnoij, E., Kuipers, J. A. M. & van Swaai, P. M. (1997), 'Dynamic simulation of gas-liquid two-phase flow: Effect of column aspect ratio on the flow structure', *Chem. Eng. Sci.* **52**, 3759–3772.

Delnoij, E., Kuipers, J. A. M., van Swaaij, P. M. & Westerweel, J. (2000), 'Measurement of gas-liquid two-phase flow in bubble columns using ensemble correlation PIV', *Chem. Eng. Sci.* **55**, 3385–3395.

Delnoij, E., Westerweel, J., Deen, N., Kuipers, J. & van Swaaij, W. (1999), 'Ensemble correlation PIV applied to bubble plumes rising in a bubble column', *Chem. Eng. Sci.* **54**, 5159–5171.

Díaz, M. E., Montes, F. J. & Galán, M. A. (2006), 'Influence of aspect ratio and superficial gas velocity on the evolution of unsteady flow structures and flow transitions in a rectangular two-dimensional bubble column', *Ind. Eng. Chem. Res.* **45**(21), 7301–7312.

Fenneløp, T., Hirschberg, S. & Küffer, J. (1991), 'Surface current and recirculation cells generated by bubble curtains and jets', *J. Fluid. Mech.* **229**, 629–657.

Fenneløp, T. & Sjoen, K. (1980), 'Hydrodynamics of underwater blowouts', *Proc. of AIAA 18th Aerospace Sci. Meeting*, Pasadena, CA.

Ferrier, A., Funk, D. & Roberts, P. (1993), 'Application of optical techniques to the study of plumes in stratified fluids', *Dynam. Atmos. Oceans.* **20**, 155–183.

Fischer, H. B., List, E. G., Koh, R. C. Y., Imberger, J. & Brooks, N. H. (1979), *Mixing in Inland and Coastal Waters*, Academic Press, New York, NY.

García, C. & García, M. (2006), 'Characterization of flow turbulence in large-scale bubble-plume experiments', *Exp. Fluids* **41**, 91–101.

Grota, B. & Strauß, K. (2000), 'DPIV in a particle-laden gas flow - the influence of the particle fluctuation velocities on the accuracy of several cross-correlation-based analysis methods', *EUROMECH 4*, Eindhoven, The Netherlands.

Gui, L., Lindken, R. & Merzkirch, W. (1997), ‘Phase-separated PIV measurements of the flow around systems of bubbles rising in water’, T. Morrow, ed., *ASME-FEDSM97-3103*, ASME fluids engineering division summer meeting, Vancouver, BC, Canada.

Gui, L. & Merzkirch, W. (1996), ‘A method of tracking ensembles of particle images’, *Exp. Fluids* **21**, 465–468.

Hassan, Y., Blanchat, T., Jr, C. S. & Canaan, R. (1992), ‘Simultaneous velocity measurements of both components of a two-phase flow using particle image velocimetry’, *Int. J. Multiphase Flow* **18**, 371–395.

Hilgers, S., Merzkirch, W. & Wagner, T. (1995), ‘PIV measurements in multiphase flow using CCD-and Photo-camera’, *ASME-FED* **209**, 151–154.

Hu, H., Saga, T., Kobayashi, T., Okamoto, K. & Taniguchi, N. (1998), ‘Evaluation of the cross correlation method by using PIV standard images’, *J. Visualization* **1**, 87–94.

Hugi, C. (1993), ‘Modelluntersuchungen von Blasenstrahlen für die Seebelüftung’, Ph.D. Thesis, Inst. f. Hydromechanik u. Wasserwirtschaft, ETH, Zürich.

Jakobsen, M., Easson, W., Greated, C., & Glass, D. (1996), ‘Particle image velocimetry: Simultaneous two-phase flow measurements’, *Meas. Sci. Technol.* **7**, 1270–1280.

Johansen, Ø. (2000), ‘DeepBlow – a Lagrangian plume model for deep water blowouts’, *Spill Science & Technology Bulletin* **6**(2), 103–111.

Keane, R. & Adrian, R. (1992), ‘Theory of cross-correlation analysis of PIV images’, *App. Sci. Res.* **49**, 191–215.

Khalitov, D. & Longmire, E. (2002), ‘Simultaneous two-phase PIV by two-parameter phase discrimination’, *Exp. Fluids* **32**, 252–268.

Kiger, K. & Pan, C. (2000), ‘PIV technique for the simultaneous measurement of dilute two-phase flows’, *J. Fluids. Engrg.* **122**, 811–818.

Kobus, H. E. (1968), ‘Analysis of the flow induced by air-bubble systems’, *Proc. 11th Int. Conf. Coastal Engrg., London*, ASCE, Reston, VA, pp. 1016–1031.

Koochesfahani, M. & Dimotakis, P. (1985), ‘Laser-induced fluorescence measurements of mixed fluid concentration in a liquid plane shear layer’, *AAIA Journal* **23**, 1700–1707.

Koynov, A., Tryggvason, G., Schluter, M. & Khinast, J. G. (2006), ‘Mass transfer and chemical reactions in reactive deformable bubble swarms’, *Applied Physics Letters* **88**(13). 134102.

LaVision GmbH (2002), *DaVis FlowMaster Software Mannual for DaVis 6.2*, LaVision GmbH.

Lee, J. H. W. & Chu, V. H. (2003), *Turbulent Jets and Plumes : A Lagrangian Approach*, Kluwer Academic Publishers, Boston.

Leitch, A. M. & Baines, W. D. (1989), ‘Liquid volume flux in a weak bubble plume’, *J. Fluid Mech.* **205**, 77–98.

Lemckert, C. J. & Imberger, J. (1993), ‘Energetic bubble plumes in arbitrary stratification’, *J. Hydr. Engrg.* **119**(6), 680–703.

Lindken, R., Gui, L. & Merzkirch, W. (1999), ‘Velocity measurements in multiphase flow by means of particle image velocimetry’, *Chem. Eng. Technol.* **22**(3), 202–206.

Lindken, R. & Merzkirch, W. (1999), 'Velocity measurements of liquid and gaseous phase for a system of bubbles rising in water', R. Adrian, ed., *Proc. of the third international workshop on PIV*, Santa Barbara, California, pp. 113–118.

Lindken, R. & Merzkirch, W. (2002), 'A novel PIV technique for measurements in multiphase flows and its application to two-phase bubbly flows', *Exp. Fluids* **33**, 814–825.

Liro, C. R., Adams, E. E. & Herzog, H. J. (1992), 'Modeling the release of CO_2 in the deep ocean', *Energy Conserv. Mgmt.* **33**(5–8), 667–674.

Liu, Z. & Adrain, R. (1992), *Simultaneous Imaging of the Velocity Fields of Two Phases*, New York: Butterworth, pp. 35–58.

McDougall, T. J. (1978), 'Bubble plumes in stratified environments', *J. Fluid Mech.* **85**(4), 655–672.

McGinnis, D., Lorke, A., Wüest, A., Stöckli, A. & Little, J. (2004), 'Interaction between a bubble plume and the near field in a stratified lake', *Water Resour. Res.* **40**, W10206.

Milgram, J. H. (1983), 'Mean flow in round bubble plumes', *J. Fluid Mech.* **133**, 345–376.

Monkewitz, P. (1988), 'The absolute and convetive nature of ibstability in two-dimensional wakes at low reynolds numbers', *Phys. Fluids* **31**(5), 999–1006.

Motarjemi, M. & Jameson, G. (1978), 'Mass transfer from very small bubbles - the optimum bubble size for aeration', *Chem. Eng. Sci.* **33**, 1415–1423.

Oakley, T., Loth, E. & Adrain, R. (1997), 'A two-phase cinematic PIV method for bubbly flows', *J. Fluids. Engrg.* **119**, 707–712.

Papanicolaou, P. N. & List, E. J. (1988), 'Investigations of round turbulent buoyant jets', *J. Fluid Mech.* **195**, 341–391.

Papanicolaou, P. N. & List, E. J. (1989), 'Large-scale structure in the far field of buoyant jets', *J. Fluid Mech.* **209**, 151–190.

Raffael, M., Willert, C. & Kompenhan, J. (1998), *Particle Image Velocimetry: A Practical Guide*, Springer-Verlag, Germany.

Rensena, J. & Roig, V. (2001), 'Experimental study of the unsteady structure of a confined bubble plume', *Int. J. Multiphase Flow* **27**, 1431–1449.

Riebesell, U. I., Rost, B., Tortell, P. D., Zeebe, R. E. & Morel, F. M. (2000), 'Reduced calcification of marine Plankton in response to increased atmospheric CO_2', *Nature* **407**, 364–367.

Rottenkolber, G., Gindele, J., Raposo, J., Dullenkopf, K., Hentschel, W., Witting, S., Spicher, U. & Merzkirch, W. (1999), 'Spray analysis of a gasoline direct injector by means of simultaneous two-phase PIV', R. Adrian, ed., *Proc. of the third international workshop on PIV*, Santa Barbara, California, pp. 209–216.

Roy, S. & Duke, S. (2004), 'Visualization of oxygen concentration fields and measurement of concentration gradients at bubble surfaces in surfactant-contaminated water', *Exp. Fluids* **36**, 654–662.

Ryu, Y., Chang, K.-A. & Lim, H.-J. (2005), 'Use of bubble image velocimetry for measurement of plunging wave impinging on structure and associated greenwater', *Meas. Sci. Tech.* **16**, 1945–1953.

Sakakibara, J., Wicker, R. & Eaton, J. (1996), 'Measurements of particle-fluid velocity correlation and the extra dissipation in a round jet', *J. Multiphase Flow*

22(5), 863–881.

Schladow, S. G. (1993), ‘Lake destratification by bubble-plume systems: Design methodology’, *J. Hydr. Engrg.* **119**(3), 350–368.

Schlüter, M. & Räbiger, N. (1998), ‘Bubble swarm velocity in two phase flows’, *Proceedings of the ASME Heat Transfer Division*, Vol. 5, ASME, pp. 275–280.

Seol, D.-G., Bhaumik, T., Bergmann, C. & Socolofsky, S. (2007), ‘Particle image velocimetry measurements of the mean flow characteristics in a bubble plume’, *J. Eng. Mech.* **133**(6), 665–676.

Seol, D.-G., Bryant, D. B. & Socolofsky, S. (2008), ‘Accounting for bubble effects on concentration field measurements in a bubble plume using planar laser-induced fluorescence (PLIF)’, *Exp. Fluids* (submitted).

Seol, D.-G. & Socolofsky, S. (2008), ‘Vector post-processing algorithm for phase discrimination of two-phase PIV’, *Exp. Fluids* (DOI 10.1007/s00348-008-0473-9).

Simiano, M., Zboray, R., de Cachard, F., Lakehal, D. & Yadigaroglu, G. (2006), ‘Comprehensive experimental investigation of the hydrodynamics of large-scale, 3d, oscillating bubble plumes’, *Int. J. Multiphase Flow* **32**, 1160–1181.

Socolofsky, S. A. (2001), ‘Laboratory Experiments of Multi-phase Plumes in Stratification and Crossflow’, Ph.D. Thesis, Dept. of Civ. Env. Engrg., MIT, Cambridge, MA.

Socolofsky, S. A. & Adams, E. E. (2002), ‘Multi-phase plumes in uniform and stratified crossflow’, *J. Hydr. Res.* **40**(6), 661–672.

Socolofsky, S. A. & Adams, E. E. (2003), ‘Liquid volume fluxes in stratified multiphase plumes’, *J. Hydr. Engrg.* **129**(11), 905–914.

Socolofsky, S. A. & Adams, E. E. (2005), ‘Role of slip velocity in the behavior of stratified multiphase plumes’, *J. Hydr. Engrg.* **131**(4), 273–282.

Socolofsky, S. A., Crounse, B. C. & Adams, E. E. (2002), ‘Multi-phase plumes in uniform, stratified and flowing environments’, H. Shen, A. Cheng, K.-H. Wang, M. H. Teng & C. Liu, eds, *Environmental Fluid Mechanics–Theories and Applications*, ASCE/Fluids Committee, Chapter 4, pp. 84–125.

Soga, C. & Rehmann, C. (2004), ‘Dissipation of turbulent kinetic energy near a bubble plume’, *J. Hydr. Engrg.* **130**, 441–449.

Song, X., Shen, L., Murai, Y. & Yamamoto, F. (1999), ‘Separation of particle-bubble images in multiphase flow’, R. Adrian, ed., *Proc. of the third international workshop on PIV*, Santa Barbara, California, pp. 15–18.

Sridhar, G. & Katz, J. (1995), ‘Drag and lift forces on microscopic bubbles entrained by a vortex’, *Phys. Fluids* **7**(2), 389–399.

Sridhar, G., Ran, B. & Katz, J. (1991), ‘Implementation of particle image velocimetry to multi-phase flow’, H. Kato & O. Furuya, eds, *Cavitation Multiphase Flow Forum*, ASME, New York, pp. 205–210.

Tian, X. & Roberts, P. (2003), ‘A 3D LIF system for turbulent buoyant jet flows’, *Exp. Fluids* **35**, 636–647.

Tokuhiro, A., Maekawa, M., Iizuka, K., Hishida, K. & Maeda, M. (1998), ‘Turbulent flow past a bubble and an ellipsoid using shadow-image and PIV techniques’, *Int. J. Multiphase Flow* **24**, 1383–1406.

Topham, D. R. (1975), Hydrodynamics of an oilwell blowout, Technical Report 33, Beaufort Sea, Institute of Ocean Sciences, Sidney, B.C., Canada.

Troy, C. D. & Koseff, J. R. (2005), 'The generation and quantitative visualization of breaking internal waves', *Exp. Fluids* **38**, 549–562.

Wain, D. & Rehmann, C. (2005), 'Eddy diffusivity near bubble plumes', *Water Resour. Res.* **41**, W09409.

Webster, D., Rahman, S. & Dasi, L. (2003), 'Laser-induced fluorescence measurements of a turbulent plume', *J. Eng. Mech.* **129**(10), 1130–1137.

Webster, D., Roberts, P. & Ra'ad, L. (2001), 'Simultaneous DPIV/PLIF measurements of a turbulent jet', *Exp. Fluids* **30**, 65–72.

Westerweel, J. (1994), 'Efficient detection of supurious vectors in particle image velocimetry data', *Exp. Fluids* **16**, 236–247.

Wilkinson, D. L. (1979), 'Two-dimensional bubble plumes', *J. Hydr. Div.* **105**(HY2), 139–154.

Willert, C. (1997), 'Stereoscopic digital particle image velocimetry for application in wind tunnel flows', *Meas. Sci. Tech.* **8**(12), 1465–1479.

Wüest, A., Brooks, N. H. & Imboden, D. M. (1992), 'Bubble plume modeling for lake restoration', *Water Resour. Res.* **28**(12), 3235–3250.

Yapa, P. D. & Zheng, L. (1997), 'Simulation of oil spills from underwater accidents I: Model development', *J. Hydr. Res.* **35**(5), 673–687.

Yapa, P. D., Zheng, L. & Nakata, K. (1999), 'Modeling underwater oil/gas jets and plumes', *J. Hydr. Engrg.* **125**(5), 481–491.

Zheng, L. & Yapa, P. D. (1998), 'Simulation of oil spills from underwater accidents II: Model verification', *J. Hydr. Res.* **36**(1), 117–134.

Zhou, L. X., Li, R. X. & Du, R. X. (2006), 'Numerical simulation of the effect of void fraction and inlet velocity on two-phase turbulence in bubble-liquid flows', *Acta Mechanica Sinica* **22**(5), 425–432.

Zic, K., Stefan, H. G. & Ellis, C. (1992), 'Laboratory study of water destratification by a bubble plume', *J. Hydr. Res.* **30**(1), 7–27.

APPENDIX A

IMAGE CORRECTION PROCEDURES

1. **Correction for CCD background noise, vignette.** Corrected image is given by

   $$I_{c1}(i,j) = K\frac{I_{raw}(i,j) - I_b(i,j)}{I_s(i,j) - I_b(i,j} \tag{A.1}$$

   where $I_{c1}(i,j)$ is corrected image for background noise and lens vignette, K is average pixel value in the standard image, $I_{raw}(i,j)$ is raw image $I_b(i,j)$ is black level image (image with camera cap on), and $I_s(i,j)$: standard image (image with uniform background).

2. **Correction for vertical non-uniformity.** Correction base image for each column i is given by

   $$I_{base}(i,j) = \frac{I_{c=30\mu g/l}(i,:)}{\bar{I}_s(i,:)} \tag{A.2}$$

   Then, the corrected image is given by

   $$I_{c2}(i,j) = \frac{I_{c1}(i,j)}{I_{base}(i,j)} \tag{A.3}$$

3. **Bubble removing.** Bubbles are removed using bubble templates as shown in Figure A.1.

4. **Image transform from pixel coordinate system ($I_{c2}(i,j)$) to radial coordinate system ($I_{c2}(r,\theta)$).** The conversion to radial coordinate system can be done by

   $$r = \sqrt{(x_0 + i)^2 + (j - y_0)^2} \tag{A.4}$$

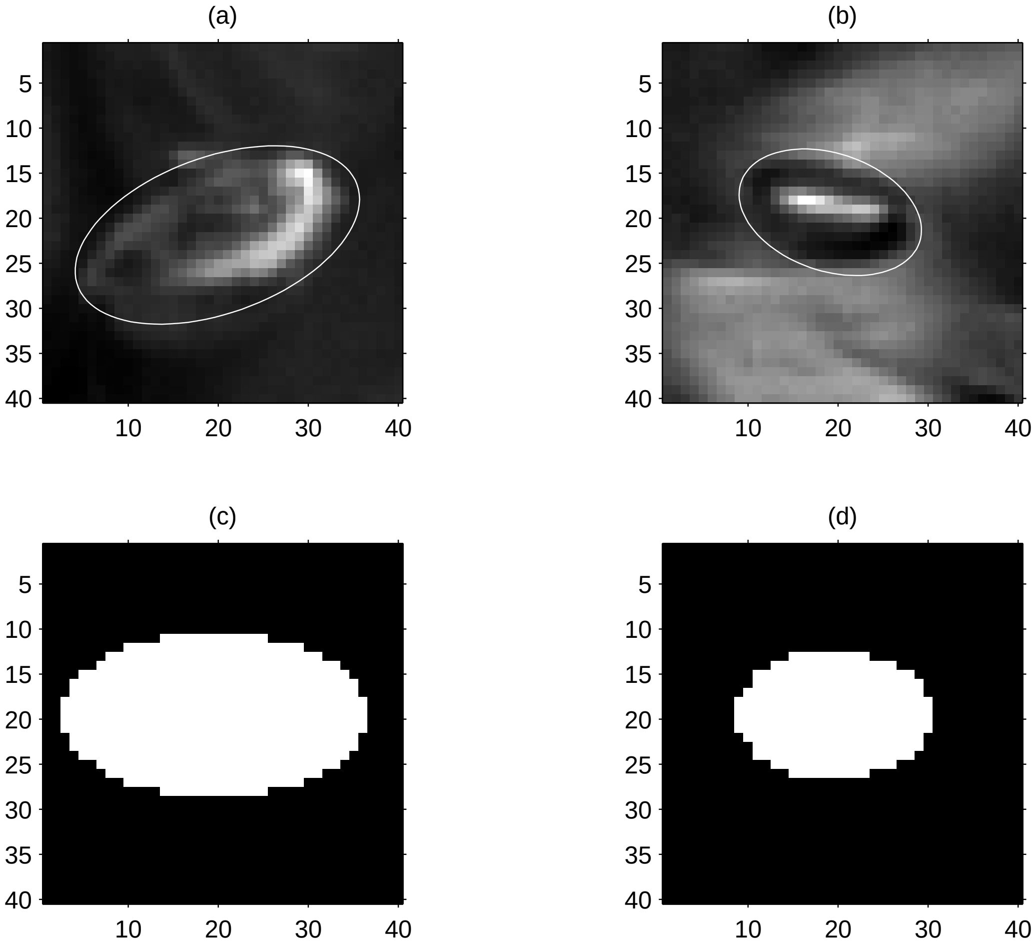

Fig. A.1. Bubble mask template. (a) Sampled large bubble image, (b) sampled small bubble image from an instantaneous image, (c) large bubble mask generated from (a), and (d) small bubble mask generated from (b).

$$\theta = \tan^{-1}\left(\frac{j - y_0}{x_0 + i}\right) \tag{A.5}$$

where x_0 and y_0 are the location of the scanning mirror in pixel.

5. **Laser attenuation: water, dye, & bubbles.**

   $$I_{c3}(r,\theta) = \frac{I_{c2}(r,\theta)}{\exp\left(-\sum_r a\Delta r\right)} \tag{A.6}$$

   where, $a = a_w + ca_d + \alpha a_v$: laser attenuation coefficient by water($a_w = 1.1859 \times 10^{-4}$[pixel^{-1}]) , dye ($a_d = 2.6314 \times 10^{-6}$[$\mu$g/l^{-1}pixel^{-1}]), and bubble void fraction ($a_v = 2.5 \times 10^{-5}$[%$^{-1}$pixel^{-1}]). c is local dye concentration, and α is local void fraction.

   Local dye concentration is obtained by

   $$c(r,\theta) = \frac{I_{c2}(r,\theta) - B(r,\theta)}{A(r,\theta)} \tag{A.7}$$

   where $A(r,\theta)$ and $B(r,\theta)$ are slope and intercept obtained from uniform dye calibration image before laser attenuation correction

6. **Inverse transform of image from radial coordinate system ($I_{c3}(r,\theta)$) to pixel coordinate system ($I_{cc}(i,j)$).**

7. **Convert image intensity to concentration.**

   $$C(i,j) = \frac{I_{cc}(i,j) - B^{'}(i,j)}{A^{'}(i,j)} \tag{A.8}$$

   where $A^{'}(i,j)$ and $B^{'}(i,j)$ are slope and intercept obtained from uniform dye calibration image after laser attenuation correction.

APPENDIX B

SLIP VELOCITY OF BUBBLES IN WATER

1. **Bubbles in pure water** For bubbles with equivelent bubble diameter $d_e > 1.3mm$ in pure water,

   $$U_s = [(2.14\sigma/\rho d_e) + 0.505 g d_e]^{1/2} \tag{B.1}$$

   where U_s is the bubble slip velocity, σ is the surface tension of water ($= 0.0736 kg/s^2$), d_e is the equivelent bubble diameter, and g is the gravity acceleration.

2. **Bubbles in contaminated water** For bubbles in contaminated water,

   $$U_s = \frac{\mu}{\rho \cdot d_e} M^{-0.149} (J - 0.857) \tag{B.2}$$

   where μ is the viscosity of water ($= 1.005 \times 10^{-3} kg/m{\cdot}s$) and ρ is the water density ($= 998.2 kg/m^3$). M is the Morton number, which is defined by

   $$M = g\mu^4 \Delta\rho/\rho^2\sigma^3 \tag{B.3}$$

   where $\Delta\rho$ is the density difference between water and air ($= 1.4 kg/m^3$). And, J is defined by the H as follows:

   $$J = 0.94 H^{0.757} \qquad (2 < H \leq 59.3) \tag{B.4}$$

   and

   $$J = 3.424 H^{0.441} \qquad (H > 59.3) \tag{B.5}$$

where

$$H = \frac{4}{3} E_o M^{-0.149} (\mu/\mu_w)^{-0.14} \tag{B.6}$$

where μ_w is the viscosity of water in Braida's experiments, which can be taken as $0.0009 kg/m{\cdot}s$, and E_o is the Eötvös number as defined by

$$E_o = g \Delta\rho {d_e}^2 / \sigma \tag{B.7}$$

APPENDIX C

VOID FRACTION IN A BUBBLE PLUME

1. **Local void fraction.** Void fraction at a point or a very small volume when measured experimentally. $\alpha_{local} = 0$ when liquid phase is present and $\alpha_{local} = 1$ when gas phase is present. Typically, this void ratio is measured using optic probe for a certain amount of time, T. When $P(r, t)$ represents the local instantaneous presence of gas phase at location, r, the local time-averaged void fraction can be given by

$$\alpha_{local}(r,t) = \frac{\int_T P(r,t)\,dt}{T} \tag{C.1}$$

This can be incorpolated to the image recording of a bubble plume by calculating local void fraction at each pixel. A bubble is assumed to stay at a local point for camera exposure time (10 ms). When a bubble is present at a local pixel point, it is counted as n. If T is the total measurement time, the local void fraction is defined by

$$\alpha_{local}(x_i) = \frac{n{\cdot}\Delta t}{T} \tag{C.2}$$

where x_i is a local pixel point and Δt is the camera exposure time.

2. **Cross-sectional void fraction.** Ratio of the area of the cross-section of the channel occupied by the gas phase to the total area of the cross-section of the channel. The cross-sectional void fraction can be determined by

$$\alpha_{cross-section} = \frac{A_G}{A_G + A_L} \tag{C.3}$$

where A_G is the area of the cross-section of the channel occupied by the gas phase and A_L is that of the liquid phase.

3. **Volumetric void fraction.** Ratio of the volume of the channel occupied by the gas phase to the total volume of the cross-section of the channel. The cross-sectional void fraction can be determined by

$$\alpha_{volumetric} = \frac{V_G}{V_G + V_L} \tag{C.4}$$

where V_G is the volume of the cross-section of the channel occupied by the gas phase and V_L is that of the liquid phase. This can be inditectly calculated from the ideal gas law under the assumption of isothermal expansion of a bubble as:

$$Q_b(z) = \frac{Q_0 H_A}{(H_T - z)} = \int_0^\infty 2\pi r C(z,r)(u(z,r) + u_s)dr = \pi b^2 C_m(z)\left[U_m(z) + u_s\right] \tag{C.5}$$

VITA

Dong-Guan Seol was born in 1974 in Ulsan, South Korea. He entered the Department of Ocean Engineering at Pukyong National University, Pusan, Korea in 1992. After finishing his bachelor and master degree in the same university, he joined the Korean Navy as a naval officer in 1998. After serving in the navy for three years, he started his professional career as a researcher at GeoSystem Research Corporation from in 2002. He came to Texas A&M University in the Fall of 2003 to pursue his doctoral degree in Ocean Engineering. His research interests include environmental fluid mechanics, experimental and numerical study of multiphase flows, and coastal engineering.

Permanent address: 144 Mangyang-ri Onyang-eup Ulju
Ulsan 689-901, South Korea
Email address: seoldg@yahoo.co.kr

This document was typeset in LaTeX by Dong-Guan Seol.